



저작자표시-비영리-동일조건변경허락 2.0 대한민국

이용자는 아래의 조건을 따르는 경우에 한하여 자유롭게

- 이 저작물을 복제, 배포, 전송, 전시, 공연 및 방송할 수 있습니다.
- 이차적 저작물을 작성할 수 있습니다.

다음과 같은 조건을 따라야 합니다:



저작자표시. 귀하는 원저작자를 표시하여야 합니다.



비영리. 귀하는 이 저작물을 영리 목적으로 이용할 수 없습니다.



동일조건변경허락. 귀하가 이 저작물을 개작, 변형 또는 가공했을 경우에는, 이 저작물과 동일한 이용허락조건하에서만 배포할 수 있습니다.

- 귀하는, 이 저작물의 재이용이나 배포의 경우, 이 저작물에 적용된 이용허락조건을 명확하게 나타내어야 합니다.
- 저작권자로부터 별도의 허가를 받으면 이러한 조건들은 적용되지 않습니다.

저작권법에 따른 이용자의 권리는 위의 내용에 의하여 영향을 받지 않습니다.

이것은 [이용허락규약\(Legal Code\)](#)을 이해하기 쉽게 요약한 것입니다.

[Disclaimer](#)

공학박사학위논문

Frequency-domain seismic waveform inversion  
based on the Lippmann-Schwinger equation

리프먼-슈윙거 방정식에 기초한  
주파수영역 탄성파 파형역산

2014 년 8 월

서울대학교 대학원  
에너지시스템공학부  
곽 상 민







# Abstract

## Frequency-domain seismic waveform inversion based on the Lippmann-Schwinger equation

Sangmin Kwak

Department of Energy Systems Engineering

The Graduate School

Seoul National University

Waveform inversion, a seismic data processing technique, is a tomographic method to estimate the physical properties of subsurface media from seismic data. Full-waveform inversion (FWI) solves the inverse problem as an iterative data-fitting procedure, which takes advantage of the forward modeling of wave propagation and the local optimization. The solutions of the inverse problem have the potential to converge to local minima due to the nonlinear aspects and the local optimization approach, which complicates frequency-domain FWI methods.

In this study, I propose a seismic waveform inversion method based on the Lippmann-Schwinger equation; the method is called Lippmann-Schwinger waveform inversion (LSWI). Waveform inversion is a type of inverse scattering problem that inputs the reference model, reference wavefield and seismic data measured at receivers and outputs the medium perturbation as the difference of the reference model and actual medium. LSWI directly solves the inverse scattering problem based on the Lippmann-Schwinger equation, which is a fundamental equation in scattering theory. The medium perturbation is computed as the perturbation

operator from the definition of the virtual scattering source and is used to update the reference velocity models. Sloth (i.e., square of slowness) is included in the perturbation operator and has a linear relationship with the pressure wavefield in the acoustic wave equation. LSWI avoids the local minima convergence problem through the linear relationship of sloth and the direct inverse approach. The sequential frequency strategy is selected because the inverted model depends on the initial model due to the single scattering assumption. I used numerical examples to demonstrate that LSWI can estimate the subsurface velocity model from surface seismic data containing low-frequency components if the inversion starts from an initial velocity model not too far from the medium of interest.

Real data applications of LSWI require pre-processing of the given data set to remove noise. The selection of an initial velocity model and the employment of low frequency components are also important to achieve a more exact solution for waveform inversion. Most of the problems associated with the real data applications of LSWI are analogous to those of FWI. In the case of the marine streamer data set, a problem with insufficient data due to the limited offsets prevents the estimation of medium perturbations from the data residual. A divide-and-conquer approach can be considered as a solution for this problem.

**Keywords:** seismic tomography, waveform inversion, scattering theory, frequency domain, Lippmann-Schwinger equation

**Student Number:** 2010-21022

# Contents

<b>Abstract</b>	<b>i</b>
<b>List of Figures</b>	<b>v</b>
<b>1. Introduction</b>	<b>1</b>
1.1 Full-waveform inversion . . . . .	2
1.2 Scattering theory and inverse scattering problem . . . . .	5
1.3 The Lippmann-Schwinger equation . . . . .	7
1.4 Outline . . . . .	9
<b>2. Theory</b>	<b>11</b>
2.1 Lippmann-Schwinger equation of seismic scattering . . . . .	12
2.2 Waveform inversion based on the Lippmann-Schwinger equation	16
2.3 Waveform inversion procedure . . . . .	20
2.3.1 Forward modeling of the acoustic wave equation . . . . .	21
2.3.2 The virtual scattering source . . . . .	28

2.3.3	The scattered wavefield and total wavefield . . . . .	32
2.3.4	The sloth perturbation . . . . .	33
2.3.5	Updating of the velocity model . . . . .	36
<b>3.</b>	<b>Numerical examples</b>	<b>39</b>
3.1	Synthetic data example for the Marmousi model . . . . .	40
3.1.1	Sensitivity to the presence of noise in data . . . . .	61
3.1.2	Sensitivity to the lack of low frequencies in data . . . . .	69
3.1.3	Sensitivity to the accuracy of the initial models . . . . .	72
3.2	Field data example with the Gulf of Mexico data set . . . . .	82
3.3	Field data example with the TOTAL data set . . . . .	96
<b>4.</b>	<b>Discussion</b>	<b>103</b>
4.1	The presence of noise in data . . . . .	105
4.2	The lack of low frequencies in data . . . . .	107
4.3	The accuracy of the initial models . . . . .	109
4.4	Green's function and the assumption of acoustic media . . . . .	112
<b>5.</b>	<b>Conclusions</b>	<b>113</b>
	<b>References</b>	<b>117</b>
	<b>초 록</b>	<b>125</b>

# List of Figures

Figure 2.1	A diagram of the data residual, virtual scattering source and scattered wavefield. The inverted triangles and stars denote receivers and sources, respectively. The virtual scattering source is formulated to reconstruct the scattered wavefield from the data residual. . . . .	19
Figure 2.2	The workflow of Lippmann-Schwinger waveform inversion (LSWI). . . . .	37
Figure 3.1	The Marmousi P-wave velocity model. . . . .	42
Figure 3.2	(a) A common-shot gather seismogram and (b) a frequency spectrum of the synthetic seismic data for the Marmousi model. . . . .	43
Figure 3.3	The initial velocity model for the waveform inversion of the synthetic Marmousi data set. . . . .	44

Figure 3.4	The frequency-domain reference wavefields propagated in the reference velocity model for the 100th shot (located at a distance of 4.8 km) with respect to a frequency of (a) 5 Hz, (b) 10 Hz and (c) 15 Hz. . . . .	45
Figure 3.5	The frequency-domain data residuals for the 100th shot (located at a distance of 4.8 km) with respect to a frequency of (a) 5 Hz, (b) 10 Hz and (c) 15 Hz before performing the waveform inversion. . . . .	46
Figure 3.6	The frequency-domain virtual scattering sources for the 100th shot (located at a distance of 4.8 km) with respect to a frequency of (a) 5 Hz, (b) 10 Hz and (c) 15 Hz. . . . .	49
Figure 3.7	The frequency-domain scattered wavefields reconstructed for the 100th shot (located at a distance of 4.8 km) with respect to a frequency of (a) 5 Hz, (b) 10 Hz and (c) 15 Hz. . . . .	50
Figure 3.8	The frequency-domain total wavefields reconstructed for the 100th shot (located at a distance of 4.8 km) with respect to a frequency of (a) 5 Hz, (b) 10 Hz and (c) 15 Hz. . . . .	51
Figure 3.9	The frequency-domain actual wavefields propagated in the true Marmousi velocity model for the 100th shot (located at a distance of 4.8 km) with respect to a frequency of (a) 5 Hz, (b) 10 Hz and (c) 15 Hz. . . . .	52
Figure 3.10	The sloth perturbations computed with respect to a frequency of (a) 5 Hz, (b) 10 Hz and (c) 15 Hz. . . . .	53

Figure 3.11	The velocity model updated by the waveform inversion of the synthetic Marmousi data set. . . . .	54
Figure 3.12	The frequency-domain data residuals for the 100th shot (located at a distance of 4.8 km) with respect to the frequency of (a) 5 Hz, (b) 10 Hz and (c) 15 Hz. The data residual computed with forward-modeled data for the initial velocity model (dashed line) and the total wavefield (solid line) after performing the waveform inversion. . . . .	56
Figure 3.13	The common-shot gather seismograms for the 50th shot (located at a distance of 2.4 km): seismograms synthesized for the (a) initial, (b) inverted and (c) true velocity models. . . . .	57
Figure 3.14	The common-shot gather seismograms for the 100th shot (located at a distance of 4.8 km): seismograms synthesized for the (a) initial, (b) inverted and (c) true velocity models. . . . .	58
Figure 3.15	The common-shot gather seismograms for the 150th shot (located at a distance of 7.2 km): seismograms synthesized for the (a) initial, (b) inverted and (c) true velocity models. . . . .	59
Figure 3.16	The common-shot gather seismograms of the noise-contaminated Marmousi data set with Gaussian random noise: S/N ratio of (a) 12.75 and (b) 25.50. . . . .	62
Figure 3.17	The inverted velocity models for the noise-contaminated Marmousi data set with Gaussian random noise: S/N ratio of (a) 12.75 and (b) 25.50. . . . .	63

Figure 3.18	The common-shot gather seismograms of noise-contaminated Marmousi data set with Gaussian random noise: S/N ratio of 12.75 for the (a) 50th, (b) 100th and (c) 150th shot (source located at 2.4 km , 4.8 km and 7.2 km). . . . .	64
Figure 3.19	The synthetic common-shot gather seismograms recovered by the waveform inversion of noise-contaminated Marmousi data set with Gaussian random noise: S/N ratio of 12.75 for the (a) 50th, (b) 100th and (c) 150th shot (source located at 2.4 km , 4.8 km and 7.2 km). . . . .	65
Figure 3.20	The common-shot gather seismograms of noise-contaminated Marmousi data set with Gaussian random noise: S/N of ratio 25.50 for the (a) 50th, (b) 100th and (c) 150th shot (source located at 2.4 km , 4.8 km and 7.2 km). . . . .	66
Figure 3.21	The synthetic common-shot gather seismograms recovered by the waveform inversion of noise-contaminated Marmousi data set with Gaussian random noise: S/N ratio of 25.50 for the (a) 50th, (b) 100th and (c) 150th shot (source located at 2.4 km , 4.8 km and 7.2 km). . . . .	67
Figure 3.22	The inverted velocity models with frequency components starting from (a) 2 Hz, (b) 4 Hz and (c) 6 Hz. . . . .	71
Figure 3.23	The initial velocity models for the waveform inversion: (a) homogeneous velocity model of 3 km/s, (b) linearly increasing velocity model ranging from 1.5 to 4.5 km/s and (c) smoothed velocity model. . . . .	74

Figure 3.24 The inverted velocity models started with the initial velocity models: (a) homogeneous velocity model of 3 km/s, (b) linearly increasing velocity model ranging from 1.5 to 4.5 km/s and (c) smoothed velocity model. . . . . 75

Figure 3.25 The common-shot gather seismograms of 100th shot: synthetic seismograms for the inverted velocity models started with the (a) homogeneous, (b) linearly increasing and (c) smoothed velocity models. . . . . 76

Figure 3.26 The comparison of traces from the common-shot gather seismograms of 100th shot for the inverted velocity models started with the homogeneous (solid), linearly increasing (dashed with '+' marker) and smoothed (dashed with × marker) velocity models. The receivers are located at the distance of (a) 3.6 km, (b) 6.0 km and (c) 8.4 km. . . . . 77

Figure 3.26 (continued) The comparison of traces from the common-shot gather seismograms of 100th shot for the inverted velocity models started with the homogeneous (solid), linearly increasing (dashed with '+' marker) and smoothed (dashed with × marker) velocity models. The receivers are located at the distance of (a) 3.6 km, (b) 6.0 km and (c) 8.4 km. . . . . 78

Figure 3.26	(continued) The comparison of traces from the common-shot gather seismograms of 100th shot for the inverted velocity models started with the homogeneous (solid), linearly increasing (dashed with '+' marker) and smoothed (dashed with × marker) velocity models. The receivers are located at the distance of (a) 3.6 km, (b) 6.0 km and (c) 8.4 km. . . . .	79
Figure 3.27	The migration images for the initial velocity models: (a) homogeneous velocity model of 3 km/s, (b) linear-increasing velocity model from 1.5 to 4.5 km/s and (c) smoothed velocity model. . . . .	80
Figure 3.28	The migration images for the inverted velocity models updated from the initial velocity models: (a) homogeneous velocity model of 3 km/s, (b) linearly increasing velocity model from 1.5 to 4.5 km/s and (c) smoothed velocity model. . . . .	81
Figure 3.29	(a) A common-shot gather seismogram and (b) a frequency spectrum of the Gulf of Mexico field data set. . . . .	83
Figure 3.30	The initial velocity model for the waveform inversion of the Gulf of Mexico data set. . . . .	84
Figure 3.31	The inverted velocity model for the waveform inversion of the Gulf of Mexico data set. . . . .	85
Figure 3.32	The common-shot gather seismograms of the 210th shot of the Gulf of Mexico data set: (a) synthetic seismogram recovered by the waveform inversion and (b) frequency-filtered seismogram of the real field data. . . . .	87

Figure 3.33	The common-shot gather seismograms of the 250th shot of the Gulf of Mexico data set: (a) synthetic seismogram recovered by the waveform inversion and (b) frequency-filtered seismogram of the real field data. . . . .	88
Figure 3.34	The common-shot gather seismograms of the 300th shot of the Gulf of Mexico data set: (a) synthetic seismogram recovered by the waveform inversion and (b) frequency-filtered seismogram of the real field data. . . . .	89
Figure 3.35	The common-shot gather seismograms of the 350th shot of the Gulf of Mexico data set: (a) synthetic seismogram recovered by the waveform inversion and (b) frequency-filtered seismogram of the real field data. . . . .	90
Figure 3.36	The frequency spectrums after the low-pass and high-pass filter is applied: (a) a trapezoidal low-pass filter of 0-4-10-20 Hz and (b) a trapezoidal high-pass filter of 10-20-40-60 Hz. . . . .	92
Figure 3.37	The inverted velocity model for the waveform inversion of the Gulf of Mexico data set: 2 to 16 Hz frequency components are employed with interval 0.5 Hz without frequency filtering. . . . .	93
Figure 3.38	The inverted velocity model for the waveform inversion of the Gulf of Mexico data set: 4 to 16 Hz frequency components are employed with 0.15 Hz interval after the data set is filtered with a trapezoidal low-pass filter of 0-4-10-20 Hz. . . . .	94

Figure 3.39	The inverted velocity model for the waveform inversion of the Gulf of Mexico data set: 20 to 32 Hz frequency components are employed with 0.15 Hz interval after the data set is filtered with a trapezoidal high-pass filter of 10-20-40-60 Hz. . . . .	95
Figure 3.40	(a) A common-shot gather seismogram and (b) a frequency spectrum of the TOTAL data set. . . . .	97
Figure 3.41	The initial velocity model for the waveform inversion of the TOTAL data set. . . . .	98
Figure 3.42	The inverted velocity model for the waveform inversion of the TOTAL data set. . . . .	99
Figure 3.43	The common-shot gather seismograms of the 200th shot of the TOTAL data set: (a) synthetic seismogram recovered by the waveform inversion and (b) frequency-filtered seismogram of the real field data. . . . .	100
Figure 3.44	The common-shot gather seismograms of the 600th shot of the TOTAL data set: (a) synthetic seismogram recovered by the waveform inversion and (b) frequency-filtered seismogram of the real field data. . . . .	101
Figure 3.45	The common-shot gather seismograms of the 1000th shot of the TOTAL data set: (a) synthetic seismogram recovered by the waveform inversion and (b) frequency-filtered seismogram of the real field data. . . . .	102

# 1. Introduction

First, full-waveform inversion (FWI) is briefly reviewed as a tomographic method to extract the physical properties of subsurface media from exploration seismic data. Furthermore, I introduce scattering theory and the Lippmann-Schwinger equation, which serve as the basis of waveform inversion in this study. Then, I propose a new waveform inversion method to directly estimate medium perturbation, as a difference between the actual medium of interest and the initial guess model of medium, by solving the inverse scattering problem.

## 1.1 Full-waveform inversion

In seismic data processing, the forward problem inputs the physical properties of the medium and source character and outputs the wavefield propagation everywhere inside and outside the medium of interest. In contrast, the inverse problem inputs measurements of the wavefield outside the medium of interest and the source character and outputs processing goals that include locating structure/reflectors at their correct spatial location and identifying changes in the Earth's mechanical properties across the imaged reflectors (Weglein et al., 2009).

Seismic tomography, which is solved as an inverse problem, is a tool for imaging the Earth's interior (Nolet, 1987; Woodward, 1992; Trampert, 1998; Tromp et al., 2005; Woodward et al., 2008; Rawlinson et al., 2010). Global seismologists have researched seismic tomography to investigate the global-scale structure inside the Earth through passive methods, including analyzing signals from natural earthquakes. Exploration geophysicists have developed seismic tomography techniques to identify gas or oil reservoirs in the upper crust of the Earth from exploration seismic data. Traveltime tomography is generally used to produce a background velocity model for migrations in exploration geophysics (Varela et al., 1998; Brenders and Pratt, 2007). Of the various seismic tomography methods available, waveform tomography exploits the full potential of seismic data (Ravaut et al., 2004). Waveform tomography (Pratt, 1999) is also known as full-waveform inversion (FWI) and has advanced with improvements in computing technology.

FWI is a data-fitting procedure that uses full-wavefield modeling to extract quantitative information from seismograms (Lailly, 1983; Tarantola, 1984; Virieux and Operto, 2009). In other words, FWI is the process of fitting synthetic mod-

eled data to seismic field data by updating the appropriate medium parameters to optimize this fit (Guitton and Alkhalifah, 2013). FWI has attracted the attention of academia and industry as a cutting-edge technique in seismic data processing and has proven itself as a valuable tool for updating and improving the accuracy of subsurface velocity models (Vigh et al., 2013). FWI methods have been developed in the time (Tarantola, 1984; Gauthier et al., 1986; Mora, 1987; Shipp and Singh, 2002) and frequency (Pratt, 1990; Geller and Hara, 1993; Pratt et al., 1998) domains. Since Shin and Cha (2008, 2009) developed the Laplace and Laplace-Fourier domain FWI method, long-wavelength velocity models can be built from scratch using the FWI technique with field data lacking low frequencies.

The key aspects of FWI are an efficient forward modeling engine and a local differential approach (Virieux and Operto, 2009). The most affordable and popular process of FWI is the gradient-based method, in which the model is updated iteratively by following the local descent direction or gradient (Guitton and Alkhalifah, 2013). Gradient-based FWI in the frequency domain can provide velocity models with imaging of high spatial resolution at half the propagated wavelength (Virieux and Operto, 2009). However, FWI possesses difficulties related to the ill-posedness and nonlinearity of the inverse problem, the limited and poor illumination of the subsurface, the anelastic and anisotropic nature of the Earth, and the computational cost for its performance, etc (Guitton and Alkhalifah, 2013). In particular, because that FWI is an approach based on the local optimization method, a problem exists regarding the potential of solutions to converge to the wrong solutions of local minima if the initial estimation model is far from the global minima (Mora, 1987).

FWI is an indirect inversion method that seeks to search, locally and globally,

and consider possible candidates that emulate a characteristic, property or invariance that a direct solution would automatically satisfy (Weglein et al., 2009). As a gradient-based method, FWI requires scaling of the gradient by step length with a Hessian (or pseudo-/approximate Hessian) matrix to update the initial estimation of the subsurface medium with velocity perturbation. In this study, I propose a waveform inversion method based on the Lippmann-Schwinger equation; the method is called Lippmann-Schwinger waveform inversion (LSWI). LSWI solves the inverse scattering problem to directly estimate the difference between the actual medium of interest and the initial medium guess. Based on the scattering and perturbation theories, LSWI estimates the perturbation of slowness (i.e., the square of slowness) as medium perturbation instead of velocity itself.

## 1.2 Scattering theory and inverse scattering problem

Scattering theory is a form of perturbation analysis that describes how a perturbation in the properties of a medium relates a perturbation to a wavefield that experiences that perturbed medium (Weglein et al., 2003). The difference between the actual and reference media is characterized by the perturbation operator, whereas the corresponding difference between the actual and reference wavefields is referred to as the scattered wavefield. Forward scattering inputs the reference medium, the reference wavefield and the perturbation operator and outputs the actual wavefield. Inverse scattering inputs the reference medium, the reference wavefield and the values of the actual field on the measurement surface and outputs the difference between the actual and reference medium properties through the perturbation operator. The inverse scattering series was introduced to many studies, including Born–WKBJ (Wentzel–Kramers–Brillouin–Jeffreys) inversion (Clayton and Stolt, 1981), linearized inversion (Beylkin, 1985; Beylkin and Burridge, 1990), AVA (amplitude versus angle) inversion (Amundsen et al., 2006), multiple attenuation (Weglein et al., 1997, 2003), deghosting (Ikelle, 1999), downward continuation (Stolk and de Hoop, 2006), Born series forward modeling (Innanen, 2009) and the inversion of 1D acoustic and elastic media (Zhang and Weglein, 2009a,b).

The waveform inversion method in this study is based on the scattering and perturbation theories, which can decompose the actual medium into a reference medium and medium perturbation (Ikelle and Amundsen, 2005). The problem of determining the Earth’s material properties from seismic reflection data is an inverse scattering problem and, specifically, a nonlinear inverse scattering problem (Weglein et al., 2003). Zhang and Weglein (2009a,b) proposed a direct nonlinear

inversion of 1D acoustic and elastic media, but they exclusively considered reflection data with reference medium information. However, the waveform inversion method in this study is a direct inversion method with a forward modeling of the wave equation that can simulate all of the wave propagation, such as reflection, refraction, diffraction, etc., in the subsurface media. Furthermore, the perturbation of slowness (i.e., the square of slowness) is adopted as a solution of the inverse scattering problem because of the linear relationship between the slowness and pressure wavefield.

### 1.3 The Lippmann-Schwinger equation

The Lippmann-Schwinger equation (Lippmann and Schwinger, 1950) was introduced to present the application of variational principles to the quantum theory of scattering (Taylor, 1972). In seismic data processing, the Lippmann-Schwinger equation is the fundamental equation for inverse scattering techniques to determine the unknown parameters of subsurface media from seismic data acquired above the medium of interest. In general, one cannot analytically determine Green's function for arbitrary inhomogeneous media. Accordingly, the solutions of the inverse scattering problem are cast as a perturbation about a simpler reference problem for which analytic solutions for Green's functions are available, or at least can be easily computed (Ikelle and Amundsen, 2005).

The Lippmann-Schwinger equation, which is the desired integral solution for the acoustic wave-scattering problem (Lo and Inderwiesen, 1994), can be written as follows:

$$P_s(\mathbf{r}) = -k_0^2 \int G(\mathbf{r}|\mathbf{r}')M(\mathbf{r}')[P_i(\mathbf{r}') + P_s(\mathbf{r}')] d\mathbf{r}', \quad (1.1)$$

where  $P_s(\mathbf{r})$  is the scattered wavefield,  $P_i(\mathbf{r})$  is the incident wavefield,  $k_0$  is the magnitude of the wavenumber and  $M(\mathbf{r}')$  is the model function of medium perturbation. The sum of the incident and scattered wavefields in the integrand is referred to as the total wavefield. Green's function  $G(\mathbf{r}|\mathbf{r}')$  provides the solution at position  $\mathbf{r}$  for a negative impulse at  $\mathbf{r}'$ , which corresponds to the location of a point scatterer. The Lippmann-Schwinger equation nonlinearly relates the data function  $P_s(\mathbf{r})$ , referred to as the scattered wavefield, to the model function  $M(\mathbf{r})$  (Lo and Inderwiesen, 1994). The nonlinearity is a result of the scattered wavefield

$P_s(\mathbf{r})$  inside the integrand of Eq. (1.1) whose value depends on the model function  $M(\mathbf{r})$ . Given this nonlinearity, it is difficult to use the equation to perform forward modeling while resorting to computationally extensive approaches, such as finite difference methods, or to derive diffraction tomography image reconstruction algorithms. However, I use the Lippmann-Schwinger equation to formulate the virtual scattering source as a substitute for the scattering source term (the product of the model function  $M(\mathbf{r})$  and total wavefield  $[P_i(\mathbf{r}) + P_s(\mathbf{r})]$  in Eq. (1.1)) in the proposed waveform inversion method. Accordingly, nonlinearity is not considered in the waveform inversion because of the relationship between the scattered wavefield and the virtual scattering source.

In this study, Lippmann-Schwinger waveform inversion (LSWI) employs forward modeling of the wave equation, similar to FWI. However, LSWI does not use a local optimization approach that FWI exploits to search descent directions and, therefore, does not take advantage of misfit function of the data residuals. Instead, LSWI utilizes the data residual to formulate the virtual scattering source and to reconstruct the scattered wavefield using the Lippmann-Schwinger equation. Therefore, LSWI updates the velocity model once per single frequency, whereas FWI generally requires iterative updates for each of the frequency components. Moreover, LSWI reconstructs the total wavefield as an approximation of the actual wavefield simultaneously during the inversion procedure, whereas FWI requires additional forward modeling.

## 1.4 Outline

In the following sections, I derive the Lippmann-Schwinger equation of seismic scattering from the scattering and perturbation theories. Section 2 describes the theory and algorithm of Lippmann-Schwinger waveform inversion (LSWI). The detailed procedure of LSWI is presented with an illustration of the workflow. In Section 3, I demonstrate the feasibility of the waveform inversion method as an inverse scattering problem with numerical examples of synthetic and real seismic field data. I also discuss several problems that should be considered when this method is applied to real field data sets in Section 4. The thesis is concluded with a summary of this study and future research topics.



## 2. Theory

In this section, I introduce the theory and algorithm of Lippmann-Schwinger waveform inversion (LSWI). First, I derive the Lippmann-Schwinger equation of seismic scattering from the perturbation and scattering theories in Section 2.1. Second, I describe the waveform inversion method used to estimate medium perturbation from seismic data based on the Lippmann-Schwinger equation in Section 2.2.

The procedure of waveform inversion method is presented in Section 2.3. The procedure starts with performing the forward modeling of the reference model to obtain reference wavefield and data, presented in Section 2.3.1. The modified Lippmann-Schwinger equation is employed to formulate the virtual scattering source from the data residual in Section 2.3.2. Then, the scattered wavefield is reconstructed by the propagation of the virtual scattering source in the reference model and obtains the total wavefield in Section 2.3.3. Newton's optimization method is exploited to obtain the slowness perturbation from the virtual scattering sources and total wavefields, presented in Section 2.3.4. Last, the method for updating the reference model with slowness perturbation is described in Section 2.3.5.

## 2.1 Lippmann-Schwinger equation of seismic scattering

In this section, I derive the Lippmann-Schwinger equation of seismic scattering based on the perturbation and scattering theories (Lo and Inderwiesen, 1994; Ikelle and Amundsen, 2005). On the basis of perturbation theory, I assume that the actual medium parameters can be divided into the parameters of reference medium and medium perturbation:

$$\kappa(\mathbf{x}) = \kappa_0(\mathbf{x}) + \Delta\kappa(\mathbf{x}), \quad (2.1)$$

and

$$\sigma(\mathbf{x}) = \sigma_0(\mathbf{x}) + \Delta\sigma(\mathbf{x}). \quad (2.2)$$

$\kappa$  and  $\sigma$  represent the compressibility (i.e., reciprocal of bulk modulus) and specific volume (i.e., reciprocal of density) of the actual medium. The parameters of the reference medium are denoted as  $\kappa_0$  and  $\sigma_0$ , and the parameters of the medium perturbation are denoted as  $\Delta\kappa$  and  $\Delta\sigma$ . The wave propagations in the actual and reference media satisfy the following equations in the frequency domain:

$$L(\mathbf{x}, \omega) G(\mathbf{x}, \omega; \mathbf{x}_s) = -\delta(\mathbf{x} - \mathbf{x}_s), \quad (2.3)$$

and

$$L_0(\mathbf{x}, \omega) G_0(\mathbf{x}, \omega; \mathbf{x}_s) = -\delta(\mathbf{x} - \mathbf{x}_s). \quad (2.4)$$

where  $\omega$  is a temporal angular frequency and  $\delta$  is the Dirac's delta function.  $L(\mathbf{x}, \omega)$  and  $L_0(\mathbf{x}, \omega)$  are the differential operators for the actual and reference media:

$$L(\mathbf{x}, \omega) = \omega^2 \kappa(\mathbf{x}) + \nabla \cdot \sigma(\mathbf{x}) \nabla, \quad (2.5)$$

and

$$L_0(\mathbf{x}, \omega) = \omega^2 \kappa_0(\mathbf{x}) + \nabla \cdot \sigma_0(\mathbf{x}) \nabla. \quad (2.6)$$

$G(\mathbf{x}, \omega; \mathbf{x}_s)$  and  $G_0(\mathbf{x}, \omega; \mathbf{x}_s)$  are Green's functions at location  $\mathbf{x}$  in the whole medium where the source is located at  $\mathbf{x}_s$  in the actual and reference media, respectively. In other words, Eqs. (2.3) and (2.4) describe the impulse response of the actual and reference media in the frequency domain. The pressure wavefields  $p$  and  $p_0$  for the actual and reference media with the source signature of  $a(\omega)$  can be represented as follows:

$$L(\mathbf{x}, \omega) p(\mathbf{x}, \omega; \mathbf{x}_s) = -a(\omega) \delta(\mathbf{x} - \mathbf{x}_s), \quad (2.7)$$

and

$$L_0(\mathbf{x}, \omega) p_0(\mathbf{x}, \omega; \mathbf{x}_s) = -a(\omega) \delta(\mathbf{x} - \mathbf{x}_s). \quad (2.8)$$

Equations (2.7) and (2.8) describe the seismic response of pressure wavefields  $p(\mathbf{x}, \omega; \mathbf{x}_s)$  and  $p_0(\mathbf{x}, \omega; \mathbf{x}_s)$  at location  $\mathbf{x}$  where the source is located at  $\mathbf{x}_s$  with source signature  $a(\omega)$  in the actual and reference media, respectively.

Based on the perturbation of the medium parameters, the differential operator for the actual medium,  $L(\mathbf{x}, \omega)$ , can be decoupled as follows:

$$L(\mathbf{x}, \omega) = L_0(\mathbf{x}, \omega) + \Delta L(\mathbf{x}, \omega), \quad (2.9)$$

$$\text{where } \Delta L(\mathbf{x}, \omega) = \omega^2 \Delta \kappa(\mathbf{x}) + \nabla \cdot \Delta \sigma(\mathbf{x}) \nabla.$$

$\Delta L(\mathbf{x}, \omega)$  is the perturbation operator that relates the medium parameter perturbation and the perturbed wavefield. Substituting Eq. (2.9) into Eq. (2.7) yields

$$L_0(\mathbf{x}, \omega) p(\mathbf{x}, \omega; \mathbf{x}_s) = -a(\omega) \delta(\mathbf{x} - \mathbf{x}_s) - \Delta L(\mathbf{x}, \omega) p(\mathbf{x}, \omega; \mathbf{x}_s). \quad (2.10)$$

The right-hand side of Eq. (2.10) is equivalent to a source that generates the actual pressure wavefield  $p(\mathbf{x}, \omega; \mathbf{x}_s)$  by the differential operator of the reference medium  $L_0(\mathbf{x}, \omega)$ . The reference pressure wavefield  $p_0(\mathbf{x}, \omega; \mathbf{x}_s)$  in Eq. (2.8) can be written as an integral solution with Green's function:

$$p_0(\mathbf{x}, \omega; \mathbf{x}_s) = \int_D G_0(\mathbf{x}, \omega; \mathbf{x}') [a(\omega) \delta(\mathbf{x}' - \mathbf{x}_s)] d\mathbf{x}'. \quad (2.11)$$

Therefore, the actual pressure wavefield  $p(\mathbf{x}, \omega; \mathbf{x}_s)$  can be expressed as a convolution of the Green's function  $G_0$  and the source term of Eq. (2.10):

$$p(\mathbf{x}, \omega; \mathbf{x}_s) = \int_D G_0(\mathbf{x}, \omega; \mathbf{x}') [a(\omega) \delta(\mathbf{x}' - \mathbf{x}_s) + \Delta L(\mathbf{x}', \omega) p(\mathbf{x}', \omega; \mathbf{x}_s)] d\mathbf{x}'. \quad (2.12)$$

In Eq. (2.12), the first term in the integral  $G_0(\mathbf{x}, \omega; \mathbf{x}') a(\omega) \delta(\mathbf{x}' - \mathbf{x}_s)$  can be substituted with the reference pressure wavefield  $p_0(\mathbf{x}, \omega; \mathbf{x}_s)$ . Accordingly, Eq. (2.12) can be rewritten as follows:

$$p(\mathbf{x}, \omega; \mathbf{x}_s) - p_0(\mathbf{x}, \omega; \mathbf{x}_s) = \int_D G_0(\mathbf{x}, \omega; \mathbf{x}') \Delta L(\mathbf{x}', \omega) p(\mathbf{x}', \omega; \mathbf{x}_s) d\mathbf{x}'. \quad (2.13)$$

Equation (2.13) is known as the Lippmann-Schwinger equation, which describes the relationship between the scattered wavefields and medium perturbation. The left-hand side of Eq. (2.13) presents the scattered (perturbed) wavefield:

$$\Delta p(\mathbf{x}, \omega; \mathbf{x}_s) = p(\mathbf{x}, \omega; \mathbf{x}_s) - p_0(\mathbf{x}, \omega; \mathbf{x}_s). \quad (2.14)$$

The right-hand side term in the integral,  $\Delta L(\mathbf{x}', \omega) p(\mathbf{x}', \omega; \mathbf{x}_s)$ , is the scattering source term that relates medium perturbation to the scattered wavefield.

## 2.2 Waveform inversion based on the Lippmann-Schwinger equation

In seismic applications, the inverse scattering problem inputs the reference medium and the actual seismic data measured at receivers and outputs the medium perturbation (the difference between the actual and reference medium properties) through the perturbation operator (Weglein et al., 2003). Because geophysical data, including seismic data, can be acquired only at receiver positions (e.g., geophones or hydrophones located at the surface), it is impossible to measure the actual wavefield propagated in the whole medium of interest. To overcome this limitation of data acquisition and to solve the inverse scattering problem, I modified the Lippmann-Schwinger equation of seismic scattering (Eq. (2.13) in Section 2.1) by introducing the virtual scattering source  $f^v$ :

$$p(\mathbf{x}_r, \omega; \mathbf{x}_s) - p_0(\mathbf{x}_r, \omega; \mathbf{x}_s) = \int_D G_0(\mathbf{x}_r, \omega; \mathbf{x}') f^v(\mathbf{x}', \omega; \mathbf{x}_s) d\mathbf{x}', \quad (2.15)$$

where  $\mathbf{x}_r$  denotes the receiver positions. The virtual scattering source  $f^v(\mathbf{x}', \omega; \mathbf{x}_s)$  is defined as follows:

$$f^v(\mathbf{x}', \omega; \mathbf{x}_s) = \Delta L(\mathbf{x}', \omega) p(\mathbf{x}', \omega; \mathbf{x}_s). \quad (2.16)$$

$G_0(\mathbf{x}_r, \omega; \mathbf{x}')$  indicates the values of Green's function at the receiver positions, where the source is located at the arbitrary position  $\mathbf{x}'$  in the whole medium.  $f^v(\mathbf{x}', \omega; \mathbf{x}_s)$  is the virtual scattering source distributed in the whole medium. The left-hand side of Eq. (2.15) is referred to as the data residual, which is equivalent to the value of the scattered wavefield measured at the receiver positions:

$$\Delta p(\mathbf{x}_r, \omega; \mathbf{x}_s) = p(\mathbf{x}_r, \omega; \mathbf{x}_s) - p_0(\mathbf{x}_r, \omega; \mathbf{x}_s). \quad (2.17)$$

The data residual is equivalent to the difference between the actual and reference data. In this study, the virtual scattering source is formulated from the data residual by the modified Lippmann-Schwinger equation, Eq. (2.15).

The main purpose of this waveform inversion method (LSWI) is to estimate the medium perturbation through the perturbation operator  $\Delta L$ . As shown in Fig. 2.1, the virtual scattering source formulated from the data residual,  $f^v$ , can be used to reconstruct the scattered wavefield  $\Delta p(\mathbf{x}, \omega; \mathbf{x}_s)$  by propagating it in the reference medium. The scattered wavefield can be represented by rewriting Eq. (2.13) with the Green's function  $G_0$ :

$$\Delta p(\mathbf{x}, \omega; \mathbf{x}_s) = \int_D G_0(\mathbf{x}, \omega; \mathbf{x}') f^v(\mathbf{x}', \omega; \mathbf{x}_s) d\mathbf{x}'. \quad (2.18)$$

Then, the actual wavefield  $p(\mathbf{x}, \omega; \mathbf{x}_s)$  is approximated as the total wavefield by summing the reference wavefield  $p_0(\mathbf{x}, \omega; \mathbf{x}_s)$  and the scattered wavefield  $\Delta p(\mathbf{x}, \omega; \mathbf{x}_s)$ . The inversion method takes advantage of the total wavefield, as an approximation of actual wavefield, to solve for the perturbation operator  $\Delta L(\mathbf{x}, \omega)$  from the definition of the virtual scattering source in Eq. (2.16).

The derivation of the modified Lippmann-Schwinger equation, Eq. (2.15), for the virtual scattering source is based on the single scattering assumption. However, this derivation is different from the Born approximation of the Lippmann-Schwinger equation. The Born approximation substitutes the total wavefield in the integrand of the Lippmann-Schwinger equation (Eq. (2.13)) with the incident

(reference) wavefield (Lo and Inderwiesen, 1994). On the other hand, I introduce the virtual scattering source to substitute the product of the perturbation operator and the total wavefield, finally obtaining the approximation of the scattered wavefield by a simulation of the wave propagation (i.e., forward modeling). Nevertheless, the total wavefield cannot be recovered perfectly because the scattered wavefield is reconstructed by propagating the virtual scattering source in the reference medium, not in the actual medium, with the single scattering assumption.

In the proposed waveform inversion, the perturbation of slowness (i.e., square of slowness) is obtained through the perturbation operator with the virtual scattering sources and the reconstructed total wavefields. If the actual medium is known and the reference medium is similar to the actual medium, a decoupling of the actual and reference media can be kinematically correct through the perturbation operator. However, because the actual medium is unknown and medium identification is a goal of the waveform inversion, the slowness perturbation is estimated as an approximation of the correct slowness perturbation between the actual and reference media.

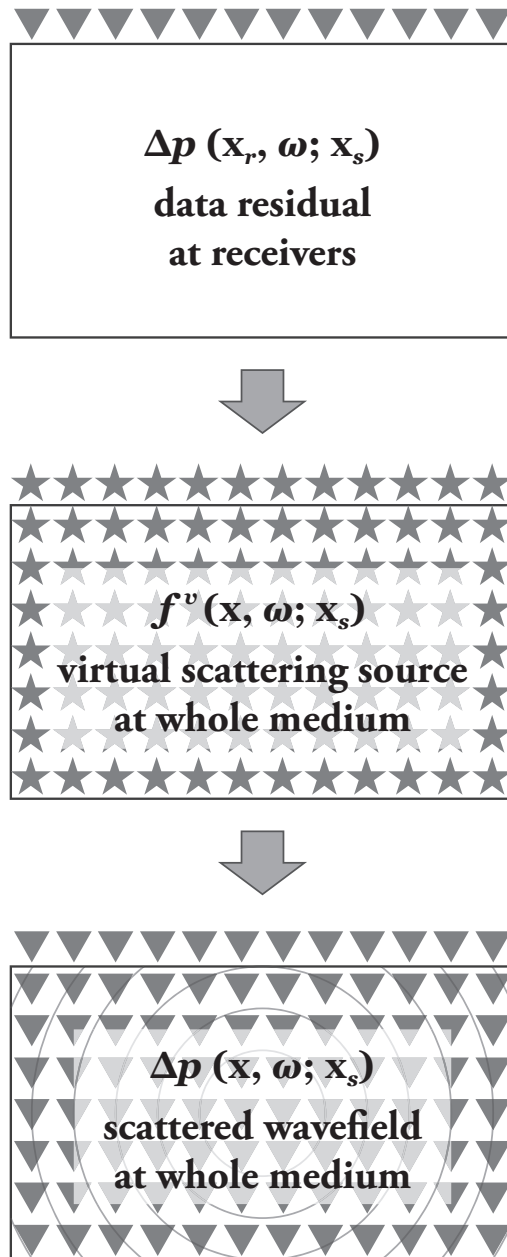


Figure 2.1 A diagram of the data residual, virtual scattering source and scattered wavefield. The inverted triangles and stars denote receivers and sources, respectively. The virtual scattering source is formulated to reconstruct the scattered wavefield from the data residual.

## 2.3 Waveform inversion procedure

In the previous sections, I briefly described the theory of seismic waveform inversion based on the Lippmann-Schwinger equation. The inversion procedure starts from the assumption that the actual model, as a mathematically defined medium of the Earth, can be divided into a reference model and model perturbation. The model perturbation is computed by the perturbation of slowness (i.e., square of slowness) through the perturbation operator. Details regarding the waveform inversion method are presented in the following sections.

First, forward modeling of the frequency-domain acoustic wave equation for the reference model is performed to obtain modeled data in Section 2.3.1. The data residual is computed as the difference between the forward-modeled data and the Fourier-transformed components of the input seismic data. In Section 2.3.2, the virtual scattering source is formulated from the data residual by using the modified Lippmann-Schwinger equation. Propagation of the virtual scattering source reconstructs the scattered wavefield in Section 2.3.3. Then, the actual wavefield can be approximated by the total wavefield which is the sum of the reference and scattered wavefields. In Section 2.3.4, the perturbation of slowness as the difference between the actual and reference models can be computed using Newton's optimization method from the definition of the virtual scattering source. Last, Section 2.3.5 shows how the reference model is updated with the computed slowness perturbation. The workflow of waveform inversion procedure is briefly illustrated in Fig. 2.2.

### 2.3.1 Forward modeling of the acoustic wave equation

The waveform inversion method exploits forward modeling as a simulation of wave propagation to obtain the synthetic seismic wavefield for a given subsurface model. The three-dimensional constant-density acoustic wave equation in the time domain is represented as a partial differential equation:

$$\left( \nabla^2 - \frac{1}{v(\mathbf{x})^2} \frac{\partial^2}{\partial t^2} \right) p(\mathbf{x}, t) = 0 \quad (2.19)$$

with

$$\nabla = \hat{\mathbf{i}} \frac{\partial}{\partial x} + \hat{\mathbf{j}} \frac{\partial}{\partial y} + \hat{\mathbf{k}} \frac{\partial}{\partial z}, \quad (2.20)$$

where  $v(\mathbf{x})$  is the P-wave velocity and  $p(\mathbf{x}, t)$  is the acoustic pressure wavefield in the time domain. The time-domain acoustic wave equation with a point source is

$$\left( \nabla^2 - \frac{1}{v(\mathbf{x})^2} \frac{\partial^2}{\partial t^2} \right) p(\mathbf{x}, t; \mathbf{x}_s) = -a(t) \delta(\mathbf{x} - \mathbf{x}_s), \quad (2.21)$$

where  $\mathbf{x}_s$  is a source position and  $a(t)$  is the time-domain source wavelet function for time  $t$ . A Fourier transform of Eq. (2.21) yields the frequency-domain acoustic wave equation as a Helmholtz equation:

$$\left( \nabla^2 + \frac{\omega^2}{v(\mathbf{x})^2} \right) p(\mathbf{x}, \omega; \mathbf{x}_s) = -a(\omega) \delta(\mathbf{x} - \mathbf{x}_s), \quad (2.22)$$

where  $a(\omega)$  is the source signature in the frequency domain and  $\omega$  is the temporal angular frequency. Equation (2.22) can be represented as follows:

$$L(\mathbf{x}, \omega) p(\mathbf{x}, \omega; \mathbf{x}_s) = -a(\omega) \delta(\mathbf{x} - \mathbf{x}_s), \quad (2.23)$$

where

$$L(\mathbf{x}, \omega) = \nabla^2 + \frac{\omega^2}{v(\mathbf{x})^2}. \quad (2.24)$$

The differential operator  $L(\mathbf{x}, \omega)$  includes sloth, which exhibits a linear relationship with the pressure wavefield  $p(\mathbf{x}, \omega; \mathbf{x}_s)$ .

Forward modeling of the wave equation employs the finite-difference or finite-element method to approximate the wavefield in the subsurface velocity model by the discretization of a continuum (Marfurt, 1984; Carcione et al., 2002; Zienkiewicz et al., 2005). The two-dimensional acoustic wave equation with a 2nd-order finite-difference scheme can be expressed as follows:

$$\frac{p_{x-\Delta x, z} - 2p_{x, z} + p_{x+\Delta x, z}}{\Delta x^2} + \frac{p_{x, z-\Delta z} - 2p_{x, z} + p_{x, z+\Delta z}}{\Delta z^2} + \frac{\omega^2 p_{x, z}}{v_{x, z}^2} = f_{x, z}, \quad (2.25)$$

where  $\Delta x = \Delta z = h$  is the spatial grid spacing and  $f_{x, z}$  is source signature at grid point  $x, z$ . Equation (2.25) can be expressed in a matrix form as follows:

$$\mathbf{L} \mathbf{p} = \mathbf{f}, \quad (2.26)$$

where the complex impedance matrix  $\mathbf{L}$  is an  $m \times m$  square matrix of the differential operator and  $m$  is the number of grid points in the subsurface velocity model.

The pressure wavefield vector  $\mathbf{p}$  and source vector  $\mathbf{f}$  are the column vectors with rows of  $m$ . The complex impedance matrix  $\mathbf{L}$  is a symmetric band matrix:

$$\mathbf{L} = \begin{bmatrix} \left(\frac{\omega^2}{v_1^2} - \frac{4}{h^2}\right) & \frac{1}{h^2} & & & & & \\ & \ddots & & & & & \\ & & \frac{1}{h^2} & \frac{1}{h^2} & \left(\frac{\omega^2}{v_k^2} - \frac{4}{h^2}\right) & \frac{1}{h^2} & \frac{1}{h^2} \\ & & & & & \ddots & \\ & & & & & & \frac{1}{h^2} & \frac{1}{h^2} & \left(\frac{\omega^2}{v_m^2} - \frac{4}{h^2}\right) \end{bmatrix}, \quad (2.27)$$

where  $v_k$  denotes the P-wave velocity at the  $k$ -th grid point in the velocity model.

The pressure wavefield vector  $\mathbf{p}$  is

$$\mathbf{p} = \begin{bmatrix} p_1 \\ \vdots \\ p_k \\ \vdots \\ p_m \end{bmatrix}, \quad (2.28)$$

where  $p_k$  denotes the value of the frequency-domain pressure wavefield at the  $k$ -th grid point in the velocity model. The source vector  $\mathbf{f}$  is

$$\mathbf{f} = \begin{bmatrix} f_1 \\ \vdots \\ f_k \\ \vdots \\ f_m \end{bmatrix}, \quad (2.29)$$

where  $f_k$  denotes the value of the source signature at the  $k$ -th grid point in the medium for frequency  $\omega$ . Forward modeling by solving Eq. (2.26) with a matrix solver provides the pressure wavefield vector  $\mathbf{p}$ .

Assuming that Eq. (2.26) represents the forward modeling for the actual velocity model, which is a mathematically defined medium of interest, then  $\mathbf{p}$  approximates the actual pressure wavefield. The value of the actual wavefield at the receiver positions can be considered as the recorded seismic data acquired from a field exploration. In other words, the seismic data measured  $p(\mathbf{x}_r, \omega; \mathbf{x}_s)$  can be extracted from the actual wavefield  $p(\mathbf{x}, \omega; \mathbf{x}_s)$  at the receiver positions:

$$\mathbf{p}' = \mathbf{I}_{nm}\mathbf{p}, \quad (2.30)$$

where  $\mathbf{p}'$  is the vector of measured seismic data, and  $n$  is the number of receivers. The projection matrix  $\mathbf{I}_{nm}$  is

$$\mathbf{I}_{nm} = \begin{bmatrix} \delta_1 & & & & \\ & \ddots & & & \\ & & \delta_k & & \\ & & & \ddots & \\ & & & & \delta_m \end{bmatrix}, \quad (2.31)$$

$$\text{where } \delta_k = \begin{cases} 1 & \text{if the } k\text{-th grid point is a receiver point,} \\ 0 & \text{if the } k\text{-th grid point is not a receiver point.} \end{cases}$$

The projection matrix  $\mathbf{I}_{nm}$  is an  $m \times m$  diagonal matrix with diagonal elements of 1 or 0. The projection matrix is dependent on the grid point indexing. Herein,

I assume that the first to the  $n$ -th grid points correspond to the surface receiver nodes for simple notation. Then, the projection matrix  $\mathbf{I}_{nm}$  can be modified into an  $n \times m$  rectangular matrix with the simple numbering of receiver nodes:

$$\mathbf{I}_{nm} = \begin{bmatrix} \mathbf{I}_n \\ \mathbf{0} \end{bmatrix}, \quad (2.32)$$

where  $\mathbf{I}_n$  is an  $n \times n$  identity matrix. Accordingly, the vector of measured seismic data  $\mathbf{p}'$  can be represented as follows:

$$\mathbf{p}' = \mathbf{I}_{nm}\mathbf{p} = \begin{bmatrix} p_1 \\ \vdots \\ p_n \end{bmatrix}. \quad (2.33)$$

For the frequency-domain waveform inversion of the real seismic field data set, the frequency-domain seismic data components are obtained by the Fourier transform of the time-domain seismic data.

The frequency-domain waveform inversion starts from a reference velocity model, because the inversion estimates the model perturbation between the actual and reference models from the measured seismic data. The inversion method first performs the forward modeling of the impulse response for the reference model prior to the source wavelet estimation. Next, the inversion method uses the source wavelet estimation technique proposed by Shin et al. (2007) to obtain the source signature analogous to that for the actual wave propagation. Assuming that the estimated source signature is identical to that for the actual wavefield, the forward modeling of the reference wavefield can be written as follows:



$$\Delta \mathbf{p}' = \mathbf{p}' - \mathbf{p}'_0. \quad (2.37)$$



$$\mathbf{p}' - \mathbf{p}'_0 = \mathbf{I}_{nm} \mathbf{G}_0 \mathbf{f}^v, \quad (2.40)$$

where the virtual scattering source  $\mathbf{f}^v$  is the product of the perturbation operator  $\Delta\mathbf{L}$  and the actual wavefield  $\mathbf{p}$ .  $\mathbf{I}_{nm}$  is the projection matrix,  $m$  is the number of whole grid points and  $n$  is the number of receiver points.  $\mathbf{G}_0$  denotes Green's function matrix for the reference velocity model. The left-hand side of Eq. (2.40) is referred to as the data residual  $\Delta\mathbf{p}'$ . Then, Eq. (2.40) can be rewritten with the modified Green's function matrix  $\mathbf{G}_{nm} = \mathbf{I}_{nm} \mathbf{G}_0$ :

$$\mathbf{G}_{nm} \mathbf{f}^v = \Delta\mathbf{p}', \quad (2.41)$$

where the modified Green's function matrix  $\mathbf{G}_{nm}$  is an  $n \times m$  rectangular matrix:

$$\mathbf{G}_{nm} = \mathbf{I}_{nm} \mathbf{G}_0 = \begin{bmatrix} G_{11} & G_{12} & \cdots & G_{1m} \\ G_{21} & G_{22} & \cdots & G_{2m} \\ \vdots & \vdots & & \vdots \\ G_{n1} & G_{n2} & \cdots & G_{nm} \end{bmatrix}, \quad (2.42)$$

where  $G_{i,j}$  is the Green's function value measured at the  $i$ -th grid point where the source is exploded at the  $j$ -th grid point. I introduce the least-squares method to solve for the virtual scattering source vector  $\mathbf{f}^v$  from Eq. (2.41) and yield the normal equation as follows:

$$(\mathbf{G}_{nm})^* \mathbf{G}_{nm} \mathbf{f}^v = (\mathbf{G}_{nm})^* \Delta\mathbf{p}', \quad (2.43)$$

where  $*$  denotes the conjugate transpose of the matrix. Equation (2.43) can be

rewritten as follows:

$$\overline{(\mathbf{G}_{nm})}^T \mathbf{G}_{nm} \mathbf{f}^v = \overline{(\mathbf{G}_{nm})}^T \Delta \mathbf{p}'. \quad (2.44)$$

In addition, Eq. (2.44) can be represented with the elements:

$$\begin{bmatrix} \overline{G_{11}} & \overline{G_{21}} & \cdots & \overline{G_{n1}} \\ \overline{G_{12}} & \overline{G_{22}} & \cdots & \overline{G_{n2}} \\ \vdots & \vdots & & \vdots \\ \overline{G_{1m}} & \overline{G_{2m}} & \cdots & \overline{G_{nm}} \end{bmatrix} \begin{bmatrix} G_{11} & G_{12} & \cdots & G_{1m} \\ G_{21} & G_{22} & \cdots & G_{2m} \\ \vdots & \vdots & & \vdots \\ G_{n1} & G_{n2} & \cdots & G_{nm} \end{bmatrix} \begin{bmatrix} f_1^v \\ f_2^v \\ \vdots \\ f_m^v \end{bmatrix} \quad (2.45)$$

$$= \begin{bmatrix} \overline{G_{11}} & \overline{G_{21}} & \cdots & \overline{G_{n1}} \\ \overline{G_{12}} & \overline{G_{22}} & \cdots & \overline{G_{n2}} \\ \vdots & \vdots & & \vdots \\ \overline{G_{1m}} & \overline{G_{2m}} & \cdots & \overline{G_{nm}} \end{bmatrix} \begin{bmatrix} \Delta p'_1 \\ \Delta p'_2 \\ \vdots \\ \Delta p'_n \end{bmatrix},$$

where  $\Delta p'_i$  is the value of the data residual at the  $i$ -th grid point, and  $f_j^v$  is the value of the virtual scattering source at the  $j$ -th grid point. The lack of the scattered wavefield (only the data residual is known) to formulate the virtual scattering source is overcome by the reciprocity of Green's function. The numerical solution of Green's function matrix  $\mathbf{G}_0$  can be substituted by the inverse of the complex impedance matrix,  $\mathbf{L}_0^{-1}$ , as the forward modeling operator. Then, Eq. (2.44) is represented as follows:

$$\overline{(\mathbf{L}_0^{-1})}^T \mathbf{I}_{nm} (\mathbf{I}_{nm} \mathbf{L}_0^{-1}) \mathbf{f}^v = \overline{(\mathbf{L}_0^{-1})}^T \mathbf{I}_{nm} \Delta \mathbf{p}', \quad (2.46)$$

Matrix solvers cannot directly solve the conjugate of the inverse system matrix  $\overline{\mathbf{L}_0^{-1}}$ . I modified Eq. (2.46) to solve with a matrix solver as follows:

$$\overline{\left(\mathbf{L}_0^{-1T} (\mathbf{I}_{nm} \mathbf{L}_0^{-1} \mathbf{f}^v)\right)} = \overline{\mathbf{L}_0^{-1T} \Delta \mathbf{p}'}, \quad (2.47)$$

Equation (2.47) is solved with the generalized minimal residual (GMRES) solver (Frayssé et al., 2005) in this study. The GMRES solver is an iterative solver and cannot solve Eq. (2.47) without an additional matrix solver for the forward modeling. Therefore, Eq. (2.47) is numerically solved by combining the GMRES solver and a forward modeling matrix solver.

### 2.3.3 The scattered wavefield and total wavefield

In this section, I describe how to obtain the total wavefield as an approximation of the actual wavefield. The virtual scattering source is a stepping-stone to reconstruct the scattered wavefield from the data residual (i.e., scattered wavefield at the receiver positions) as presented in Fig. 2.1. After formulating virtual scattering sources in Section 2.3.2, the scattered wavefield can be reconstructed by the propagation of the virtual scattering sources in the reference velocity model. From Eq. (2.18) in Section 2.2, the scattered wavefield  $\Delta\mathbf{p}$  can be represented using the forward modeling operator  $\mathbf{L}_0^{-1}$ :

$$\Delta\mathbf{p} = \mathbf{L}_0^{-1} \mathbf{f}^v. \quad (2.48)$$

Here, the scattered wavefield is equivalent to the forward-modeled wavefield of the virtual scattering source in the reference velocity model. Then, as an approximation of the actual wavefield, the total wavefield can be reconstructed by summing the reference and scattered wavefields:

$$\mathbf{p} = \mathbf{p}_0 + \Delta\mathbf{p}. \quad (2.49)$$

The reconstructed total wavefield is not equivalent to the actual wavefield propagated in the actual velocity model due to the single scattering assumption. However, I replace the actual wavefield with the total wavefield reconstructed during the inversion procedure because the definition of the virtual scattering source includes the total wavefield itself.

### 2.3.4 The sloth perturbation

The perturbation of sloth can be computed as the perturbation operator from the virtual scattering sources and total wavefields. Computation of the sloth perturbation is inspired by the source estimation technique proposed by Shin et al. (2007). The perturbation operator  $\Delta\mathbf{L}$  can be derived from the definition of the virtual scattering source. Equation (2.16) in Section 2.2 can be represented in a matrix-vector form as follows:

$$\mathbf{f}^{\mathbf{v}} = \Delta\mathbf{L} \mathbf{p}. \quad (2.50)$$

The perturbation operator  $\Delta\mathbf{L}$  is a diagonal matrix whose diagonal elements include perturbations of sloth, as shown in Eq. (2.38) in Section 2.3.2. The virtual scattering source  $\mathbf{f}^{\mathbf{v}}$  and total wavefield  $\mathbf{p}$  are obtained for various shot positions for a single temporal frequency.

The inversion method takes advantage of the least squares method and Newton's method to estimate the perturbation of sloth for a single frequency component from the virtual scattering sources and scattered wavefields across various common-shot gathers. The matrix of the perturbation operator  $\Delta\mathbf{L}$ , virtual scattering source vector  $\mathbf{f}^{\mathbf{v}}$  and total wavefield vector  $\mathbf{p}$  have elements with complex number values:

$$\begin{aligned} \Delta L_k &= a + ib, \\ p_{k,j} &= c + id, \\ f_{k,j}^{\mathbf{v}} &= e + ig, \end{aligned} \quad (2.51)$$

where  $\Delta L_k$ ,  $p_{k,j}$  and  $f_{k,j}^{\mathbf{v}}$  are the elements of  $\Delta\mathbf{L}$ ,  $\mathbf{p}$  and  $\mathbf{f}^{\mathbf{v}}$  with respect to the  $k$ -th

grid point and  $j$ -th shot, respectively, and  $i$  is the imaginary unit. The variable of interest in the waveform inversion is  $a$ , the real part of  $\Delta L_k$ . The objective function for  $\Delta L_k$  is provided as follows:

$$E = \sum_j^{\text{shots}} \delta r_{k,j} \overline{\delta r_{k,j}}, \quad (2.52)$$

where the residual  $\delta r_{k,j}$  is

$$\delta r_{k,j} = \Delta L_k p_{k,j} - f_{k,j}^v. \quad (2.53)$$

Applying Newton's method to Equation (2.52) yields the following equation to update  $\Delta L_k$ :

$$(\Delta L_k)_{n+1} = (\Delta L_k)_n - \frac{\nabla E}{\nabla^2 E}, \quad (2.54)$$

where  $\nabla E$  is the first order partial derivative with respect to  $\Delta L_k$ :

$$\nabla E = \begin{bmatrix} \frac{\partial E}{\partial a} \\ \frac{\partial E}{\partial b} \end{bmatrix}, \quad (2.55)$$

and  $\nabla^2 E$  is the second order partial derivative with respect to  $\Delta L_k$ :

$$\nabla^2 E = \begin{bmatrix} \frac{\partial^2 E}{\partial a^2} & \frac{\partial^2 E}{\partial a \partial b} \\ \frac{\partial^2 E}{\partial b \partial a} & \frac{\partial^2 E}{\partial b^2} \end{bmatrix}. \quad (2.56)$$

Accordingly, Equation (2.54) can be rewritten as follows:

$$\begin{bmatrix} a_{n+1} \\ b_{n+1} \end{bmatrix} = \begin{bmatrix} a_n \\ b_n \end{bmatrix} - \frac{1}{\sum(c^2 + d^2)} \begin{bmatrix} \sum\{a_n(c^2 + d^2) + (ce + dg)\} \\ \sum\{b_n(c^2 + d^2) + (cg - de)\} \end{bmatrix}. \quad (2.57)$$

Because  $a_n$  and  $b_n$  on the right-hand side of Eq. (2.57) are canceled, the resultant equation is exclusively composed of  $c$ ,  $d$ ,  $e$ , and  $g$  on the right-hand side. Therefore,  $\Delta L_k$  can be represented as a complex number using  $f_k^v$  and  $p_k$ :

$$\Delta L_k = -\frac{\sum\{(ce + dg) + i(CG - de)\}}{\sum(c^2 + d^2)} = -\frac{\sum f_k^v \bar{p}_k}{\sum p_k \bar{p}_k}. \quad (2.58)$$

Equation (2.58) indicates that the computation of  $\Delta L_k$  does not require iterative updates. In addition, the square of the temporal frequency,  $\omega^2$ , should be canceled before updating the reference velocity model. Thus, the perturbation of slowness  $\Delta s_k$  is

$$\Delta s_k \equiv \frac{1}{v_k^2} - \frac{1}{(v_0)_k^2} = \text{Re} \left\{ \frac{\Delta L_k}{\omega^2} \right\}. \quad (2.59)$$

### 2.3.5 Updating of the velocity model

Section 2.3.4 presents how to compute the diagonal elements of the perturbation operator  $\Delta L_k$ . In this section, I describe how to update the reference velocity model with the computed perturbation of sloth. The element of the perturbation operator  $\Delta L_k$  includes the perturbation of sloth  $\Delta s_k$  with respect to the  $k$ -th grid point:

$$\Delta L_k = \omega^2 \left( \frac{1}{v_k^2} - \frac{1}{(v_0)_k^2} \right) = \omega^2 \Delta s_k, \quad (2.60)$$

where  $v$  and  $v_0$  are the P-wave velocity of the actual and reference velocity model, respectively. If the sloth perturbation  $\Delta s$  is estimated as demonstrated in Section 2.3.4, the reference velocity model can be updated with the following equation:

$$\frac{1}{v_k^2} = \frac{1}{(v_0)_k^2} + \Delta s_k. \quad (2.61)$$

The workflow of waveform inversion is briefly illustrated in Fig. 2.2. The procedure starts with the seismic data recorded by field survey and an initial guess of the velocity model as the reference velocity model. The reference wavefield is obtained by forward modeling with the estimated source signature in the reference velocity model. The data residual, which is the difference between seismic field data and modeled data, is exploited to formulate the virtual scattering source. The scattered wavefield is reconstructed by forward modeling of the virtual scattering source. The sum of the reference and scattered wavefields represents the total wavefield. The sloth perturbation is estimated through the perturbation operator from the virtual scattering source and total wavefield across various shots. The reference velocity model is updated using the computed sloth perturbation.

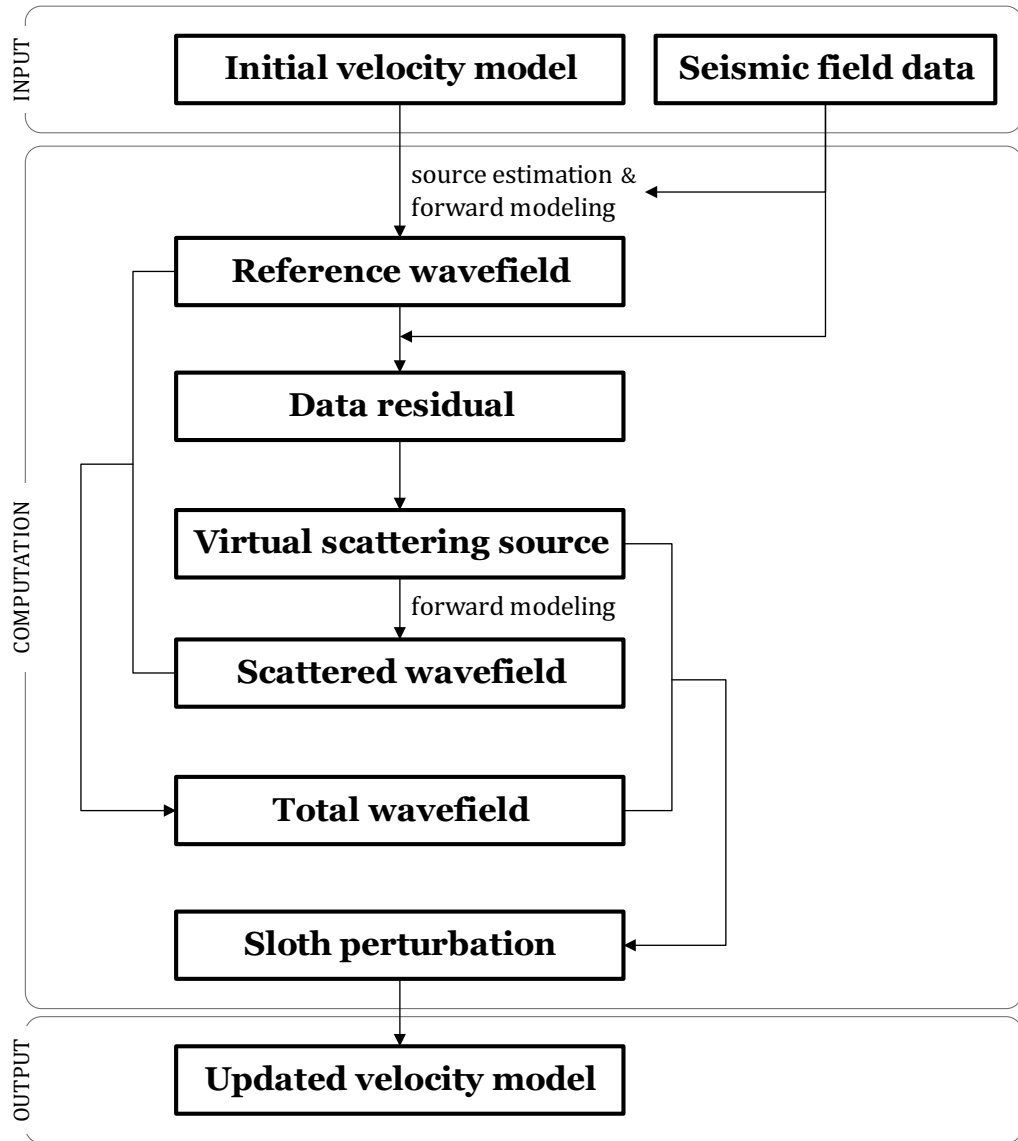


Figure 2.2 The workflow of Lippmann-Schwinger waveform inversion (LSWI).



## 3. Numerical examples

I demonstrated the Lippmann-Schwinger waveform inversion (LSWI) with the synthetic seismic data examples and the application to real field data. The procedure of LSWI is presented with the example of synthetic data for the Marmousi velocity model in Section 3.1. I also examined the effective factors for the solutions of LSWI in this study. The results of several sensitivity tests are provided in Sections 3.1.1 to 3.1.3. The waveform inversion method is implemented for a real field data set acquired at the Gulf of Mexico, and the results are presented in Section 3.2. In addition, an application of LSWI to the TOTAL data set is presented in Section 3.3.

### 3.1 Synthetic data example for the Marmousi model

I demonstrated LSWI by applying it to a synthetic data set from the Marmousi velocity model. The Marmousi model is based on a profile of real field data and has a deeper anticlinal structural trap of petroleum prospects (Versteeg, 1994). The P-wave velocity of the Marmousi model is depicted in Fig. 3.1.

The synthetic surface seismic data set was generated by the time-domain forward modeling of the acoustic wave equation with a fourth-order finite difference spatial approximation and a second-order finite difference temporal approximation. The data acquisition was simulated by 192 shots with an interval of 48 m. Each shot-gather seismogram contains 384 receivers with an interval of 24 m. Fig. 3.2 shows a common-shot gather seismogram and the frequency spectrum of the synthetic seismic data. The synthetic seismic data have a frequency spectrum that ranges from 0 to 40 Hz.

For the waveform inversion, the frequency-domain forward modeling is implemented with the finite-element method (Davies, 1980; Zienkiewicz et al., 2005) of spatial approximation with free surface and absorbing boundary conditions. The free surface condition on the top of the model is used to simulate an air-water interface with the Lloyd's mirror effect (Officer and Shrock, 1958). The absorbing boundary condition proposed by Clayton and Engquist (1977) is introduced to remove the unwanted artificial reflections on the left, right and bottom boundaries. The smoothed velocity structure of the Marmousi model presented in Fig. 3.3 is employed as an initial velocity model (i.e., starting velocity model). The grid spacing of the initial model is 24 m and the number of grid points is  $382 \times 126$ . The inversion procedure is performed with the 161 frequency components ranging

from 4.0 Hz to 20.0 Hz with a frequency interval of 0.1 Hz. The source signature is estimated from the seismic field data and forward-modeled data by using a source estimation technique proposed by Shin et al. (2007).

The forward modeling in the waveform inversion uses the multifrontal matrix solver proposed by Kim and Kim (1999) to solve the frequency-domain acoustic wave equation as a Helmholtz equation. Because the multifrontal matrix solver decomposes the inverse of the system matrix (e.g., complex impedance matrix) and stores it on random access memory (RAM), the system can solve for a multiple number of right-hand side vectors until destroying the matrix decomposition (i.e., removing the stored memory for the inverse of the complex impedance matrix). In addition, it is not necessary to write the inverse of the system matrix on the storage to formulate the virtual scattering source because multiplying the inverse matrix is equivalent to solving the system matrix with the given right-hand side vector. Therefore, the waveform inversion method does not require considerably more memory with gradient-based FWI.

Fig. 3.4 shows the frequency-domain wavefields propagated in the reference velocity model, which are referred to as the reference wavefields. The reference wavefield is produced by frequency-domain forward modeling of the estimated source signature in the reference velocity model. Frequency-domain modeled data are extracted from the value of the reference wavefield measured on receiver points located at the surface. Fig. 3.5 presents the data residuals which are the differences between the Fourier-transformed seismic field data and the forward-modeled data.

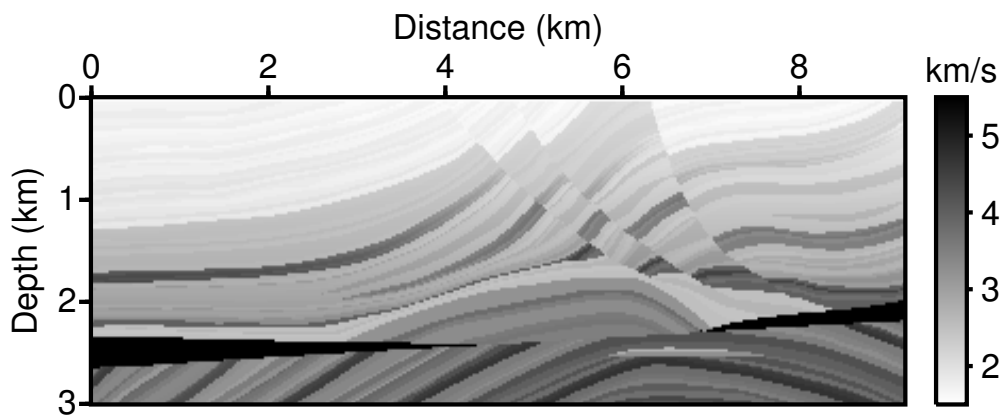
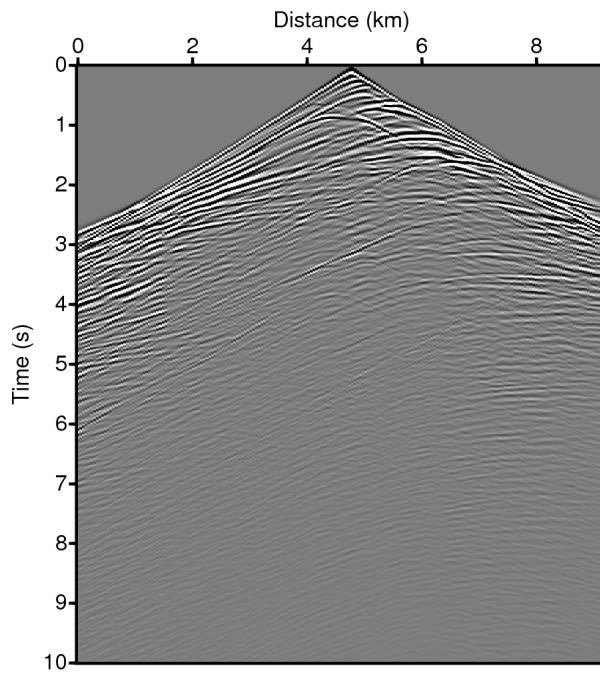
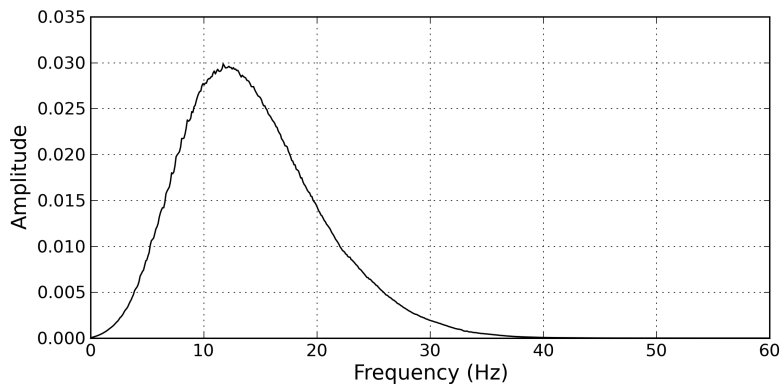


Figure 3.1 The Marmousi P-wave velocity model.



(a)



(b)

Figure 3.2 (a) A common-shot gather seismogram and (b) a frequency spectrum of the synthetic seismic data for the Marmousi model.

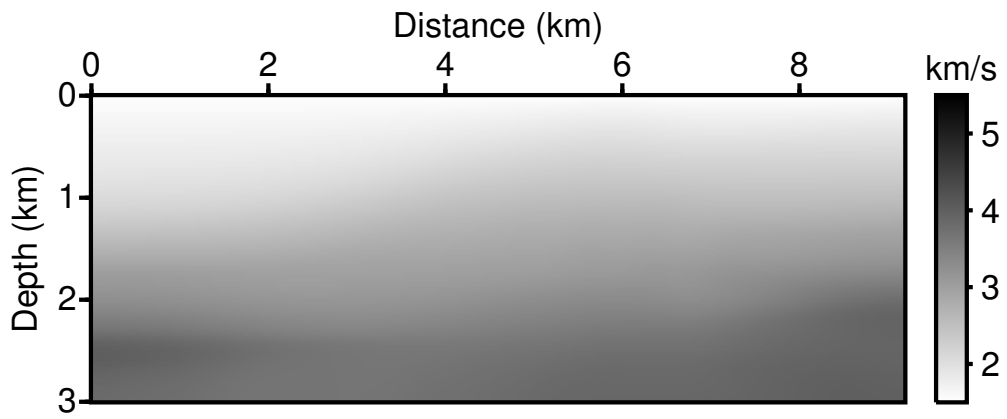
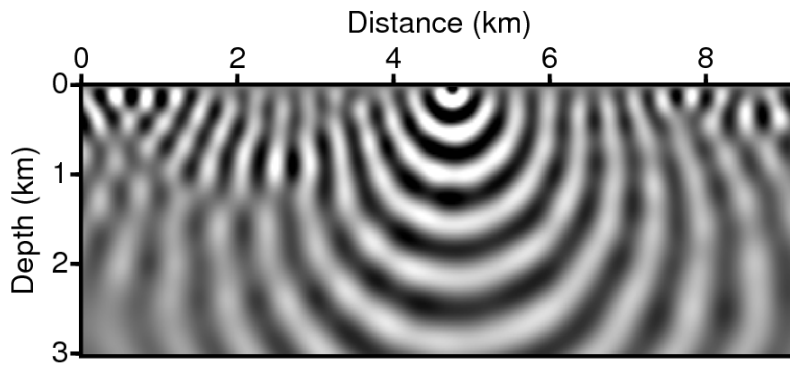
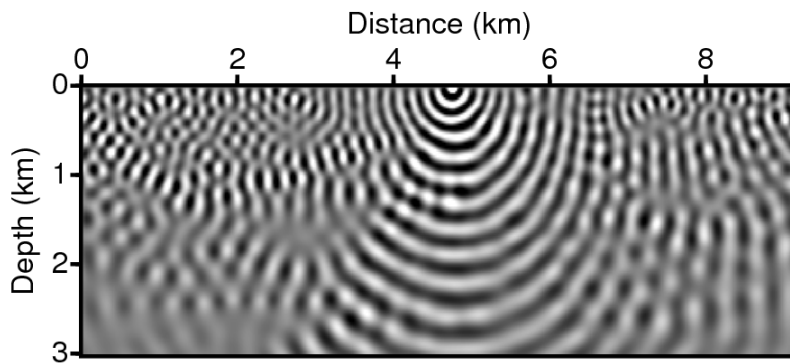


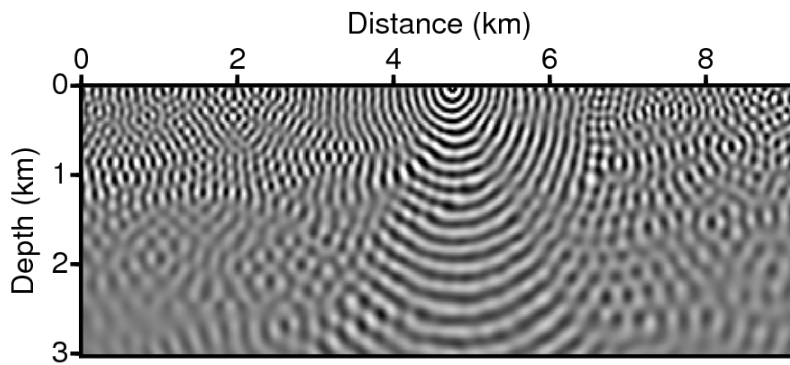
Figure 3.3 The initial velocity model for the waveform inversion of the synthetic Marmousi data set.



(a)

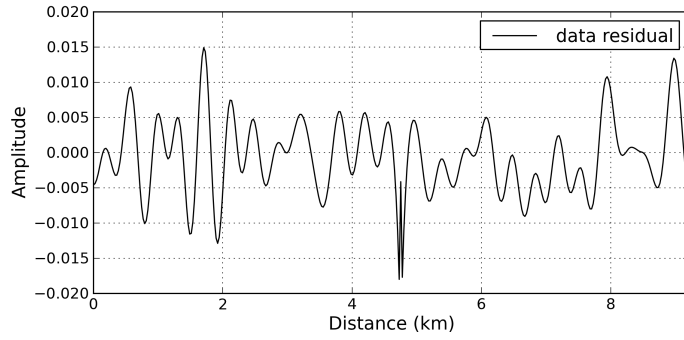


(b)

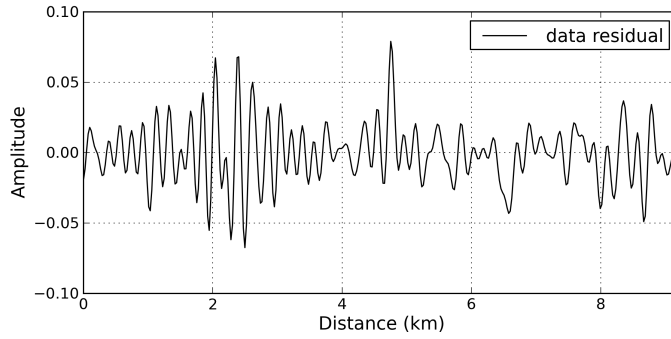


(c)

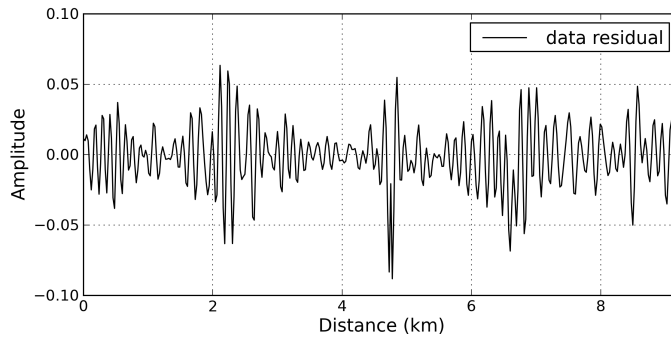
Figure 3.4 The frequency-domain reference wavefields propagated in the reference velocity model for the 100th shot (located at a distance of 4.8 km) with respect to a frequency of (a) 5 Hz, (b) 10 Hz and (c) 15 Hz.



(a)



(b)



(c)

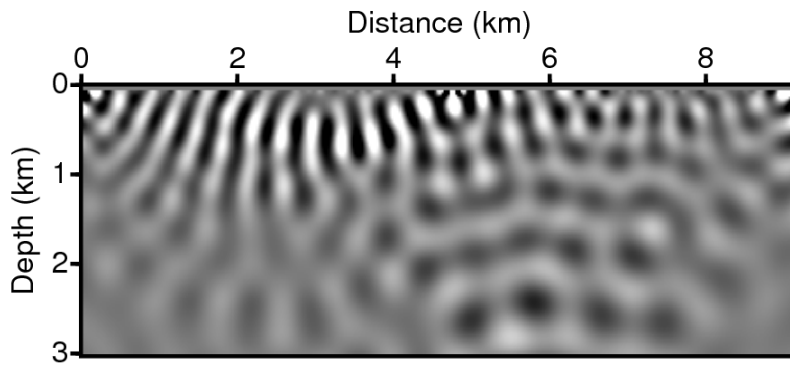
Figure 3.5 The frequency-domain data residuals for the 100th shot (located at a distance of 4.8 km) with respect to a frequency of (a) 5 Hz, (b) 10 Hz and (c) 15 Hz before performing the waveform inversion.

The virtual scattering source is formulated from the data residual with the numerical Green’s function. The generalized minimal residual (GMRES) solver (Frayssé et al., 2005) is employed to solve for the virtual scattering sources from the modified Lippmann-Schwinger equation in this study. Figure 3.6 presents the computed virtual scattering sources which are distributed throughout all of the grid points of the model.

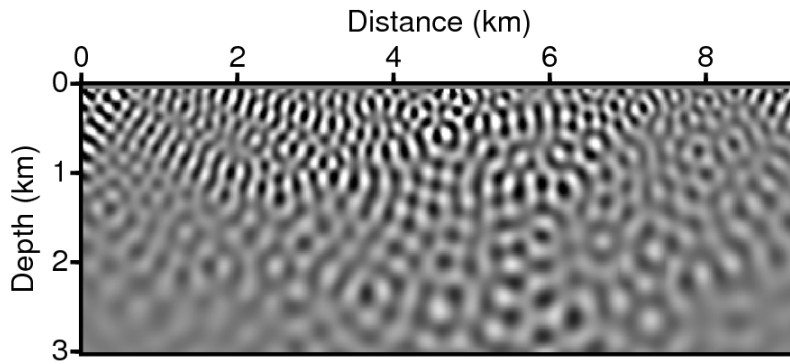
This inversion method requires fewer updates compared with FWI because it updates the velocity model once per frequency. However, the computation of the virtual scattering source requires relatively long computing time with the matrix solver and GMRES routines. For this inversion example, the computing time of the matrix decomposition with the multifrontal solver is approximately 0.32 s, and that of the system matrix solving with the decomposed matrix for a right-hand side is approximately 0.04 s. On the other hand, the computing time of the virtual scattering source is approximately 11.96 s because it requires the iterative system matrix to solve approximately 200 times for computational accuracy. If one can reduce the computing time of the virtual scattering source, then the inversion method can be more competitive with FWI in terms of the computational cost.

The scattered wavefields are reconstructed by propagating the virtual scattering source in the reference velocity model, as shown in Fig. 3.7. The sum of the reference and scattered wavefields is referred to as the total wavefield. Figure 3.8 shows the total wavefield as an approximation of the actual wavefield propagated in the medium of interest. Forward modeling of the estimated source in the true velocity model was also performed to obtain the actual wavefield, as shown in Fig. 3.9. The total wavefields are not exactly equal due to the single scattering

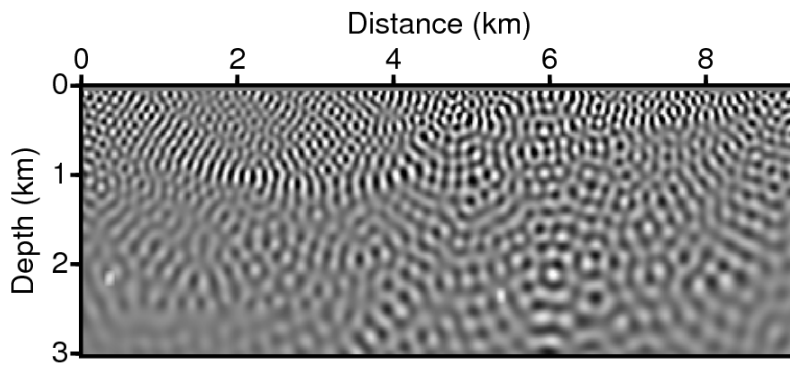
assumption but are analogous to the actual wavefields.



(a)

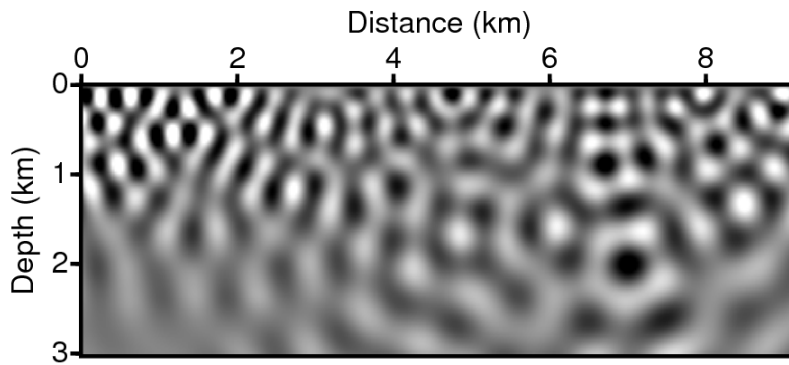


(b)

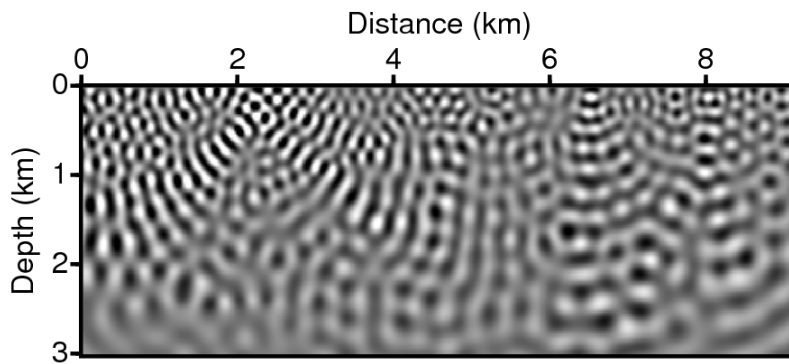


(c)

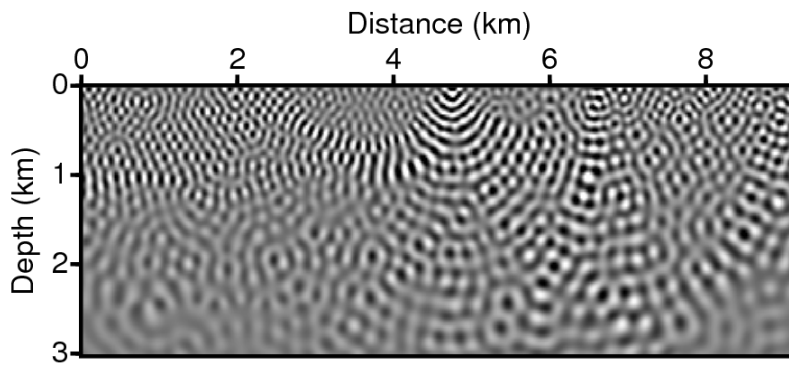
Figure 3.6 The frequency-domain virtual scattering sources for the 100th shot (located at a distance of 4.8 km) with respect to a frequency of (a) 5 Hz, (b) 10 Hz and (c) 15 Hz.



(a)

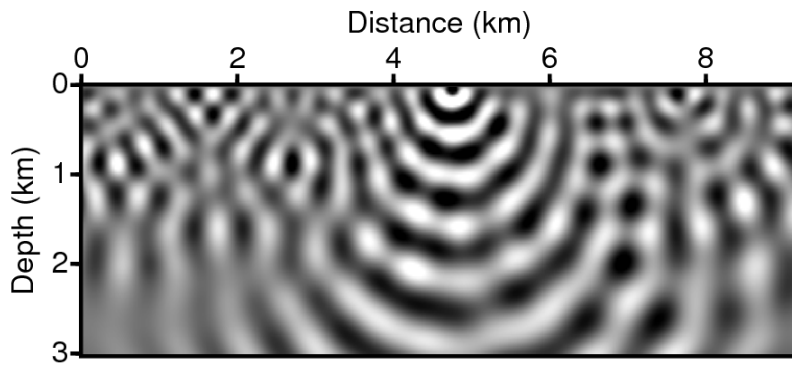


(b)

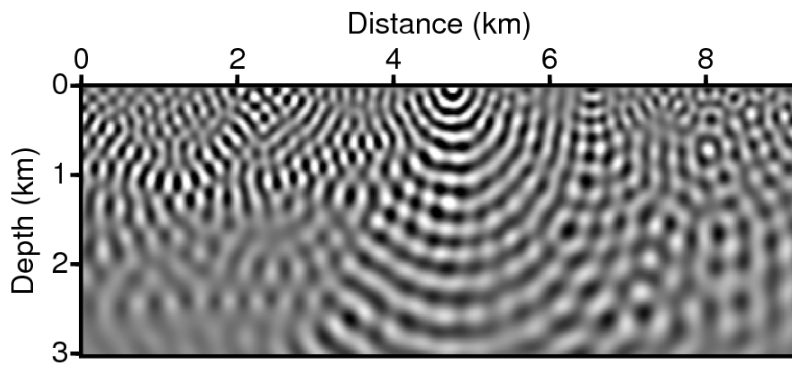


(c)

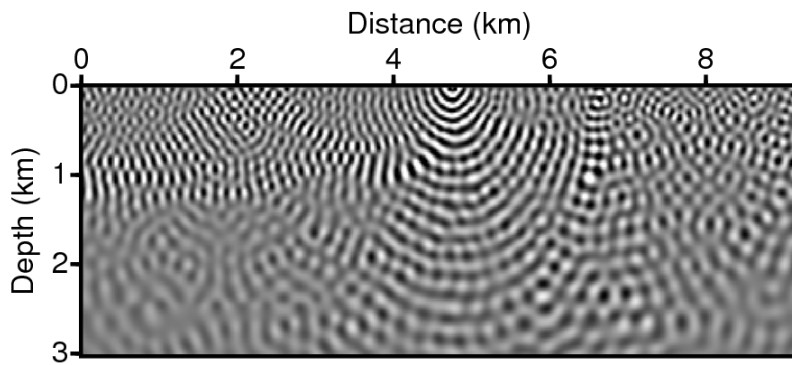
Figure 3.7 The frequency-domain scattered wavefields reconstructed for the 100th shot (located at a distance of 4.8 km) with respect to a frequency of (a) 5 Hz, (b) 10 Hz and (c) 15 Hz.



(a)

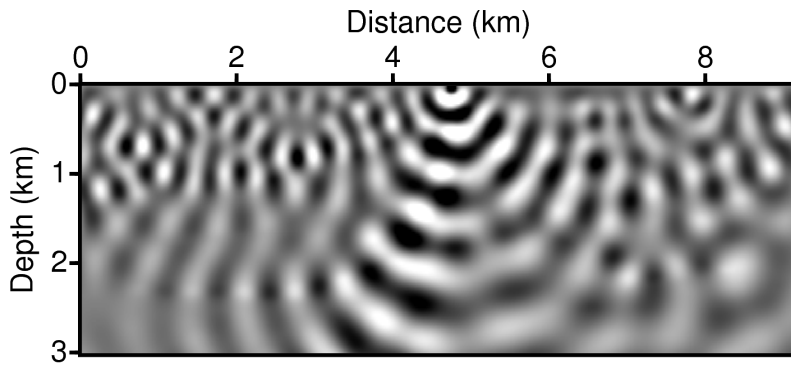


(b)

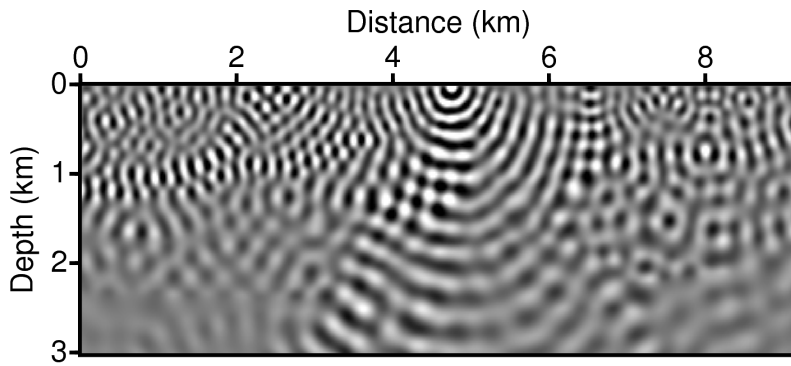


(c)

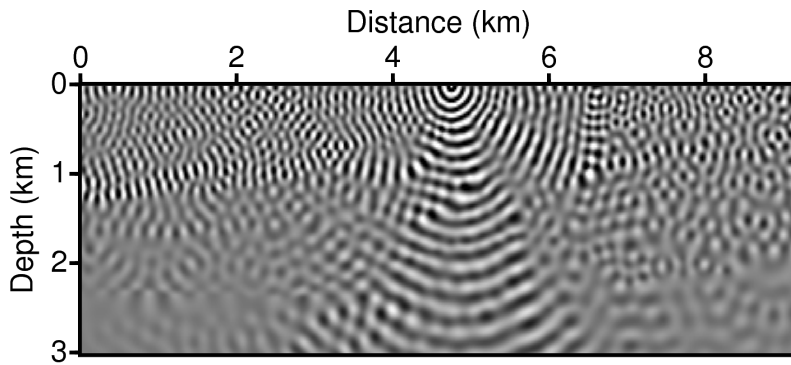
Figure 3.8 The frequency-domain total wavefields reconstructed for the 100th shot (located at a distance of 4.8 km) with respect to a frequency of (a) 5 Hz, (b) 10 Hz and (c) 15 Hz.



(a)

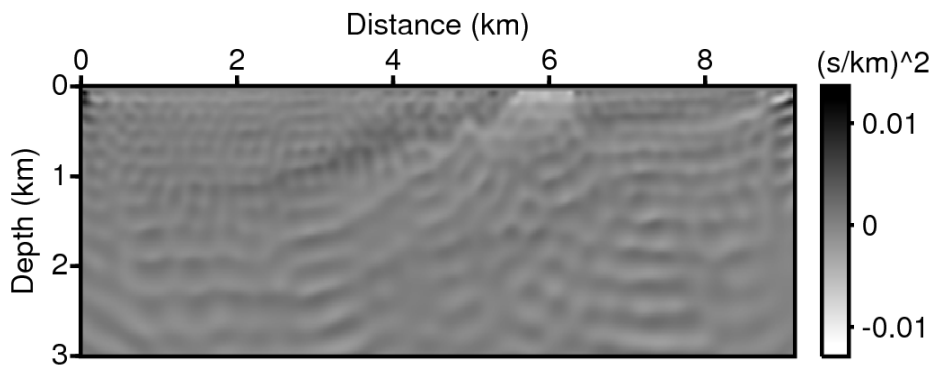


(b)

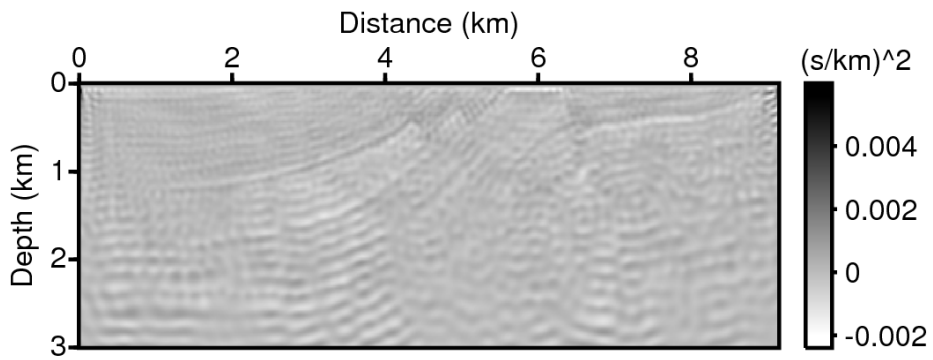


(c)

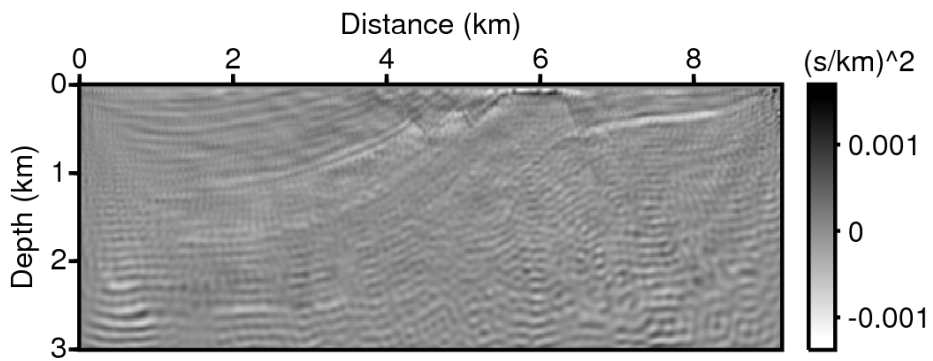
Figure 3.9 The frequency-domain actual wavefields propagated in the true Marmousi velocity model for the 100th shot (located at a distance of 4.8 km) with respect to a frequency of (a) 5 Hz, (b) 10 Hz and (c) 15 Hz.



(a)



(b)



(c)

Figure 3.10 The slowness perturbations computed with respect to a frequency of (a) 5 Hz, (b) 10 Hz and (c) 15 Hz.

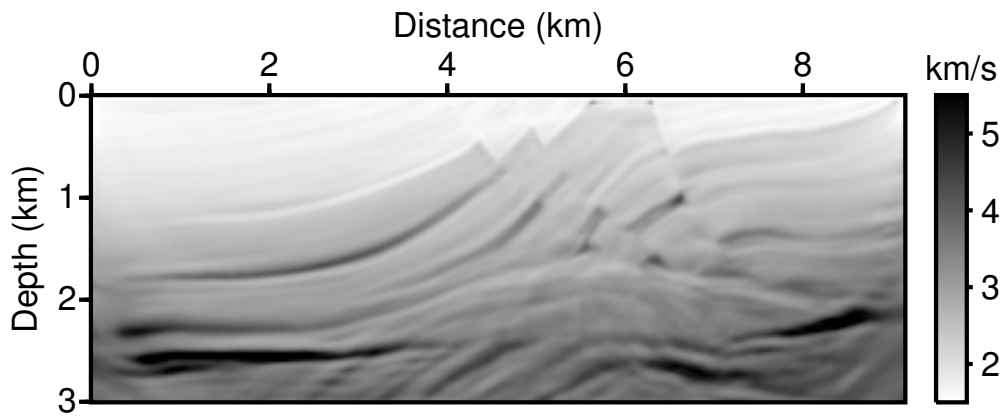
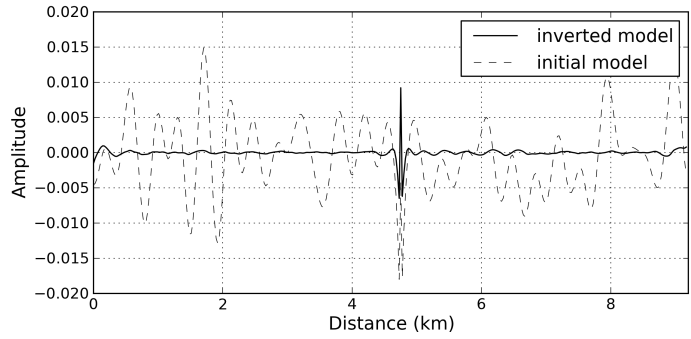


Figure 3.11 The velocity model updated by the waveform inversion of the synthetic Marmousi data set.

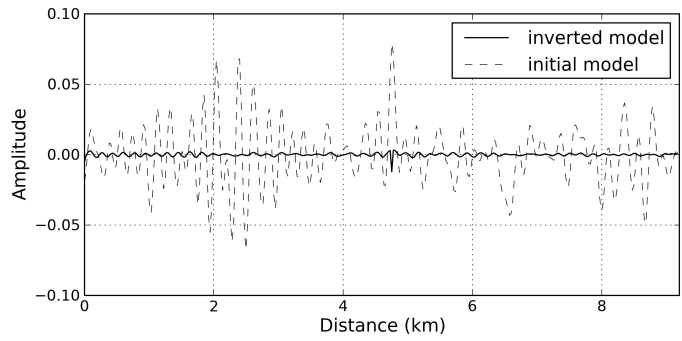
Figure 3.10 presents the sloth perturbations obtained from the virtual scattering sources and the total wavefields for each of the frequency components. Lastly, the initial velocity model is updated by adding the sloth perturbations with Eq. (2.61). The processes – from the source signature estimation to the model update – are performed for a single frequency. The velocity model is updated before moving on to the next frequency, and the frequencies are considered sequentially from low to high. The updated velocity model is analogous to the true velocity model with stratified layers and structures and also displays an anticline structure in the bottom-center of the true model as shown in Fig. 3.11.

Fig. 3.12 presents a comparison of the data residuals for the initial and inverted velocity models. The data residuals for the inverted velocity model are significantly smaller than those for the initial velocity model. Thus, the waveform inversion reconstructed the scattered wavefield to closely resemble the actual wavefield at the receiver positions.

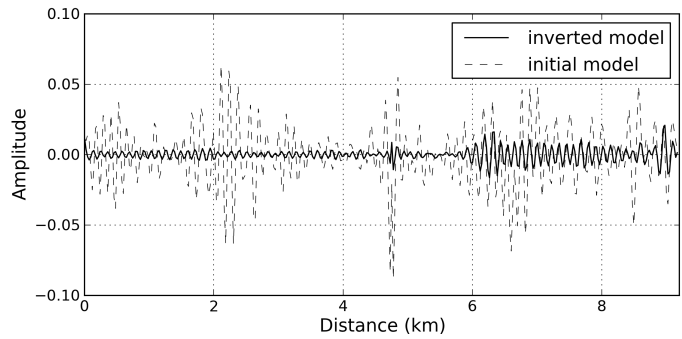
To demonstrate the reliability of the waveform inversion, synthetic seismograms for the initial, inverted and true velocity models are compared in Figs. 3.13, 3.14 and 3.15. For the synthetic seismograms of the inverted velocity model, the time-domain seismograms are synthesized by the inverse Fourier transform of the frequency-domain total wavefields reconstructed during the waveform inversion. The recovered synthetic seismograms are not exactly equivalent to the propagations of the estimated source wavelet in the inverted velocity model. However, the recovered synthetic seismograms match the corresponding shot-gather seismograms of the synthetic field data and can be considered as criteria for the comparison of the inversion result.



(a)



(b)



(c)

Figure 3.12 The frequency-domain data residuals for the 100th shot (located at a distance of 4.8 km) with respect to the frequency of (a) 5 Hz, (b) 10 Hz and (c) 15 Hz. The data residual computed with forward-modeled data for the initial velocity model (dashed line) and the total wavefield (solid line) after performing the waveform inversion.

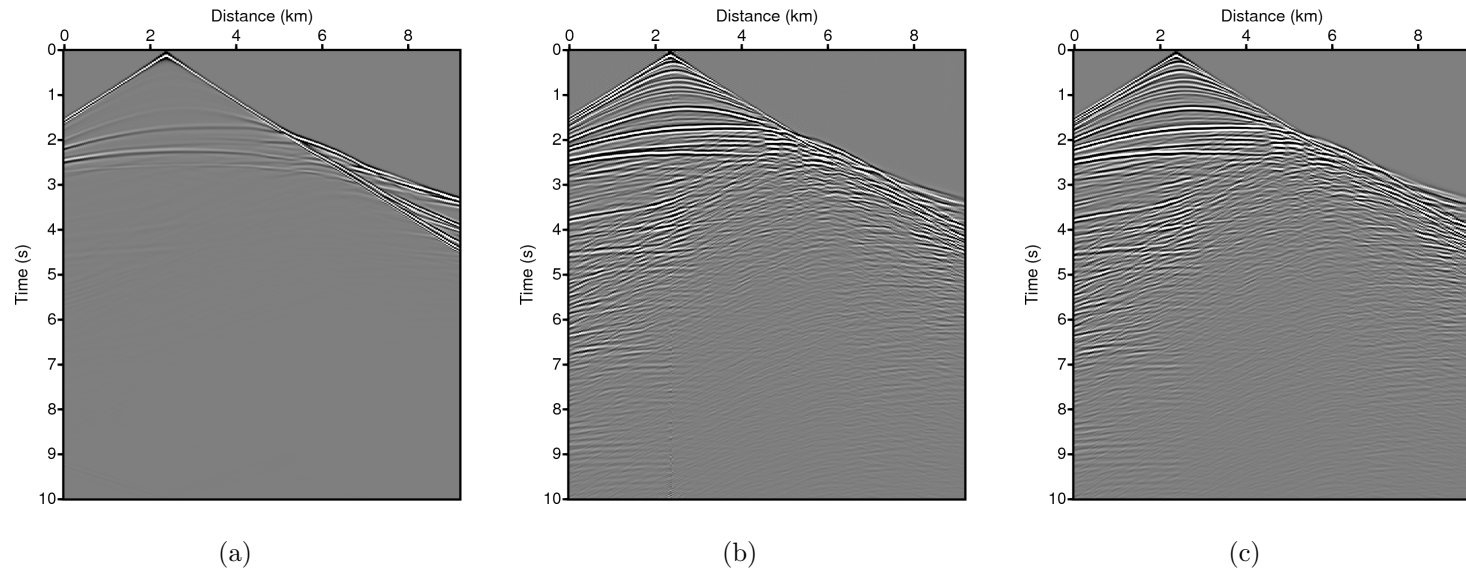


Figure 3.13 The common-shot gather seismograms for the 50th shot (located at a distance of 2.4 km): seismograms synthesized for the (a) initial, (b) inverted and (c) true velocity models.

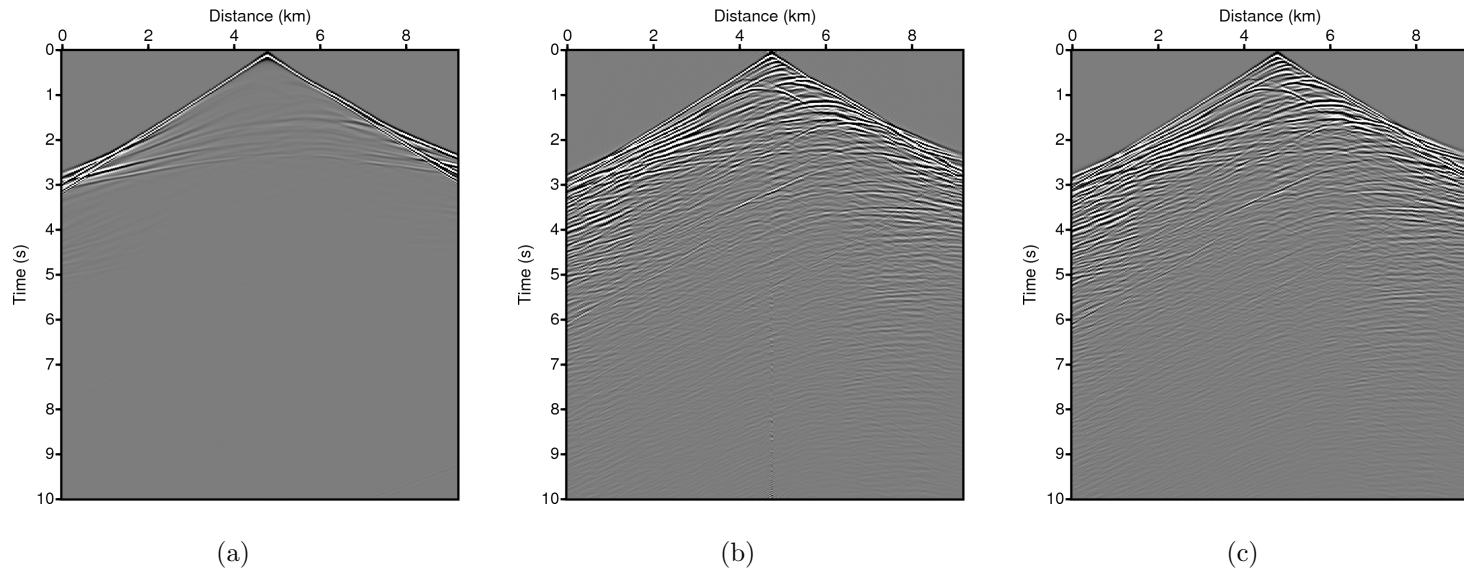


Figure 3.14 The common-shot gather seismograms for the 100th shot (located at a distance of 4.8 km): seismograms synthesized for the (a) initial, (b) inverted and (c) true velocity models.

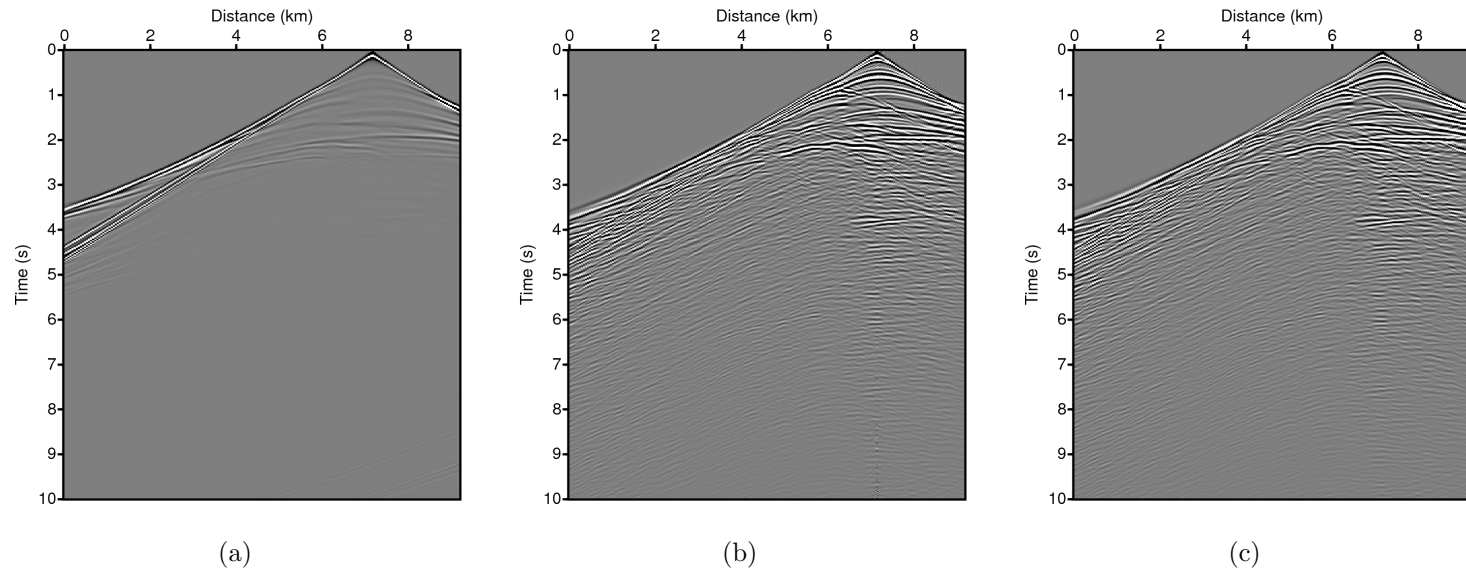


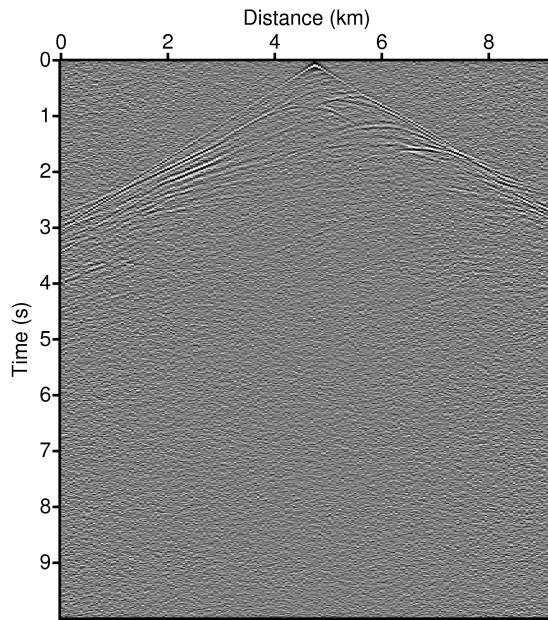
Figure 3.15 The common-shot gather seismograms for the 150th shot (located at a distance of 7.2 km): seismograms synthesized for the (a) initial, (b) inverted and (c) true velocity models.

Following the waveform inversion example of the Marmousi data set, I examine the effective factors for LSWI solutions. Gradient-based FWI methods do not prevent convergence of the misfit function toward local minima due to the limited accuracy of the given initial model, the lack of low frequencies, the presence of noise and the approximate modeling of the wave-physics complexity (Virieux and Operto, 2009). On the other hand, LSWI is a direct waveform inversion method that takes advantage of the scattering and perturbation theories to update velocity models without a local optimization approach. However, LSWI assumes single scattering to reconstruct total wavefields and employs forward modeling of the wave equation, which FWI also exploits. Therefore, LSWI solutions have the potential to be influenced by the presence of noise, the lack of low frequencies, the accuracy of the initial velocity model and the forward modeling as an approximation of wave physics.

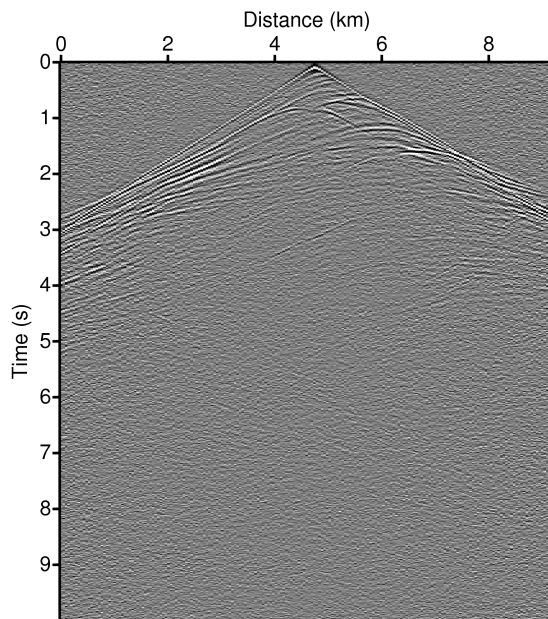
### 3.1.1 Sensitivity to the presence of noise in data

LSWI employs frequency-domain forward modeling of wave physics, which does not include noise effect. Accordingly, solutions of the waveform inversion method can be influenced by the presence of noise in the real seismic field data. In this section, I examine the sensitivity of the waveform inversion solution to the level of noise in the data.

I performed LSWI for noise-contaminated data of the Marmousi data set. Gaussian random noise is added to the noise-free Marmousi data set (depicted in Fig. 3.2a) with signal-to-noise (S/N) ratios (i.e., maximum amplitude of signal over maximum amplitude of random noise) of 12.75 and 25.50. The noise-contaminated data with an S/N ratio of 12.75 cannot clearly describe the important reflection or refraction signals due to the strong random noise, as shown in Fig. 3.16. LSWI is performed under the same conditions as those for the noise-free Marmousi data set in Section 3.1, except for the seismic data used as the input. The inverted velocity models are depicted in Fig. 3.17. Because the meaningful signals in the data are contaminated by the random noise, inverted velocity models of the noise-contaminated data are affected by the noise and display relatively poor images of subsurface structures compared with the model of noise-free data. The inverted velocity model with a S/N ratio 25.50 describes the stratified and anticline structures better than the model with a S/N ratio 12.75 as shown in Figs. 3.17a and 3.17b. The synthetic seismograms are recovered and compared with the corresponding seismograms of input seismic data set. Figure 3.18, 3.19, 3.20 and 3.21 present seismograms of the noise-contaminated input data and the data recovered by LSWI. The noises in the input data are not separated from the signals during the inversion procedure and therefore are recovered together.

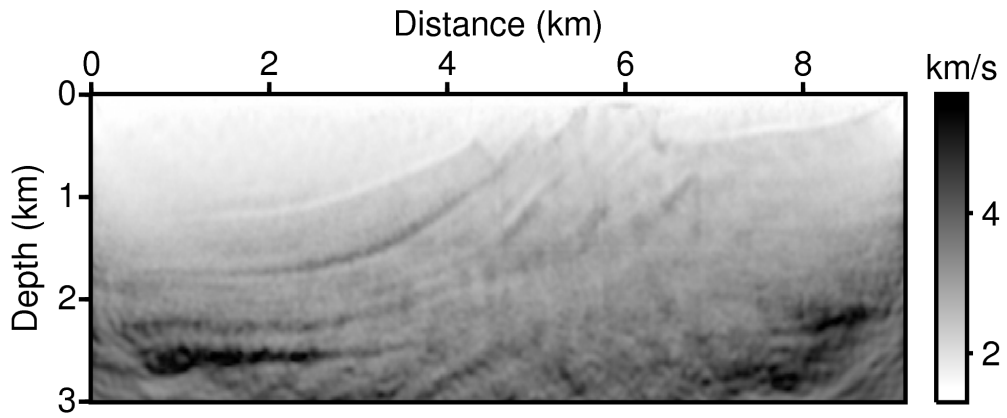


(a)

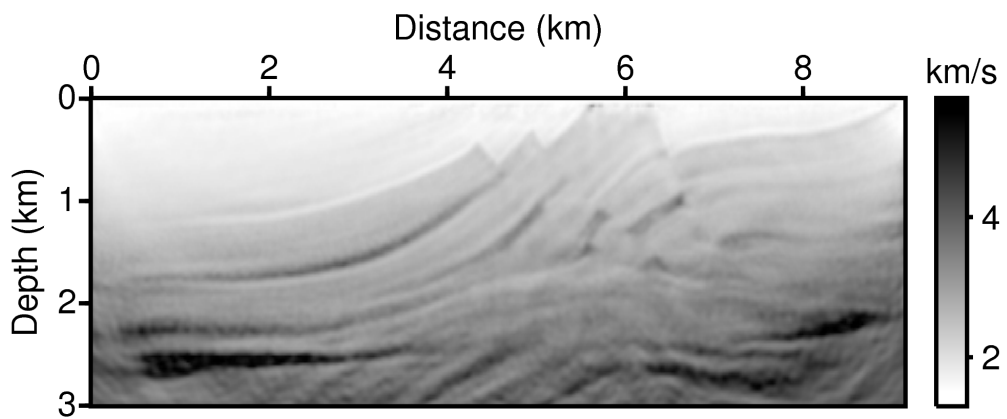


(b)

Figure 3.16 The common-shot gather seismograms of the noise-contaminated Marmousi data set with Gaussian random noise: S/N ratio of (a) 12.75 and (b) 25.50.



(a)



(b)

Figure 3.17 The inverted velocity models for the noise-contaminated Marmousi data set with Gaussian random noise: S/N ratio of (a) 12.75 and (b) 25.50.

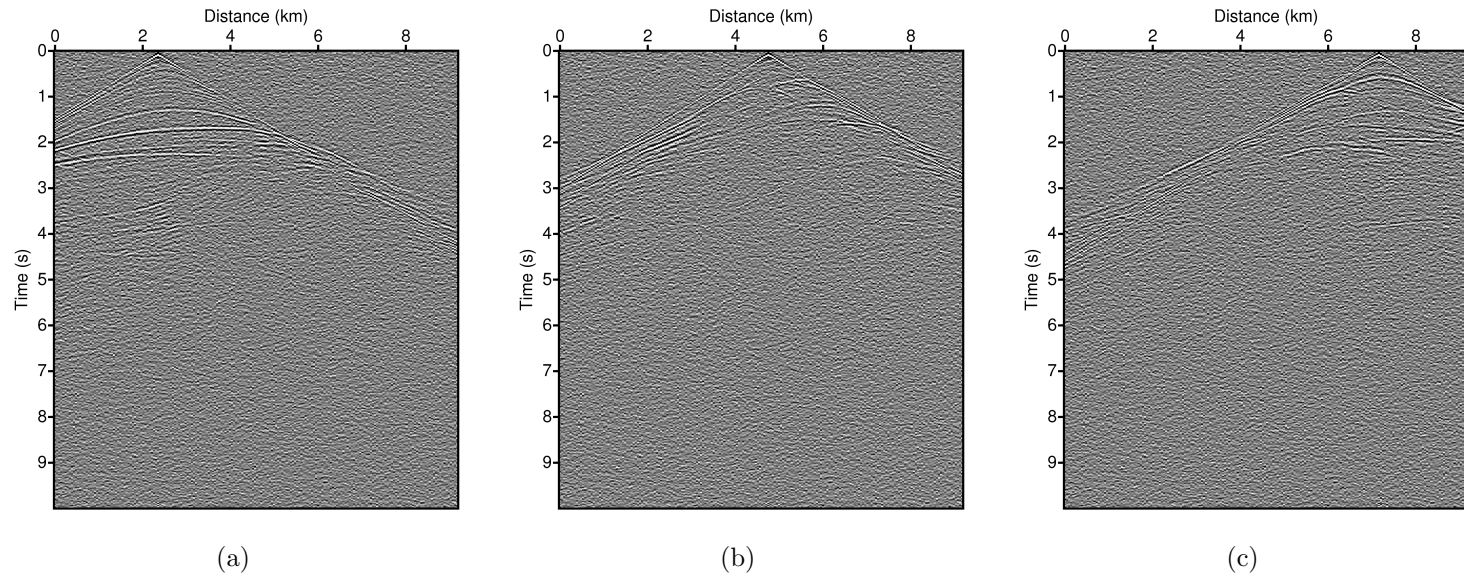


Figure 3.18 The common-shot gather seismograms of noise-contaminated Marmousi data set with Gaussian random noise: S/N ratio of 12.75 for the (a) 50th, (b) 100th and (c) 150th shot (source located at 2.4 km , 4.8 km and 7.2 km).

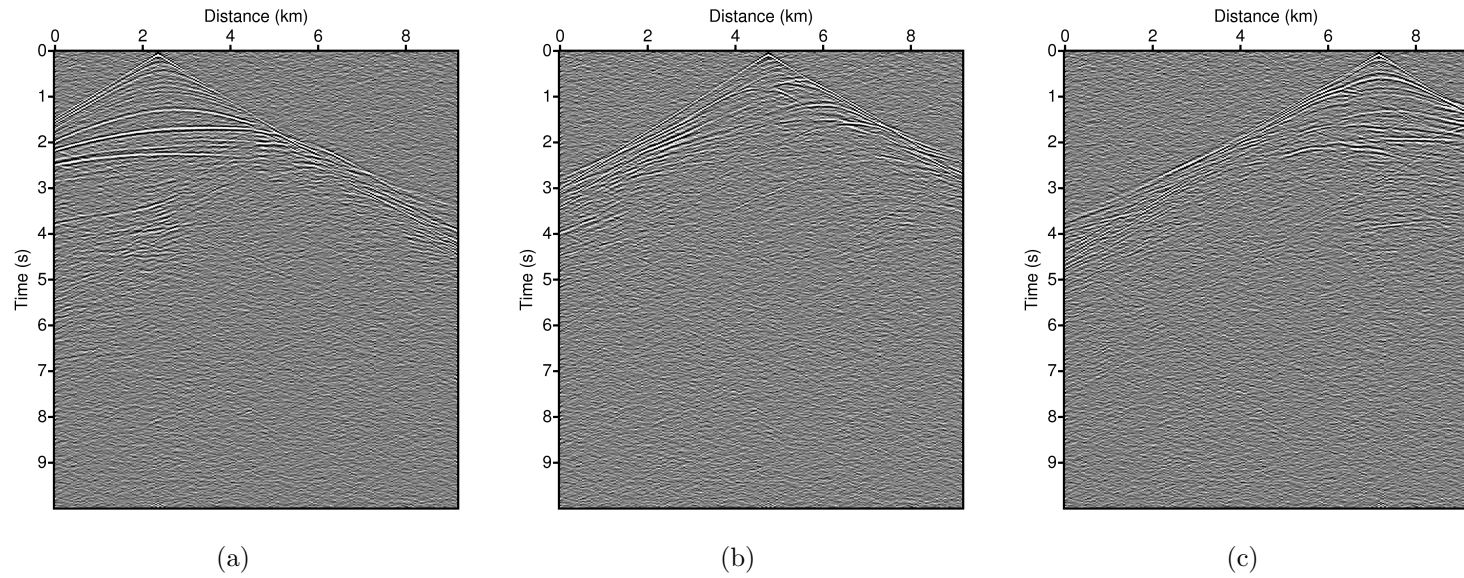


Figure 3.19 The synthetic common-shot gather seismograms recovered by the waveform inversion of noise-contaminated Marmousi data set with Gaussian random noise:  $S/N$  ratio of 12.75 for the (a) 50th, (b) 100th and (c) 150th shot (source located at 2.4 km , 4.8 km and 7.2 km).

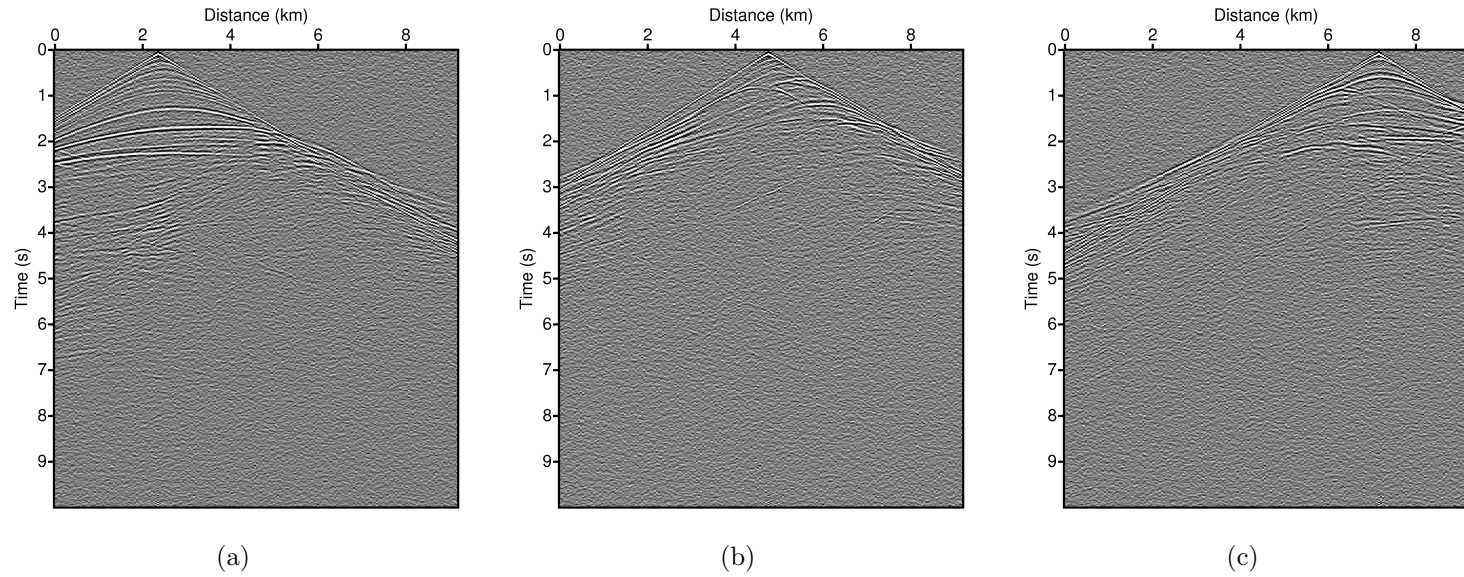


Figure 3.20 The common-shot gather seismograms of noise-contaminated Marmousi data set with Gaussian random noise: S/N of ratio 25.50 for the (a) 50th, (b) 100th and (c) 150th shot (source located at 2.4 km , 4.8 km and 7.2 km).

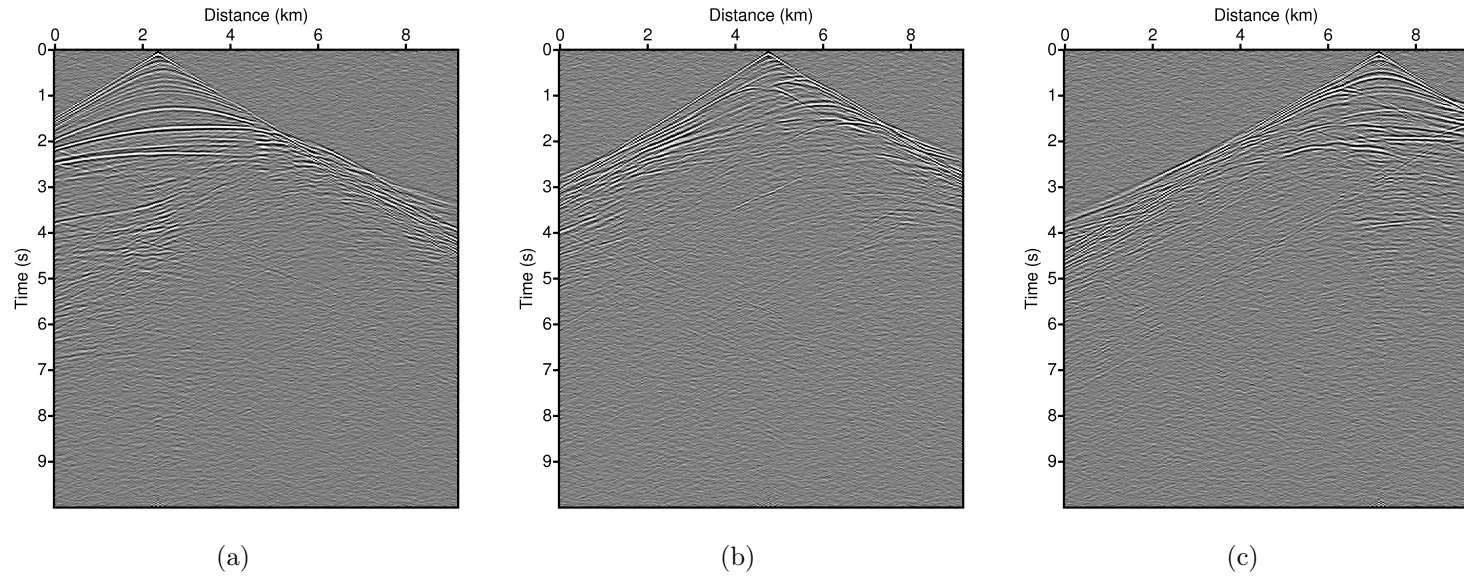


Figure 3.21 The synthetic common-shot gather seismograms recovered by the waveform inversion of noise-contaminated Marmousi data set with Gaussian random noise:  $S/N$  ratio of 25.50 for the (a) 50th, (b) 100th and (c) 150th shot (source located at 2.4 km , 4.8 km and 7.2 km).

The inversion examples with noise-contaminated data indicate that the waveform inversion results depend on the quality of the input data such as the amplitudes of the signals. Given that the LSWI takes advantage of the data residuals to generate the virtual scattering sources and the scattered wavefields, the data quality is important for the inversion results. If the input seismic data are contaminated by noise, the virtual scattering sources are formulated to reconstruct the scattered wavefields including noises in the input data. However, if the input data set with random noise has an S/N ratio high enough to preserve the meaningful signals, then the waveform inversion method can produce trustworthy solutions. The detailed cause and the antidote to noise will be discussed in Section 4.1.

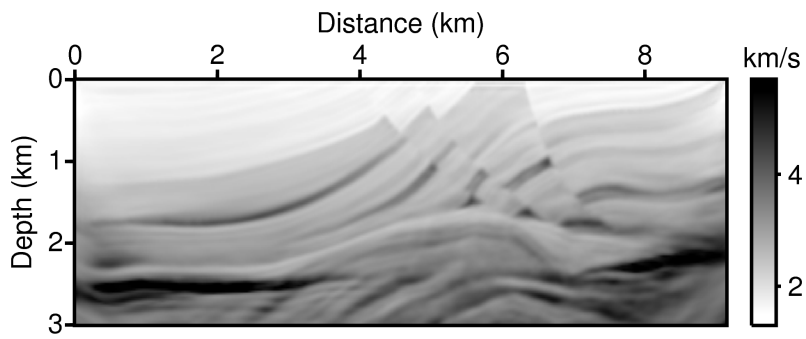
### 3.1.2 Sensitivity to the lack of low frequencies in data

Sirgue (2006) reported the benefits of having low frequencies and large offsets present in the data for the frequency-domain FWI. The waveform inversion in this study employs forward modeling of the frequency-domain wave equation and solves for the medium perturbation in the frequency domain just as the frequency-domain FWI does. Therefore, solutions of the waveform inversion can be affected by the presence of low-frequency components in the real field seismic data. In this section, I examine the sensitivity of the waveform inversion solution to the lack of low frequencies in data.

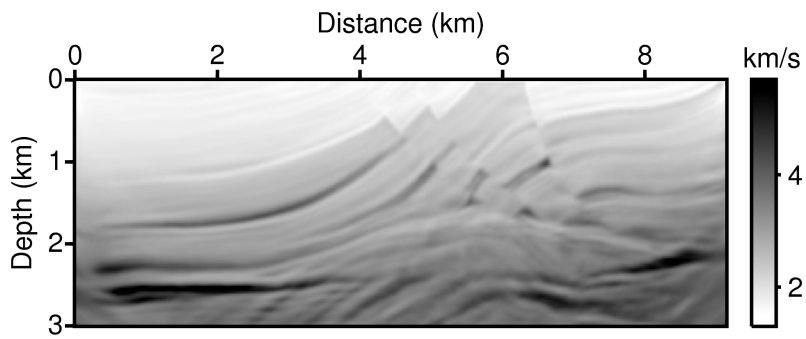
I performed LSWI using various frequency ranges for the same Marmousi data set to demonstrate the importance of the use of low-frequency components. In this context, LSWI is performed under the same conditions as those for the Marmousi data set in Section 3.1, except for the usage of frequency components. Frequency components of 2 Hz, 4 Hz, and 6 Hz to 20 Hz were used with a 0.1 Hz frequency interval, and the numbers of frequencies were 181, 161, and 141, respectively. The inverted velocity model with frequency components starting from 2 Hz reveals a relatively clear image of the anticline structures at the middle-center and bottom-center compared with the inverted models starting from 4 Hz and 6 Hz as shown in Fig. 3.22. However, the inverted velocity model with frequency components starting from 6 Hz barely describes the anticline structures of the model.

Waveform inversion methods, such as gradient-based FWI, are generally affected by the usage of temporal frequencies. The significant point is that because the low frequencies have a more linear relation with the low-wavenumber components of the model, the chance of locating global minima will be diminished if the low-frequency information is not used (Sirgue and Pratt, 2004). Therefore,

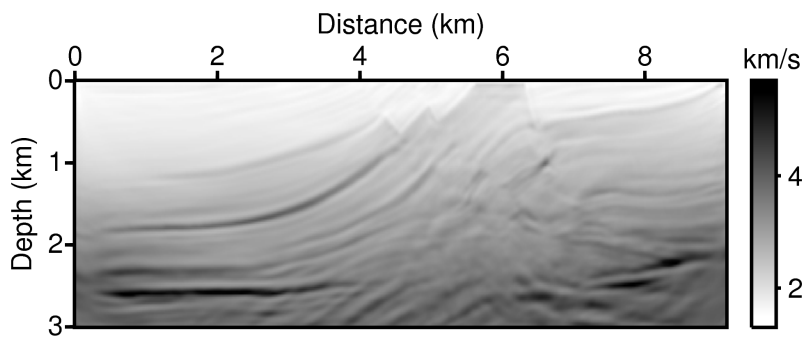
the frequency-domain waveform inversion should start with low-frequency components to provide reliable inverted velocity models if the inversion is performed in a sequential order of frequency. The detailed cause of the benefits that result from the low-frequency components will be discussed in Section 4.2.



(a)



(b)



(c)

Figure 3.22 The inverted velocity models with frequency components starting from (a) 2 Hz, (b) 4 Hz and (c) 6 Hz.

### 3.1.3 Sensitivity to the accuracy of the initial models

LSWI requires the initial velocity model because the inversion is a type of inverse scattering problem. The inversion method employs the initial model as a reference velocity model for the starting frequency to obtain the reference wavefield. Accordingly, solutions of the waveform inversion can be affected by the accuracy of the initial model. In this section, I examine the sensitivity of the waveform inversion solution to the accuracy of the initial velocity model.

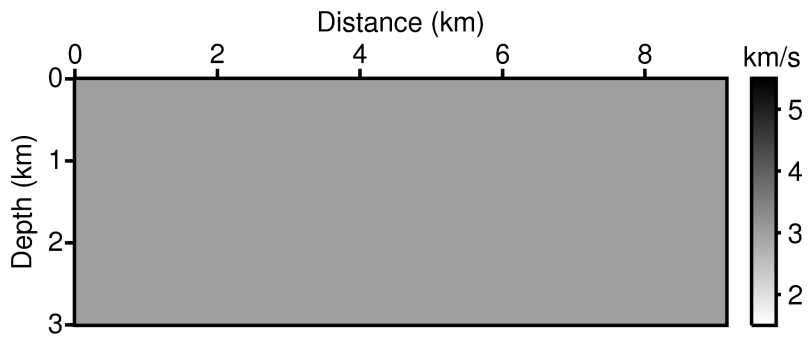
I performed the waveform inversion starting from the various initial velocity models. The waveform inversion is performed under the same conditions as those for the Marmousi data set in Section 3.1, except for the initial velocity model.

For the comparison, the following three initial velocity models are used: the 3 km/s homogeneous velocity model, the 1.5 - 4.5 km/s linearly increasing velocity model and the smoothed velocity model (Fig. 3.23). In theory, LSWI should yield an inverted velocity model as a unique solution of the waveform inversion. However, the inverted velocity models differ from each other as shown in Fig. 3.24. Thus, the waveform inversion cannot accurately delineate the true velocity model if the initial velocity model is not analogous to the true model. In other words, a waveform inversion with an initial velocity model sufficiently similar to the true model can exactly describe the true velocity model.

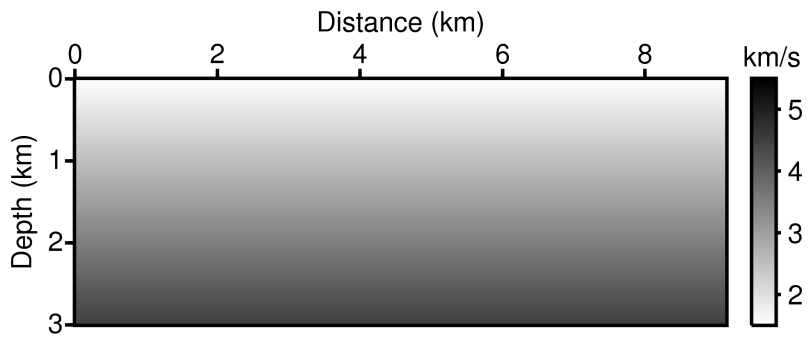
Although the different initial models yield different inverted models, the synthetic seismograms recovered during the inversion procedure are very analogous to each other, as shown in Figs. 3.25 and 3.26. The waveform inversions initiated by different initial models yield different inverted models, though they all recover synthetic seismograms similar to the recorded seismic data. The inversion method reconstructs the scattered wavefields in the medium and, notably, is tempted to

fit the scattered wavefields at the receiver positions (i.e., data residuals). On the other hand, the sloth perturbations used to update the reference model are estimated from the virtual scattering sources and the total wavefields reconstructed at the whole position of the medium. As a result, the waveform inversion method can derive various solutions for a given data set; however, all of the recovered seismograms are similar to the recorded seismic data.

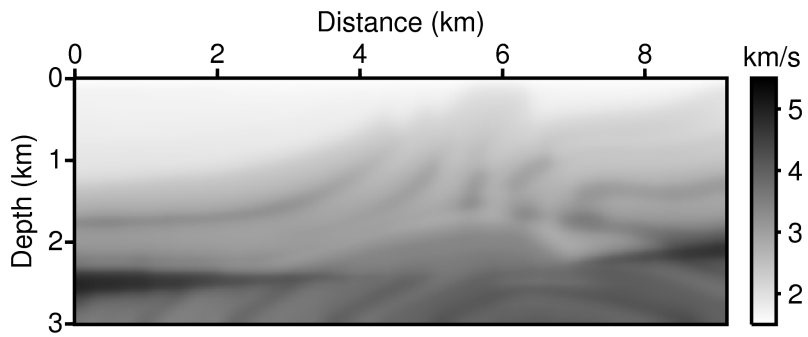
I also performed a Kirchhoff migration (Yilmaz, 2001; Forel et al., 2005) with the Marmousi data set using the initial and inverted velocity models as the background velocity models for the migration. Figures 3.27 and 3.28 depict migrated images for the initial and inverted velocity models, respectively. The migration images for the inverted models are enhanced compared with the initial models, especially for the relatively poor initial models. Thus, the proposed inversion can provide trustworthy background velocity models for good migration images even if the initial models have poor accuracy. A detailed discussion regarding the sensitivity to the accuracy of the initial models will be presented in Section 4.3.



(a)

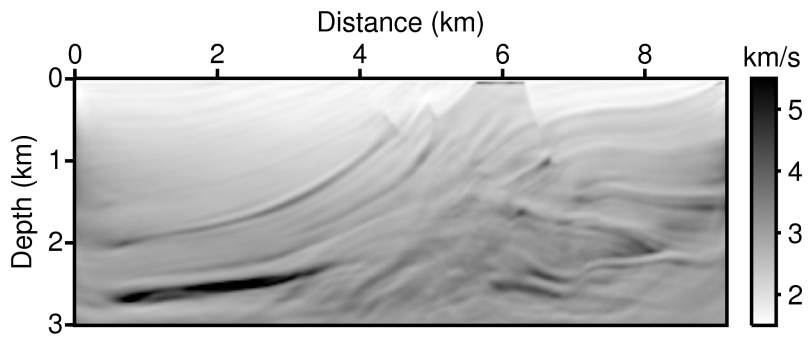


(b)

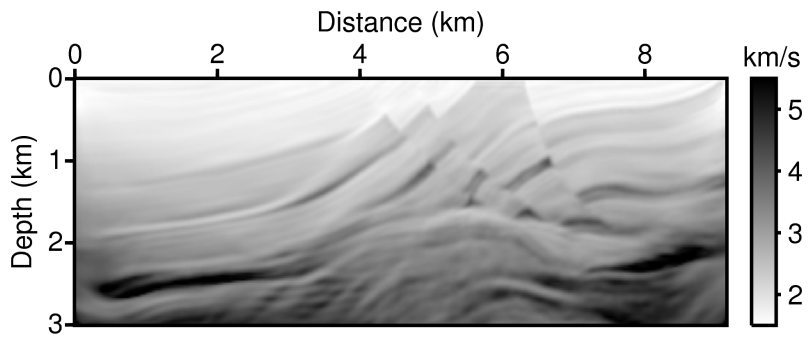


(c)

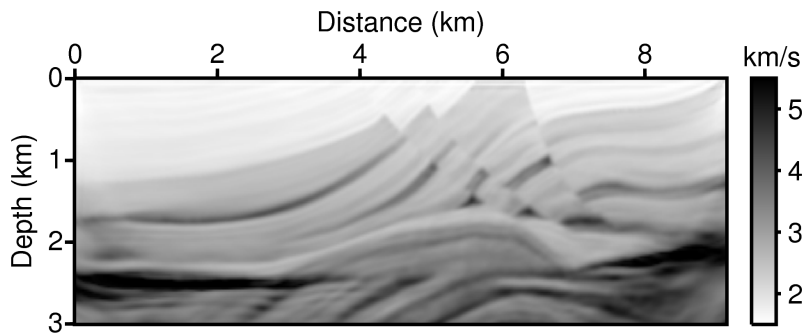
Figure 3.23 The initial velocity models for the waveform inversion: (a) homogeneous velocity model of 3 km/s, (b) linearly increasing velocity model ranging from 1.5 to 4.5 km/s and (c) smoothed velocity model.



(a)



(b)



(c)

Figure 3.24 The inverted velocity models started with the initial velocity models: (a) homogeneous velocity model of 3 km/s, (b) linearly increasing velocity model ranging from 1.5 to 4.5 km/s and (c) smoothed velocity model.

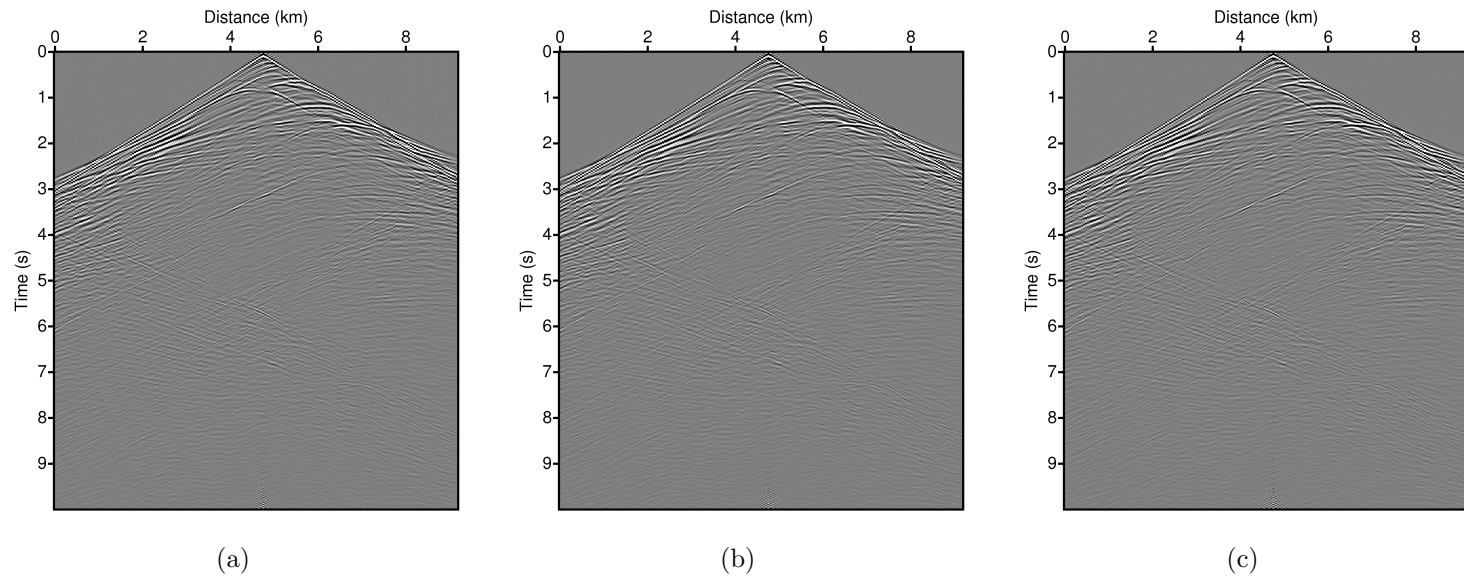
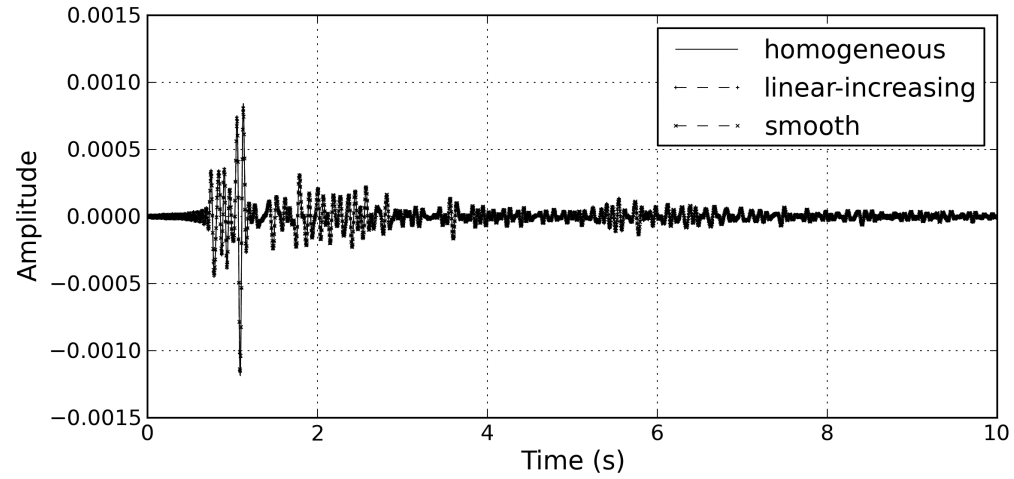
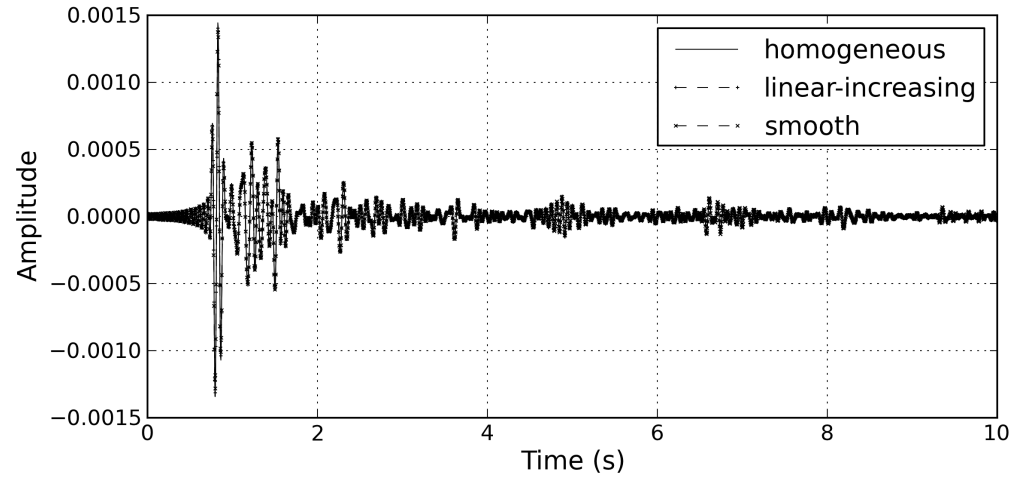


Figure 3.25 The common-shot gather seismograms of 100th shot: synthetic seismograms for the inverted velocity models started with the (a) homogeneous, (b) linearly increasing and (c) smoothed velocity models.



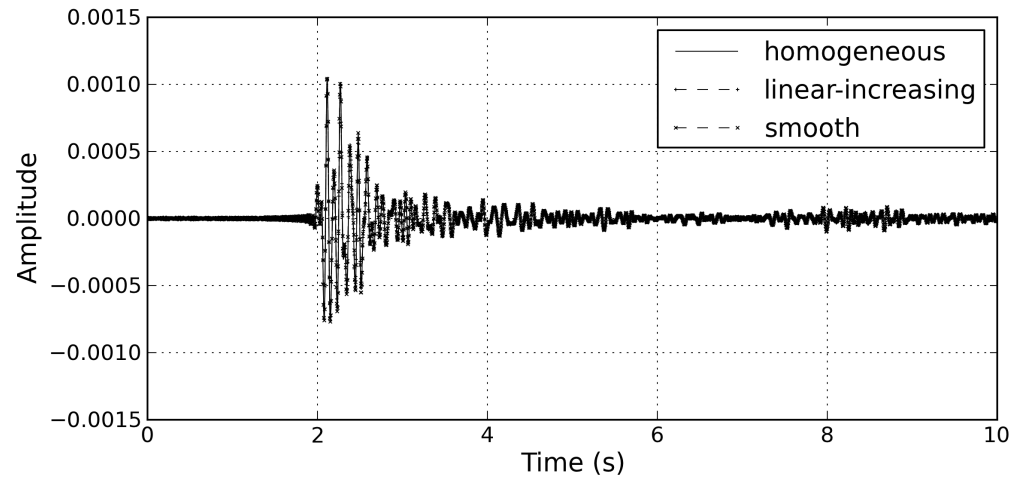
(a)

Figure 3.26 The comparison of traces from the common-shot gather seismograms of 100th shot for the inverted velocity models started with the homogeneous (solid), linearly increasing (dashed with '+' marker) and smoothed (dashed with  $\times$  marker) velocity models. The receivers are located at the distance of (a) 3.6 km, (b) 6.0 km and (c) 8.4 km.



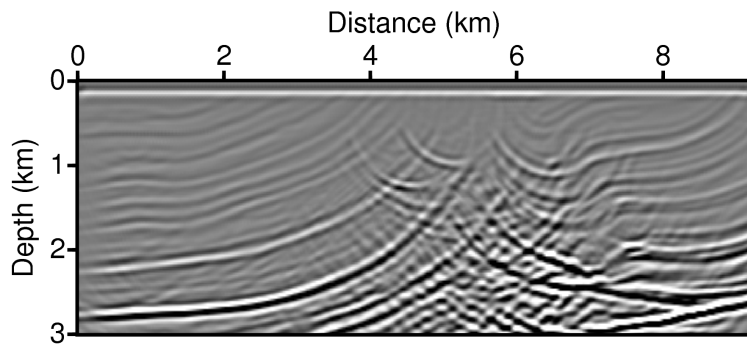
(b)

Figure 3.26 (continued) The comparison of traces from the common-shot gather seismograms of 100th shot for the inverted velocity models started with the homogeneous (solid), linearly increasing (dashed with '+' marker) and smoothed (dashed with  $\times$  marker) velocity models. The receivers are located at the distance of (a) 3.6 km, (b) 6.0 km and (c) 8.4 km.

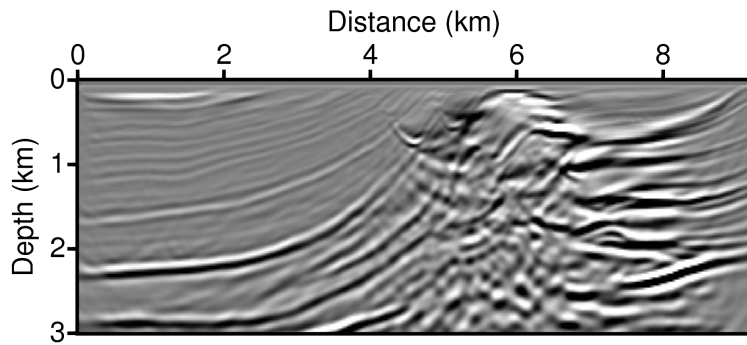


(c)

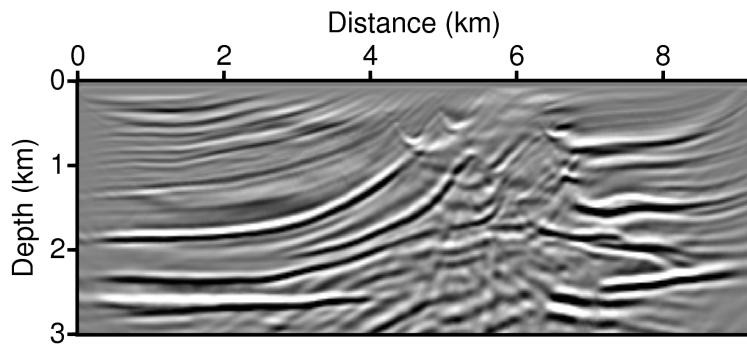
Figure 3.26 (continued) The comparison of traces from the common-shot gather seismograms of 100th shot for the inverted velocity models started with the homogeneous (solid), linearly increasing (dashed with '+' marker) and smoothed (dashed with  $\times$  marker) velocity models. The receivers are located at the distance of (a) 3.6 km, (b) 6.0 km and (c) 8.4 km.



(a)

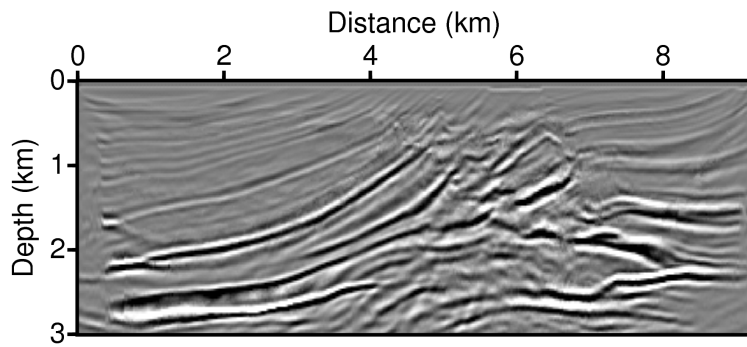


(b)

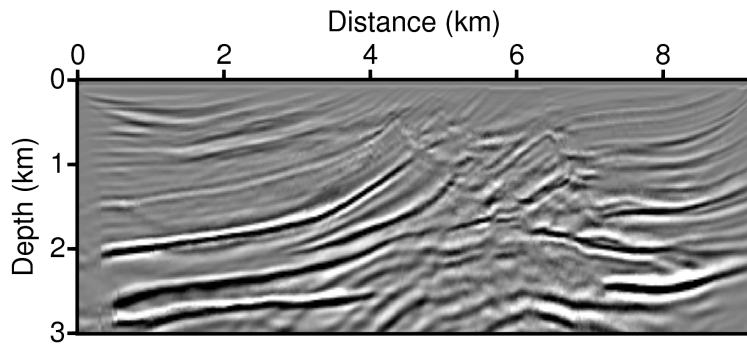


(c)

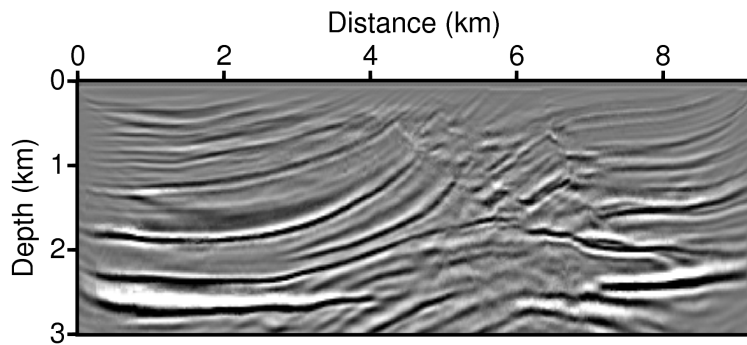
Figure 3.27 The migration images for the initial velocity models: (a) homogeneous velocity model of 3 km/s, (b) linear-increasing velocity model from 1.5 to 4.5 km/s and (c) smoothed velocity model.



(a)



(b)



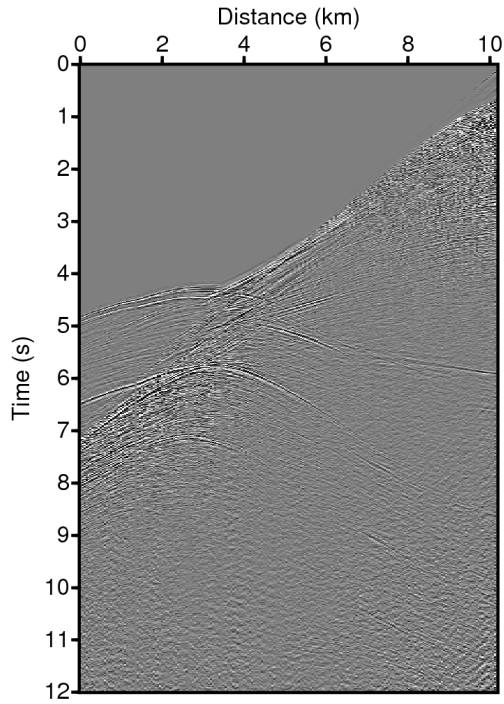
(c)

Figure 3.28 The migration images for the inverted velocity models updated from the initial velocity models: (a) homogeneous velocity model of 3 km/s, (b) linearly increasing velocity model from 1.5 to 4.5 km/s and (c) smoothed velocity model.

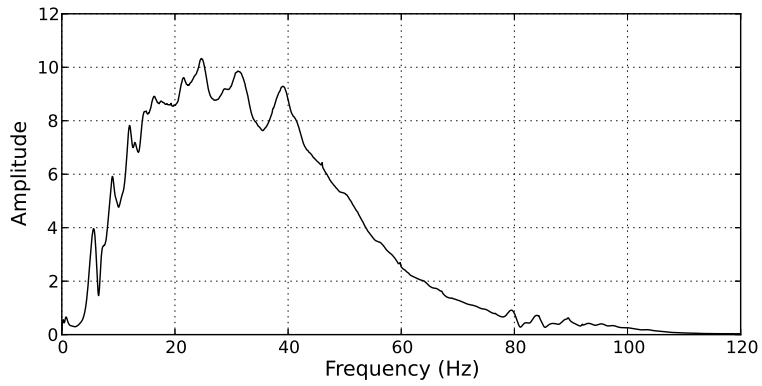
## 3.2 Field data example with the Gulf of Mexico data set

I demonstrated an application of the waveform inversion method for real seismic field data by performing the inversion with a marine data set acquired in the Gulf of Mexico. The field data set was acquired by 396 shots with 50 m intervals. The minimum and maximum offsets are approximately 137 m and 10,321 m, respectively, and the receiver spacing is 25 m. A common-shot gather seismogram and the frequency spectrum of the data are depicted in Fig. 3.29. The field data set has dominant frequency components ranging from 20 to 40 Hz.

The initial velocity model for the waveform inversion is obtained by the Laplace-domain FWI, as shown in Fig. 3.30. FWI in the Laplace-domain is introduced to generate a long-wavelength velocity model from scratch using seismic field data (Shin and Cha, 2008; Ha and Shin, 2013). The grid spacing of the initial velocity model is 25 m and the number of grid points is  $160 \times 795$ . I exploited 81 frequency components ranging from 4 Hz to 16 Hz with 5 damping constants ranging from 0.2 to 1.0. The damping constants are introduced for the waveform inversion of real field data to diminish the effect of noises in the temporally later parts of the seismograms and to focus on the first arrivals. Because the real field data set contains coherent or incoherent noises, pre-processing is required to eliminate the noises. The signals before the first arrivals of the real seismic field data are muted prior to the waveform inversion.



(a)



(b)

Figure 3.29 (a) A common-shot gather seismogram and (b) a frequency spectrum of the Gulf of Mexico field data set.

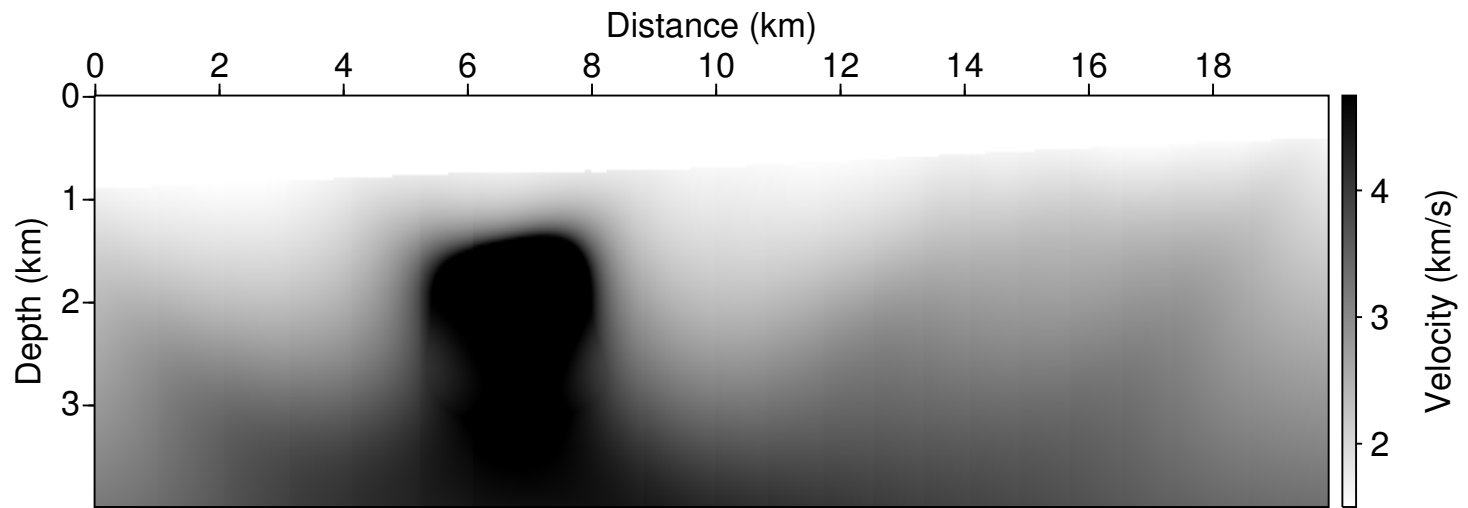


Figure 3.30 The initial velocity model for the waveform inversion of the Gulf of Mexico data set.

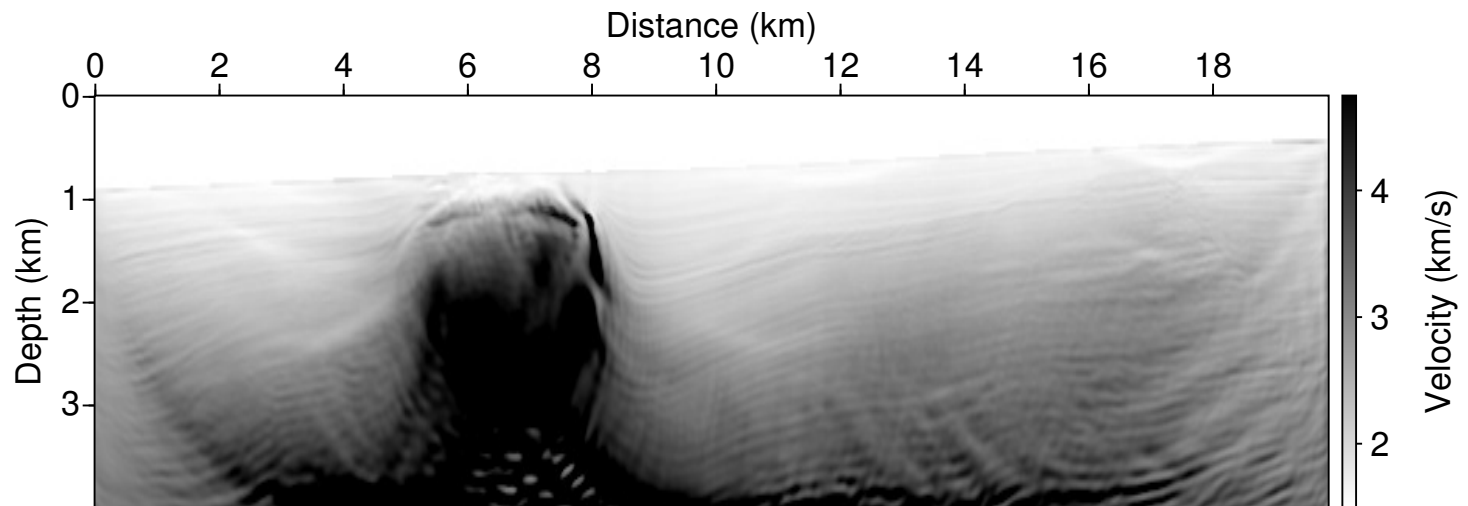


Figure 3.31 The inverted velocity model for the waveform inversion of the Gulf of Mexico data set.

The inverted velocity model is depicted in Fig. 3.31. The inverted velocity model describes the stratified sediment layers around a salt structure better than the initial model. The recovered seismograms are compared with the frequency-filtered seismograms of the input data set as shown in Figs. 3.32, 3.33, 3.34 and 3.35. The synthetic seismograms are damped out at the temporally later parts due to the usage of damping constants. Regardless of the damping, the recovered seismograms match the corresponding seismograms of the real field data set, especially at the temporally earlier parts, including the first arrivals.

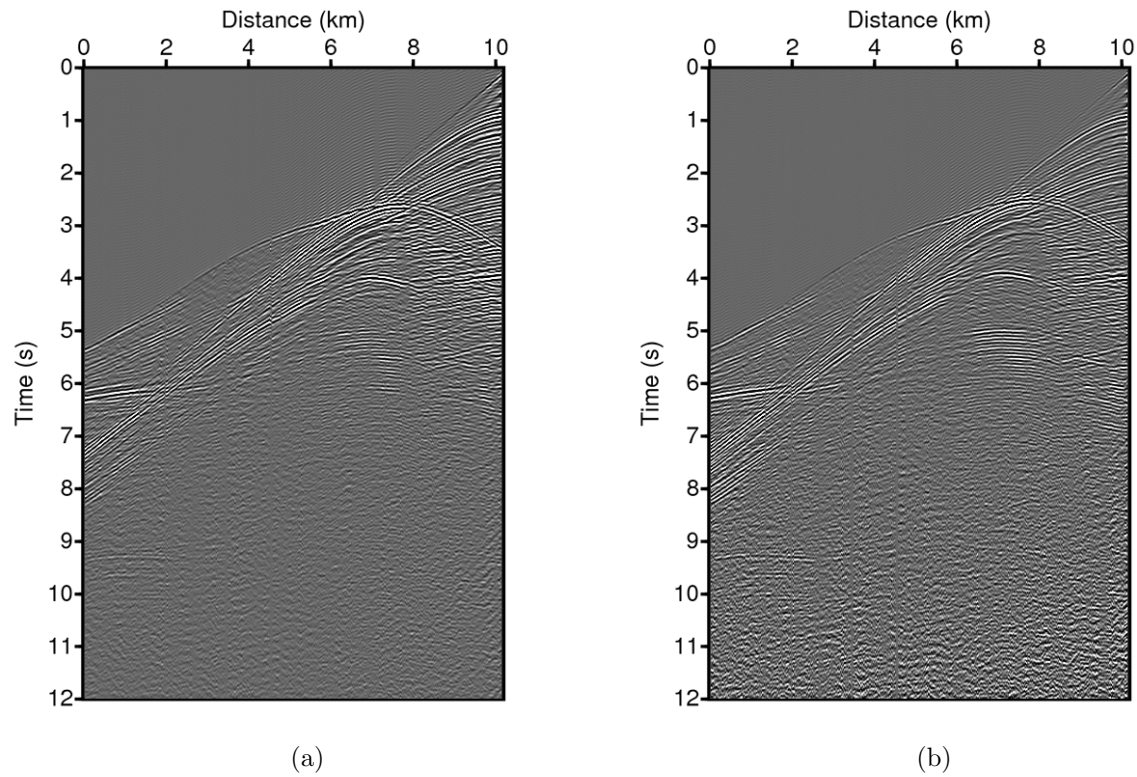


Figure 3.32 The common-shot gather seismograms of the 210th shot of the Gulf of Mexico data set: (a) synthetic seismogram recovered by the waveform inversion and (b) frequency-filtered seismogram of the real field data.

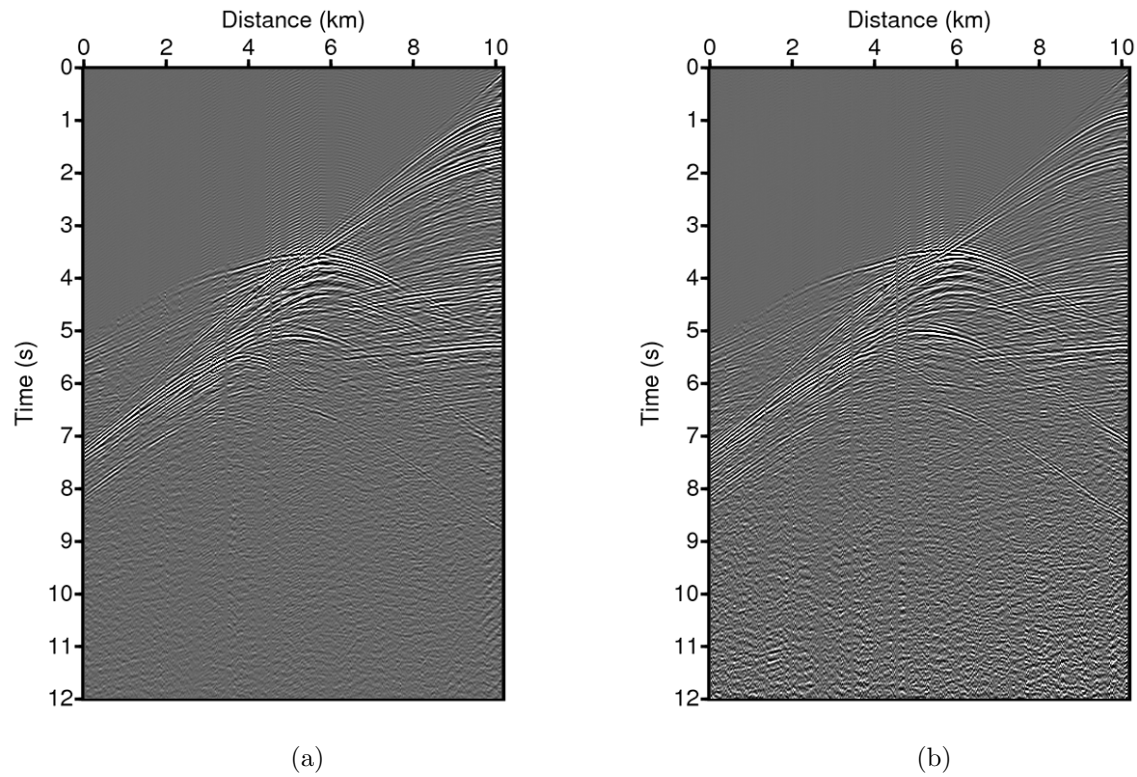


Figure 3.33 The common-shot gather seismograms of the 250th shot of the Gulf of Mexico data set: (a) synthetic seismogram recovered by the waveform inversion and (b) frequency-filtered seismogram of the real field data.

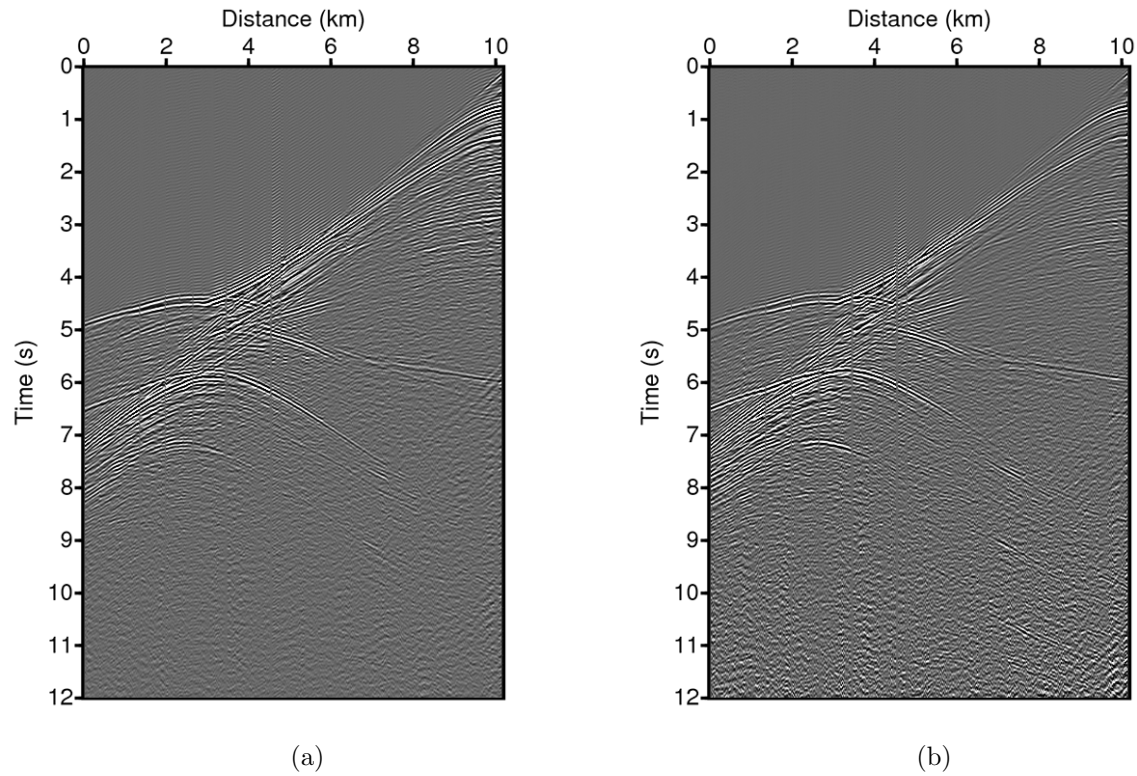


Figure 3.34 The common-shot gather seismograms of the 300th shot of the Gulf of Mexico data set: (a) synthetic seismogram recovered by the waveform inversion and (b) frequency-filtered seismogram of the real field data.

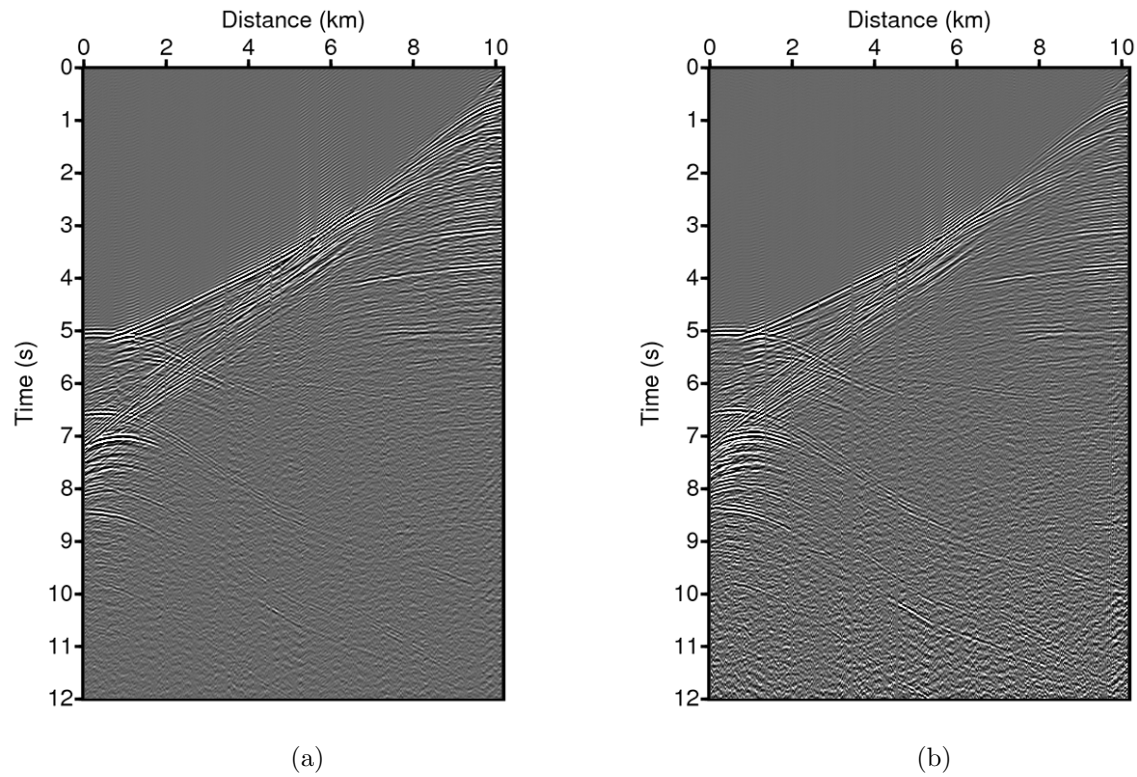
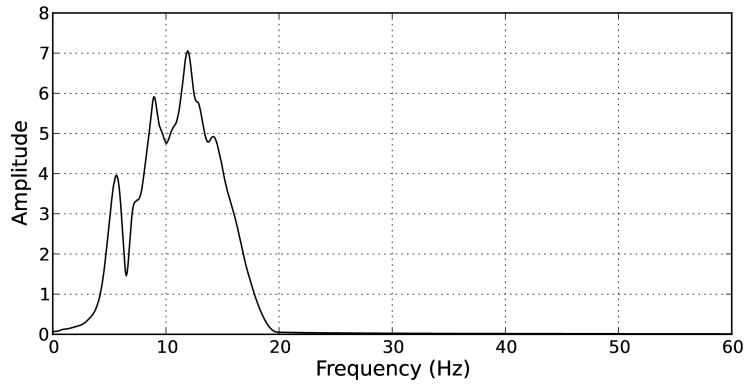
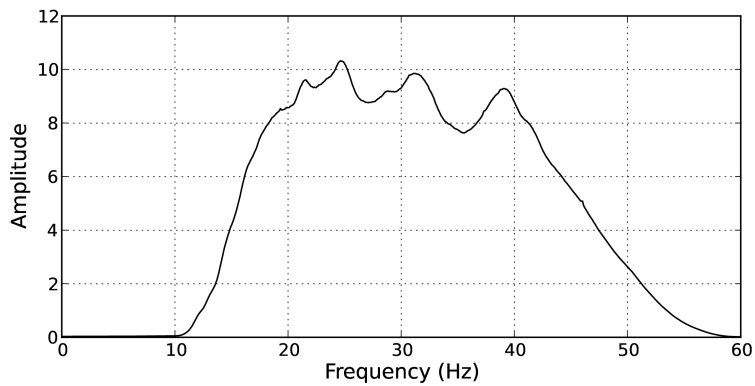


Figure 3.35 The common-shot gather seismograms of the 350th shot of the Gulf of Mexico data set: (a) synthetic seismogram recovered by the waveform inversion and (b) frequency-filtered seismogram of the real field data.

For the real data application, frequency selection is important to the inversion result. I performed three cases of various frequency usage for LSWI the using the Gulf of Mexico data set: employing (1) 2 to 16 Hz frequency components with interval 0.5 Hz without frequency filtering, (2) 4 to 16 Hz frequency components with 0.15 Hz interval after the data set is filtered with a trapezoidal low-pass filter of 0-4-10-20 Hz, and (3) 20 to 32 Hz frequency components with 0.15 Hz interval after the data set is filtered with a trapezoidal high-pass filter of 10-20-40-60 Hz. The frequency spectrums of filtered data sets are presented in Fig. 3.36. The inversion results are depicted in Figs. 3.37, 3.38 and 3.39. Although the frequency selection is expanded to lower frequency, the inversion cannot provide reasonably inverted velocity models if the frequency interval is coarse. Low-pass filtering does not influence on the inversion result if the data set have the low frequency components. Low-frequency components must be first employed prior to proceeding to high-frequency components because the low-frequency components have the long-wavelength information. LSWI cannot recover geological structures if the inversion using high-frequency components starts with initial model that does not include long-wavelength information, similar to FWI.



(a)



(b)

Figure 3.36 The frequency spectrums after the low-pass and high-pass filter is applied: (a) a trapezoidal low-pass filter of 0-4-10-20 Hz and (b) a trapezoidal high-pass filter of 10-20-40-60 Hz.

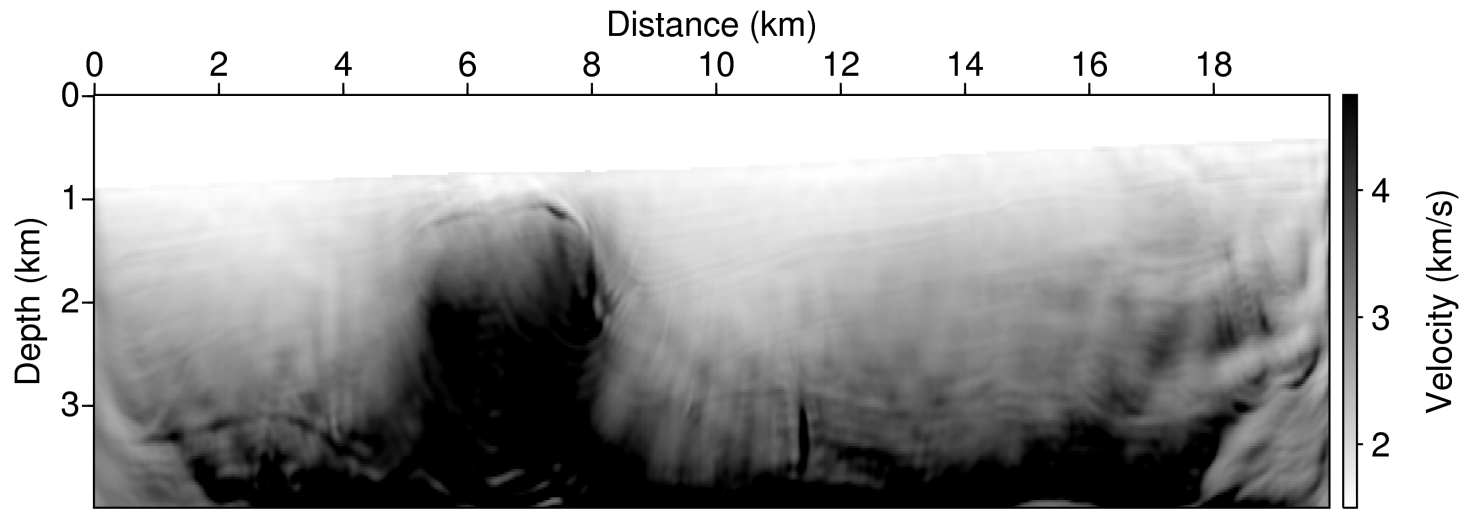


Figure 3.37 The inverted velocity model for the waveform inversion of the Gulf of Mexico data set: 2 to 16 Hz frequency components are employed with interval 0.5 Hz without frequency filtering.

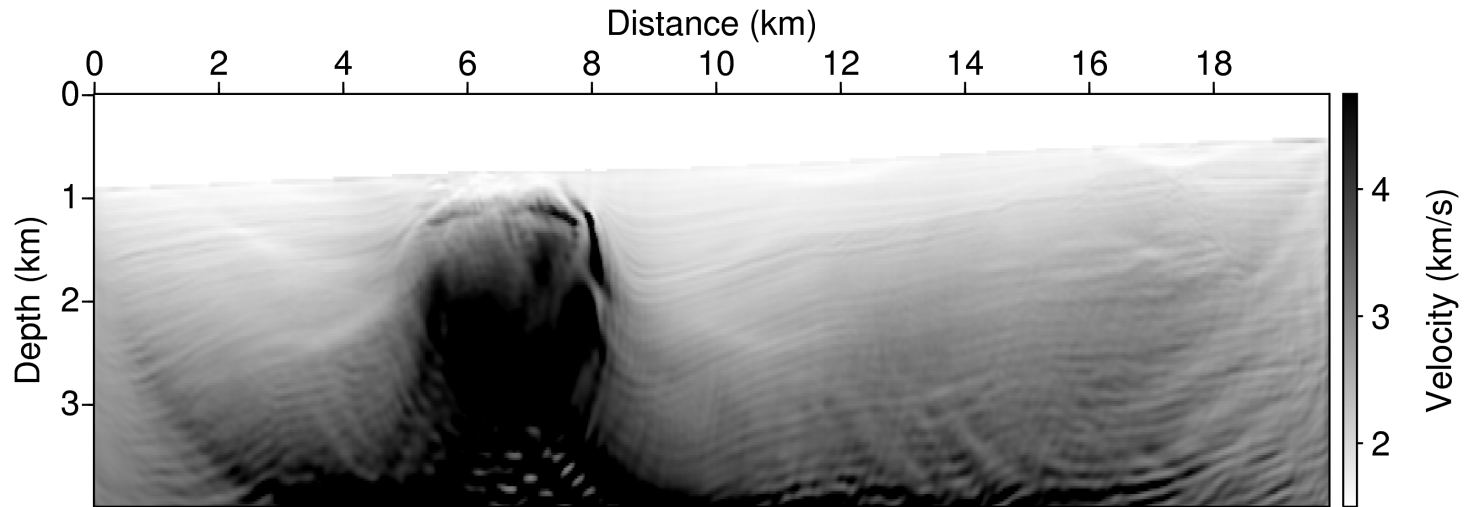


Figure 3.38 The inverted velocity model for the waveform inversion of the Gulf of Mexico data set: 4 to 16 Hz frequency components are employed with 0.15 Hz interval after the data set is filtered with a trapezoidal low-pass filter of 0-4-10-20 Hz.

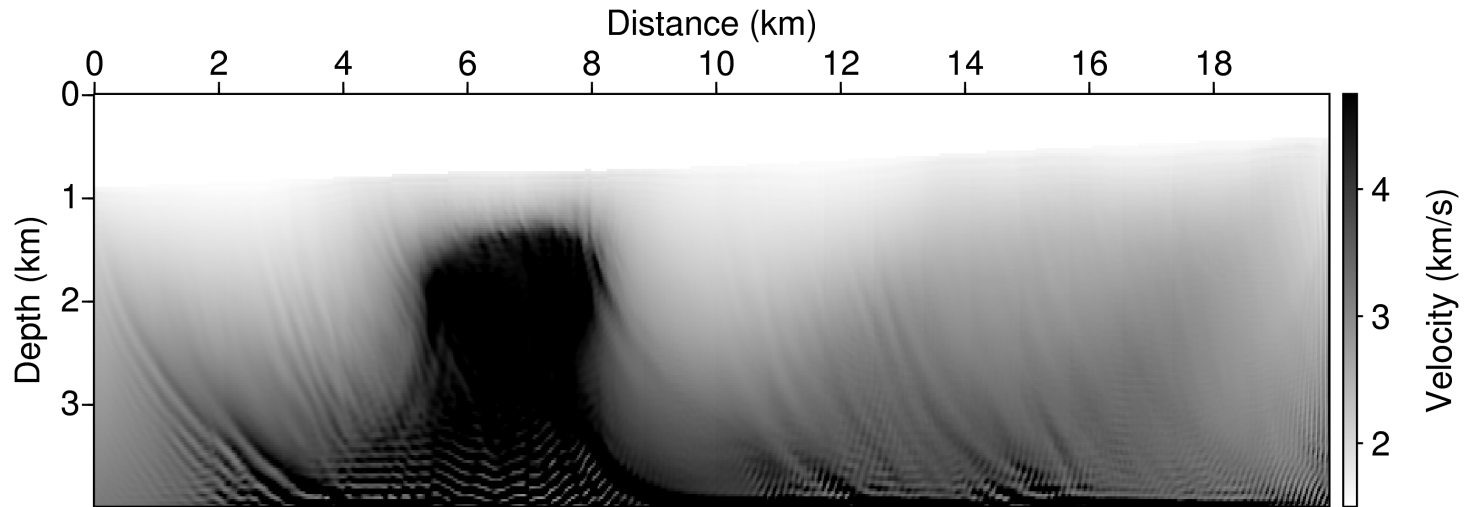


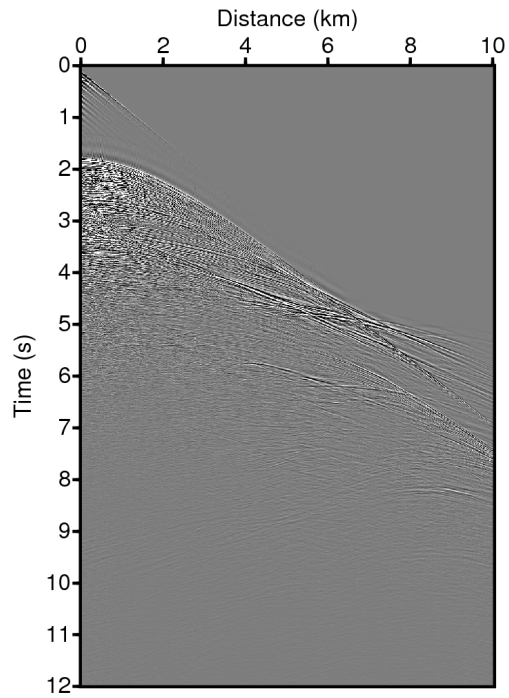
Figure 3.39 The inverted velocity model for the waveform inversion of the Gulf of Mexico data set: 20 to 32 Hz frequency components are employed with 0.15 Hz interval after the data set is filtered with a trapezoidal high-pass filter of 10-20-40-60 Hz.

### 3.3 Field data example with the TOTAL data set

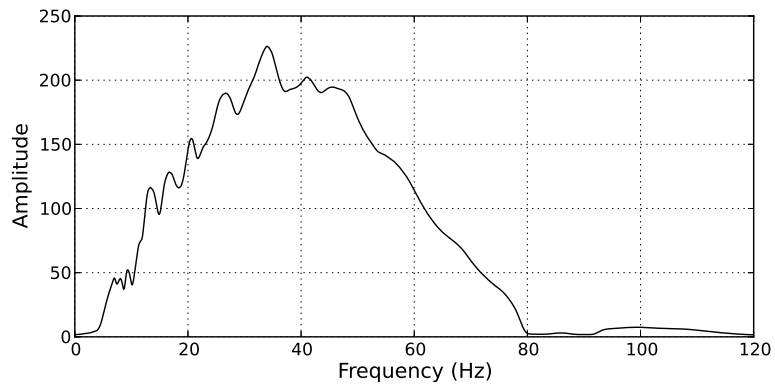
I performed the waveform inversion method with the TOTAL data set. The real seismic field data set was acquired by 1048 shots with 37.5 m intervals. The minimum and maximum offsets are approximately 165 m and 10,203 m, respectively, and the receiver spacing is 12.5 m. A common-shot gather seismogram and the frequency spectrum of the data are depicted in Fig. 3.40. The field data set has dominant frequency components ranging from 15 to 60 Hz.

The initial velocity model for the waveform inversion is obtained by the Laplace-domain FWI, as shown in Fig. 3.41. The signals before the first arrivals of the real seismic field data are muted prior to the waveform inversion. LSWI is implemented with 210 shots with 5-shot intervals. The grid spacing of the initial velocity model is 25 m and the number of grid points is  $240 \times 1689$ . I exploited 81 frequency components ranging from 4 Hz to 16 Hz with 5 damping constants ranging from 0.2 to 1.0.

The inverted velocity model is depicted in Fig. 3.42. The inverted velocity model describes the stratified sediment layers better than the initial model. The recovered seismograms are compared with the frequency-filtered seismograms of the input data set as shown in Figs. 3.43, 3.44 and 3.45. The synthetic seismograms are damped out at the temporally later parts due to the usage of damping constants.



(a)



(b)

Figure 3.40 (a) A common-shot gather seismogram and (b) a frequency spectrum of the TOTAL data set.

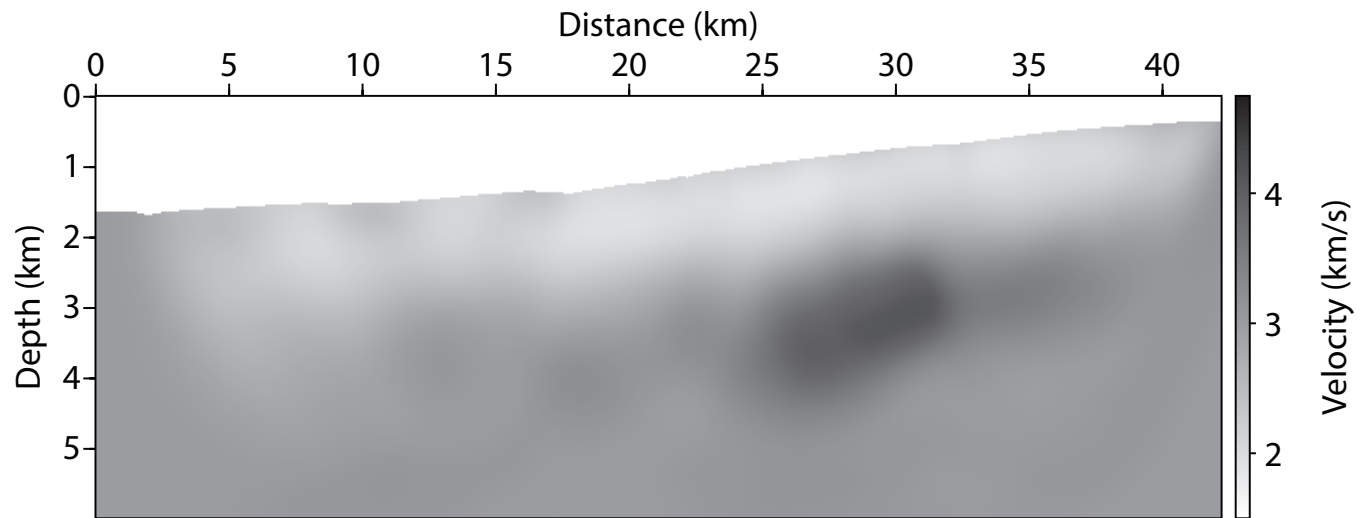


Figure 3.41 The initial velocity model for the waveform inversion of the TOTAL data set.

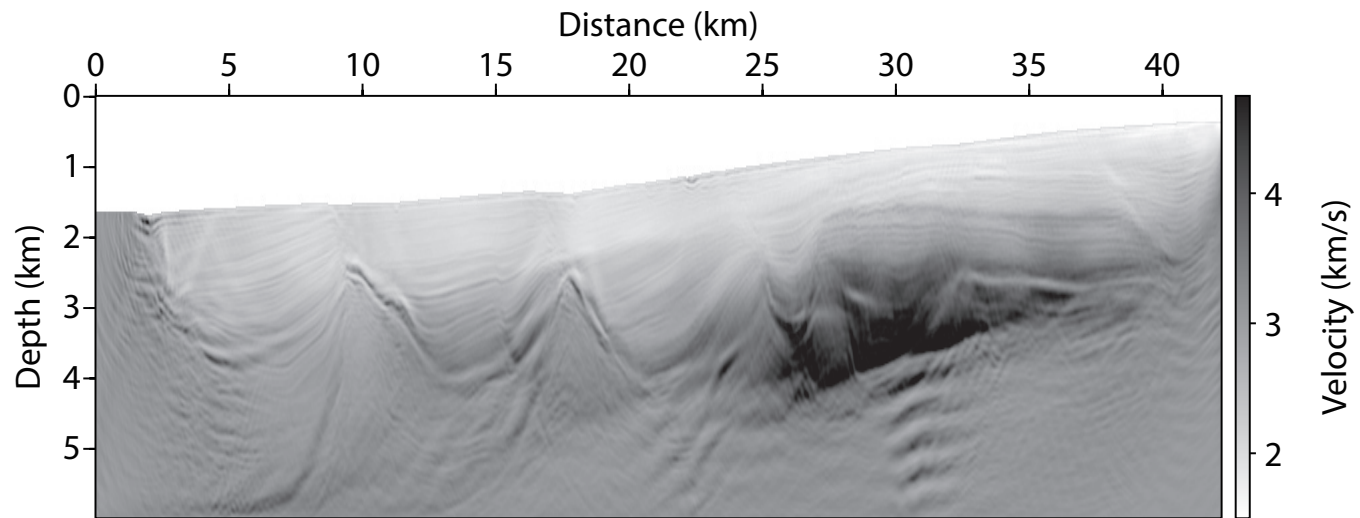


Figure 3.42 The inverted velocity model for the waveform inversion of the TOTAL data set.

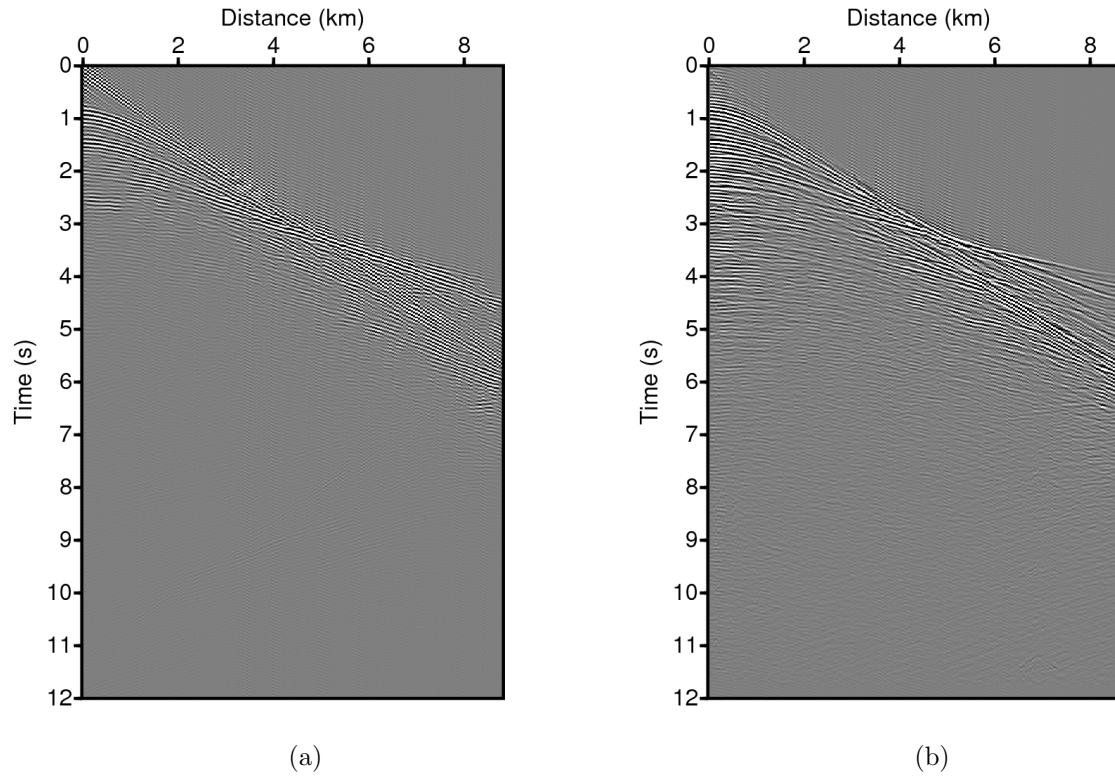


Figure 3.43 The common-shot gather seismograms of the 200th shot of the TOTAL data set: (a) synthetic seismogram recovered by the waveform inversion and (b) frequency-filtered seismogram of the real field data.

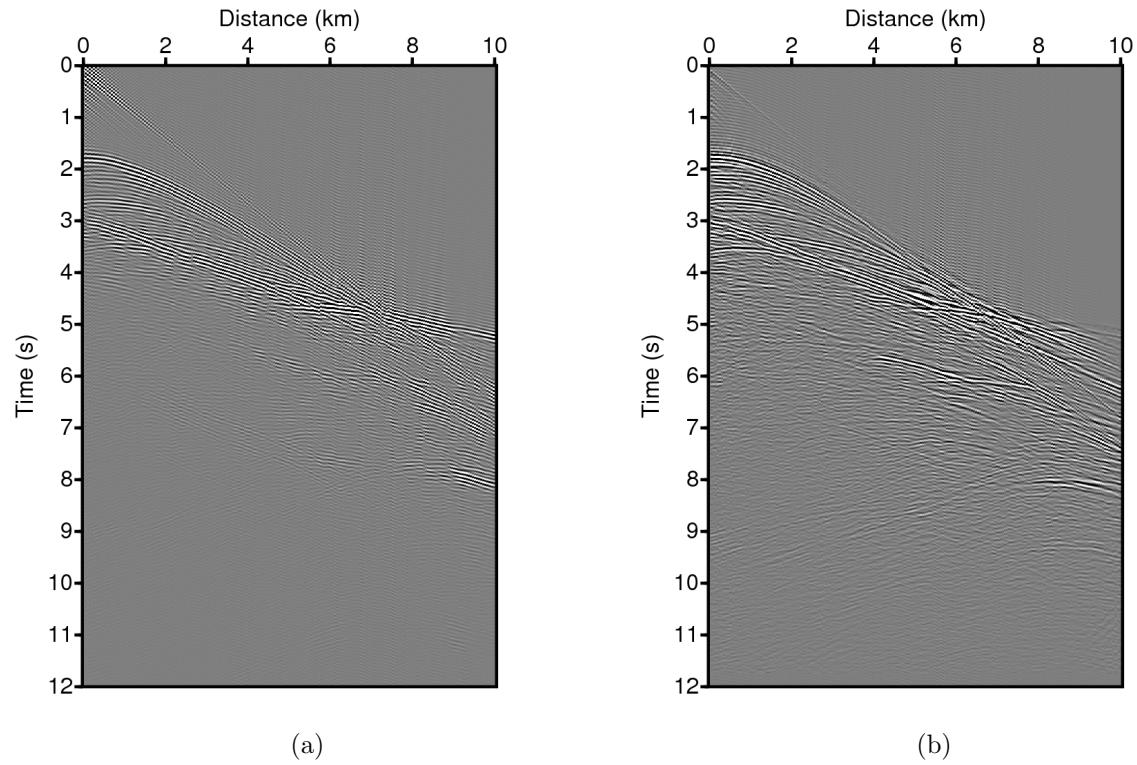


Figure 3.44 The common-shot gather seismograms of the 600th shot of the TOTAL data set: (a) synthetic seismogram recovered by the waveform inversion and (b) frequency-filtered seismogram of the real field data.

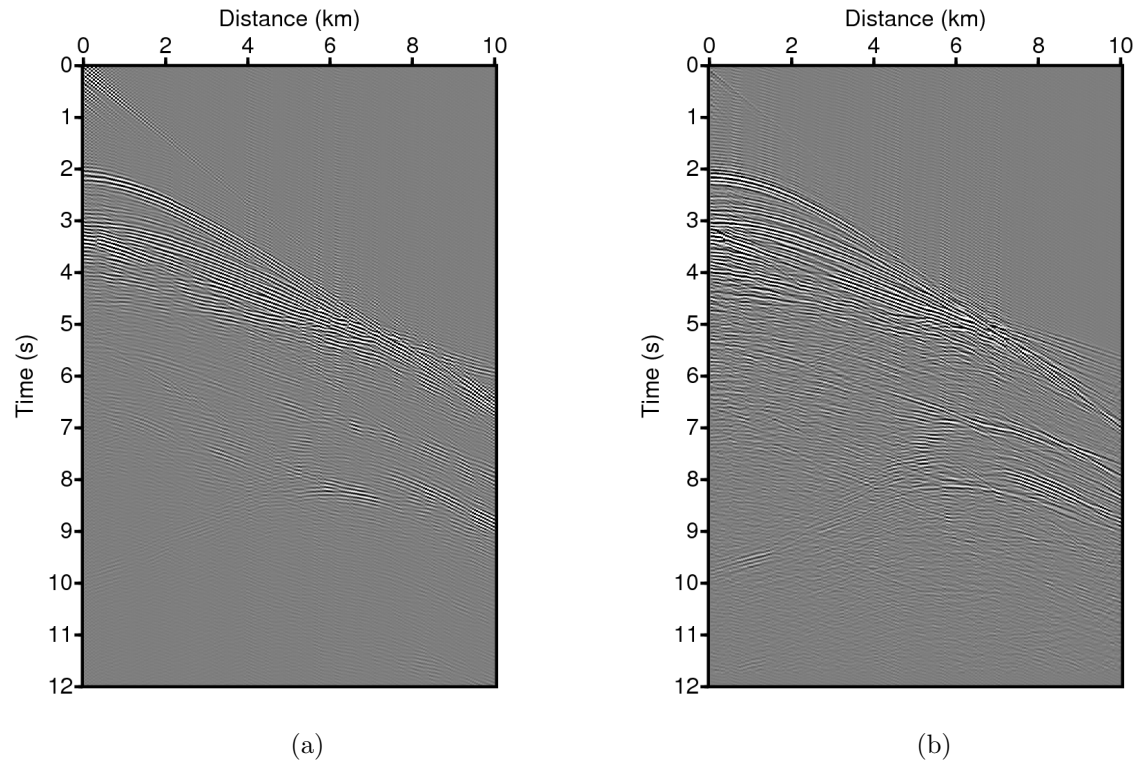


Figure 3.45 The common-shot gather seismograms of the 1000th shot of the TOTAL data set: (a) synthetic seismogram recovered by the waveform inversion and (b) frequency-filtered seismogram of the real field data.

## 4. Discussion

In the previous section, I examined the sensitivity of LSWI solutions to the presence of noise, the lack of low-frequency components and the accuracy of the initial model using Marmousi data examples.

The presence of noise in the seismic field data can influence the LSWI solution. The inversion procedure does not contain a technique to separate the noise and the important signals such as reflections or refractions. Section 3.1.1 suggests that the inversion method cannot correctly describe the subsurface structure of interest because the noises covered the meaningful signals. Nevertheless, LSWI can provide reliable solutions if the input data set has an S/N ratio high enough to reveal the meaningful signals.

The lack of low frequencies in data is a critical requisite for the inversion method to produce trustworthy solutions of updated models. This phenomenon is a general problem in seismic data processing methods implemented in the frequency domain. The use of low-frequency components can make the inverse problem more linear and can lead the solution to the global minimum in frequency-domain FWI. Section 3.1.2 shows that LSWI can update the velocity models that delineate the geological structures of the subsurface if one takes advantage of

low-frequency components in the inversion procedure. Recent advancements in data acquisition promise the presence of low-frequency components in real seismic field data sets.

The accuracy of the initial velocity model is also important for the LSWI to obtain good inverted model due to the single scattering assumption. However, unlike gradient-based FWI, the inversion method does not utilize the local optimization approach. Therefore, solutions of LSWI can delineate dependable velocity models for subsurface media of interest. I demonstrated that the inversion method can derive the intuitive solutions of velocity models to fit the seismic field data in Section 3.1.3.

In the following sections, I discuss the causes of sensitivity to the following factors: noise, frequency component, initial velocity model and numerical solution of Green's function. Moreover, I suggest remedies to deal with these problems and provide the intrinsic characteristics of LSWI.

## 4.1 The presence of noise in data

In Section 3.1.1, I examined the sensitivity of LSWI solutions to the presence of noise in data. The solution of the waveform inversion is influenced by the quality of the input seismic data during the entire inversion procedure. The waveform inversion procedure starts from the estimation of the source signature from the seismic field data and the forward-modeled data as the impulse response. Forward modeling prior to the source estimation produces only noise-free data as the impulse response of the reference velocity model and cannot distinguish noises included in the seismic field data. Accordingly, the data residual contains noises that affect the formulation of virtual scattering sources. Because the virtual scattering source is related to most of the intermediate outputs (scattered wavefield, total wavefield, slowness perturbation, etc.) in the inversion, the solution is influenced by the quality of the input seismic data. Therefore, every effort should be made to reduce noises in the field data acquisition and to remove noises in seismic data by pre-processing for waveform inversion because the resultant model will depend on the data errors as well as the data themselves (Constable et al., 1987).

For the application of real field data, noises in seismic data should be carefully eliminated by pre-processing. Generally, various types of noise contaminate real field data set. The low S/N ratio of the input data can cause inaccurate estimations of slowness perturbations. The inversion method reconstructs the total wavefield, including noise which is regarded as a type of signal. To obtain good inverted velocity models, noises in the input data (coherent noises in particular) should be eliminated without ruining the important signals such as reflections or refractions. Therefore, pre-processing is required to remove or reduce the noises included in the data set and to obtain reasonable inversion results from noise-contaminated

data. The development of a stabilization technique for noise-contaminated data would be helpful. On the other hand, multiples of input data do not need to be eliminated because this inversion method employs the solutions of the full wave equation as forward modeling during the entire process, similar to FWI. However, coherent noise should be removed properly. If not, the waveform inversion might produce virtual scattering sources for the scattered wavefields including the coherent noise.

Because the amplitudes and phases of the input data set are critical for the inversion result, several pre-processing techniques, such as trace balancing and gain control, are also required. Geometric spreading corrections should be applied to compensate for wavefront divergence by pre-processing for real field data sets. Although the waveform inversion algorithm eliminates the effect caused by a difference of magnitude between different common-shot gather seismograms, trace balancing will be helpful for source wavelet estimation, etc. The assumption of wave propagation in two-dimensional media requires gain control or compensation for geometrical spreading until three-dimensional simulation is applicable in terms of computational cost.

## 4.2 The lack of low frequencies in data

The contribution of low-frequency components on the inversion result is clarified by the sensitivity test of numerical examples in Section 3.1.2. Sirgue and Pratt (2004) and Sirgue (2006) examined the importance of low-frequency components for FWI. Proper reconstruction of the velocity model implies the recovery of a continuous range of wavenumbers from the low to the high end of the spatial spectrum (Sirgue, 2006). Moreover, the low-frequency components of data exhibit a more linear relation with the low-wavenumber components of model, and the chance of locating the global minimum is diminished if this information is not used at an early stage of the inversion (Sirgue and Pratt, 2004). LSWI also depends on the selection of frequency components because it exploits the full-wavefield modeling in the frequency domain, similar to FWI.

The proposed waveform inversion method can be performed with the simultaneous or sequential usage of frequency components, and I adopted the sequential frequency strategy in this study to update the initial velocity model. The simultaneous frequency strategy first estimates the perturbation of slowness for every frequency component employed in the inversion starting from the initial velocity model. The initial velocity model is only updated once for the inversion to provide a final updated result. The sequential frequency strategy first estimates the perturbation of slowness for the lowest frequency component employed in the inversion starting from the initial velocity model. The initial velocity model is updated for the lowest frequency and the inversion procedure moves to the next frequency. This technique employs a type of frequency-marching and requires iterative updates of the number of frequencies employed for the waveform inversion. Given that low-frequency data are more linear with respect to the model pertur-

bations than high-frequency data, the sequential frequency strategy dramatically improves the chance for the inversion to locate the global minimum of the full, wide-band inverse problem (Sirgue and Pratt, 2004).

The selection of the frequency band for the waveform inversion is very important to utilize the quantitative information contained in the seismic field data. The waveform inversion algorithm eliminates the effect on the computed slowness perturbation caused by the distribution of the frequency spectrum. Nevertheless, the usage of frequency components should be carefully determined. A strategy to select temporal frequencies for the effective FWI proposed by Sirgue and Pratt (2004) is based on the coverage of frequencies related to wavenumbers and wavelengths, and the strategy might be useful for LSWI. For the low frequency information, seismic data acquisition technology has been developed to widen the frequency spectrum of data sets to approximately 1 Hz (Plessix et al., 2010, 2012; Baeten et al., 2013). If a wide range of offsets is available, the waveform inversion using low frequency components can provide reliable velocity models that recover long- to short-wavelength components with high resolution.

### 4.3 The accuracy of the initial models

The accuracy of the initial velocity model is important for the waveform inversion as examined in Section 3.1.3. Solutions of the waveform inversion depend on the initial model and the frequency components, as does FWI solutions. The inversion updates the initial velocity model with the computed perturbation of slowness in sequential order from low to high frequencies. As a result, an inversion that begins from the initial velocity model can provide a reliable background velocity model for seismic migration even if the initial model is relatively divergent from the actual model. However, good initial models are still important for the waveform inversion to identify reliable solutions of updated velocity models due to the single scattering assumption.

The waveform inversion is based on the Lippmann-Schwinger equation, a fundamental equation of scattering theory. As an inverse scattering problem, this inversion method assumes small changes in the physical properties of the medium. Therefore, solutions of the waveform inversion are influenced by the magnitude of medium perturbations to be estimated during the inversion procedure. In other words, the initial velocity models should not be divergent from the actual velocity model as a mathematically defined medium of interest. The problem related to the accuracy of initial models is the same as that of gradient-based FWI. LSWI can provide more reliable and intuitive solutions compared with FWI, because LSWI is a direct inversion method.

Weglein et al. (2009) mentioned that the direct inverse methods are the inverse methods that input seismic data and directly output medium properties or other seismic data processing objectives. LSWI is a direct inversion method,

which does not exploit the local optimization approach with a data fitting procedure and directly estimates the medium perturbation through the perturbation operator. In addition, this method is a type of linear inverse method because the inversion introduces perturbation of slowness (i.e., square of slowness) to estimate medium perturbation. The acoustic wave equation employed for the forward modeling has an indisputable nonlinear relationship between changes in medium properties and concomitant changes in the wavefields (Weglein et al., 2009). On the other hand, the slowness perturbation is linear to the concomitant change in wavefields (i.e., scattered wavefield). With the linearity of slowness, the direct waveform inversion can provide intuitive solutions in which the recovered seismograms automatically match the seismic field data. This characteristic is analogous to that of the Occam's inversion proposed by Constable et al. (1987), which solves the simplified and linearized inverse problem to avoid the non-uniqueness of the geophysical problem.

The inversion of actual field data from a geophysical exploration/survey cannot yield a unique solution. The non-uniqueness of the solution is one of the major obstacles in seismic waveform inversion, as is the case in many geophysical inverse problems, such as gradient-based FWI (Böhm and Vesnaver, 1999; Ha et al., 2012; Saltzer et al., 2006; Vasco et al., 1996). To demonstrate the non-uniqueness problem in the proposed waveform inversion algorithm, numerical examples are presented that are initiated by several different initial velocity models in Section 3.1.3. Various solutions of inverted models depend on the initial velocity models, whereas no outstanding differences were identified in the reconstructed common-shot gather seismograms. The non-uniqueness problem may be considered as exclusively caused by the single scattering assumption. However, the non-uniqueness of solutions is a common problem in the geophysics.

It is more difficult to derive dependable inversion results from the simultaneous estimation of density and bulk modulus using acoustic pressure data because it is the under-determined inverse problem with more unknowns. Although one exploits the elastic wave equation for forward modeling and takes the multi-components of data as the input, the non-uniqueness problem does not vanish. Furthermore, nonlinearity becomes more critical in the case of elastic parameter inversion because the waveform inversion method is a type of linear approach to compute slowness perturbation through the modeling operator. I excluded various potentials of the inversion method by introducing the slowness perturbation while assuming an acoustic medium. However, the inverse problem becomes much simpler and therefore provides solutions that are similar to the actual medium.

## 4.4 Green's function and the assumption of acoustic media

In this study, it is assumed that the numerical solution of the acoustic wave equation with constant density is a Green's function. However, the numerical solution cannot exactly describe the behavior of the seismic waves as they propagate through subsurface media. If one exploits the solution of the elastic wave equation, the forward modeling solution describes the propagation of seismic waves more precisely; however, it requires more computational cost to obtain the solution. I employed forward modeling of the acoustic wave equation for the trade-off between numerical accuracy and efficiency. Given the waveform inversion only delineates the P-wave velocity of the medium, it has the limitation of estimating the physical parameters of real subsurface elastic media. On the contrary, it is difficult to update elastic media using marine field data due to nonlinearity and the under-determined inverse problem. Given the assumption of acoustic media, the waveform inversion can delineate relatively accurate velocity models of subsurface media.

Real data application of waveform inversion, especially land data, are difficult due to the quality of the data, surface waves such as Rayleigh waves, topographic effects, etc. If the waveform inversion employs the acoustic wave equation for forward modeling, substantial differences may exist between land data and modeled data. The waveform inversion method attempts to fit the data residual and reconstruct the scattered wavefield. Therefore, the signals caused by surface and elastic wave propagation must be removed through appropriate pre-processing prior to the waveform inversion.

## 5. Conclusions

In this study, I proposed a frequency-domain waveform inversion method based on the Lippmann-Schwinger equation, which is the fundamental equation of scattering theory. Lippmann-Schwinger waveform inversion (LSWI) solves the inverse scattering problem, which inputs the reference velocity model, the reference wavefield and values of the actual wavefield on the measurement surface and outputs the difference between the actual and reference models through the perturbation operator. I employed the forward modeling of the acoustic wave equation to use Green's function of wave propagation in the subsurface media, similar to FWI. On the other hand, LSWI is a direct inverse method that directly determines perturbation of slowness (i.e., square of slowness), whereas gradient-based FWI uses a local optimization approach with an iterative data fitting procedure.

Inverse scattering series based on the Lippmann-Schwinger equation has been utilized in various studies for multiple attenuation, deghosting, downward continuation, and so forth. Among those studies, the inversion proposed by Zhang and Weglein (2009a,b) is an inversion method that distinguishes imaging-only and inversion-only scattering terms to determine physical properties. However, LSWI directly determines the perturbation of properties without that type of distinction. Moreover, LSWI takes advantage of the forward modeling of the acoustic wave

equation, which can account for full-waveform of the wave propagations in the subsurface media, whereas the inversion method of Zhang and Weglein (2009a,b) uses amplitudes of reflections.

LSWI is a process for estimating the perturbation of slowness as the difference between the subsurface medium of interest and the reference model. LSWI yields a linearly approximated solution by introducing slowness perturbation. In addition, LSWI does not require step lengths to update the velocity model, because it directly inverts the perturbation of slowness as medium perturbation between the actual and reference velocity model. Accordingly, if the computing time for virtual scattering source is reduced, the computational cost required to perform the inversion is less than that of gradient-based FWI, which requires numerous forward modeling and back-propagation steps. Then, LSWI can be used as a preliminary study for 3D waveform inversion or as a more competitive alternative to gradient-based FWI.

On the other hand, LSWI can avoid the problem of local minima, an obstacle in FWI. As a direct inversion method, LSWI does not search for the solutions locally or globally and leads to an intuitive and simple solution that can produce synthetic seismograms similar to those of the given data set. The linear relationship between the slowness and wavefield also makes the inverse problem easier. Because of the single scattering assumption, initial velocity models similar to the exact solution are required to generate a trustworthy inversion result. Even if the initial model is poor, LSWI recovers the synthetic seismograms, which can confirm that the inverted velocity model provides a reasonable solution to the inverse problem in the data domain. However, the sequential frequency strategy helps LSWI overcome this limitation and produce updated velocity models includ-

ing long- to short-wavenumber components with high resolution. Although the non-uniqueness problem remains for the poor initial models, LSWI can provide dependable background velocity models for migration.

For the real data application, several factors can influence the inversion results. Noises in the seismic data, except the internal multiples, must be carefully removed because the inversion result can be affected by the intrinsic characteristics of the inversion algorithm. Therefore, appropriate pre-processing steps to eliminate noises in the input seismic data should be performed prior to the inversion procedure. Concurrently, the data set should contain the meaningful low-frequency components required to recover the long-wavelength velocity model. Moreover, it is important that the initial velocity model is similar to the medium of interest to obtain reasonable inversion results due to the single scattering assumption. At the same time, the non-uniqueness aspect of the inverse method remains a common problem in geophysical data interpretations.

Further studies are required for the application of LSWI to real data. Most of the problems for the real data application of LSWI are analogous to those of FWI. The actual wave propagation in subsurface media is complicated due to the elastic and anisotropic properties of the media. The consideration of elastic waves can help the inversion achieve a more exact solution. The solutions of LSWI also depends on the initial velocity model even if the sequential frequency strategy is selected. On the other hand, the limited offsets of marine streamer data are also problematic for building the velocity model because the lack of data residuals is a hindrance to formulating a virtual scattering source during the inversion procedure. A divide-and-conquer approach that updates velocity model part-by-part with (under) the existence of data residual can be considered as a

solution for the limited offset problem of marine field data.

# References

- Amundsen, L., A. Reitan, B. Arntsen, and B. Ursin, 2006, Acoustic nonlinear amplitude versus angle inversion and data-driven depth imaging in stratified media derived from inverse scattering approximations: *Inverse problems*, **22**, 1921.
- Baeten, G., J. W. de Maag, R.-E. Plessix, R. Klaassen, T. Qureshi, M. Kleemeyer, F. t. Kroode, and Z. Rujie, 2013, The use of low frequencies in a full-waveform inversion and impedance inversion land seismic case study: *Geophysical Prospecting*, **61**, 701–711.
- Beylkin, G., 1985, Imaging of discontinuities in the inverse scattering problem by inversion of a causal generalized radon transform: *Journal of Mathematical Physics*, **26**, 99–108.
- Beylkin, G., and R. Burridge, 1990, Linearized inverse scattering problems in acoustics and elasticity: *Wave motion*, **12**, 15–52.
- Böhm, G., and A. L. Vesnaver, 1999, In quest of the grid: *Geophysics*, **64**, 1116–1125.
- Brenders, A., and R. Pratt, 2007, Efficient waveform tomography for lithospheric imaging: implications for realistic, two-dimensional acquisition geometries and

- low-frequency data: *Geophysical Journal International*, **168**, 152–170.
- Carcione, J. M., G. C. Herman, and A. Ten Kroode, 2002, Seismic modeling: *Geophysics*, **67**, 1304–1325.
- Clayton, R., and B. Engquist, 1977, Absorbing boundary conditions for acoustic and elastic wave equations: *Bulletin of the Seismological Society of America*, **67**, 1529–1540.
- Clayton, R. W., and R. H. Stolt, 1981, A Born-WKBJ inversion method for acoustic reflection data: *Geophysics*, **46**, 1559–1567.
- Constable, S. C., R. L. Parker, and C. G. Constable, 1987, Occam’s inversion: A practical algorithm for generating smooth models from electromagnetic sounding data: *Geophysics*, **52**, 289–300.
- Davies, A. J., 1980, *The finite element method: a first approach*: Oxford, Clarendon Press.
- Forel, D., T. Benz, and W. D. Pennington, 2005, *Seismic data processing with seismic unix*: Society of Exploration Geophysicists.
- Frayssé, V., L. Giraud, S. Gratton, and J. Langou, 2005, Algorithm 842: A set of gmres routines for real and complex arithmetics on high performance computers: *ACM Transactions on Mathematical Software (TOMS)*, **31**, 228–238.
- Gauthier, O., J. Virieux, and A. Tarantola, 1986, Two-dimensional nonlinear inversion of seismic waveforms: Numerical results: *Geophysics*, **51**, 1387–1403.
- Geller, R. J., and T. Hara, 1993, Two efficient algorithms for iterative linearized inversion of seismic waveform data: *Geophysical Journal International*, **115**, 699–710.

- Guitton, A., and T. Alkhalifah, 2013, An introduction to this special section: Full-waveform inversion and the way forward: *The Leading Edge*, **32**, 1026–1028.
- Ha, W., W. Chung, S. Shin, and C. Shin, 2012, Non-uniqueness of waveform inversions in the Laplace domain: *Geosystem Engineering*, **15**, 151–156.
- Ha, W., and C. Shin, 2013, Why do Laplace-domain waveform inversions yield long-wavelength results?: *Geophysics*, **78**, R167–R173.
- Ikelle, L., and L. Amundsen, 2005, *Introduction to petroleum seismology*: Society of Exploration Geophysicists.
- Ikelle, L. T., 1999, Using even terms of the scattering series for deghosting and multiple attenuation of ocean-bottom cable data: *Geophysics*, **64**, 579–592.
- Innanen, K. A., 2009, Born series forward modelling of seismic primary and multiple reflections: an inverse scattering shortcut: *Geophysical Journal International*, **177**, 1197–1204.
- Kim, J. H., and S. J. Kim, 1999, Multifrontal solver combined with graph partitioners: *AIAA journal*, **37**, 964–970.
- Lailly, P., 1983, The seismic inverse problem as a sequence of before stack migrations: *Conference on inverse scattering: theory and application*, Society for Industrial and Applied Mathematics, 206–220.
- Lippmann, B. A., and J. Schwinger, 1950, Variational principles for scattering processes. i: *Physical Review*, **79**, 469.
- Lo, T.-w., and P. L. Inderwiesen, 1994, *Fundamentals of seismic tomography*: Society of Exploration Geophysicists.

- Marfurt, K. J., 1984, Accuracy of finite-difference and finite-element modeling of the scalar and elastic wave equations: *Geophysics*, **49**, 533–549.
- Mora, P., 1987, Nonlinear two-dimensional elastic inversion of multioffset seismic data: *Geophysics*, **52**, 1211–1228.
- Nolet, G., 1987, *Seismic tomography: with applications in global seismology and exploration geophysics*: Springer.
- Officer, C. B., and R. R. Shrock, 1958, *Introduction to the theory of sound transmission: With application to the ocean*: McGraw-Hill.
- Plessix, R.-É., G. Baeten, J. W. de Maag, M. Klaassen, Z. Rujie, T. Zhifei, et al., 2010, Application of acoustic full waveform inversion to a low-frequency large-offset land data set: 80th SEG Annual Meeting, Society of Exploration Geophysicists.
- Plessix, R.-É., G. Baeten, J. W. de Maag, F. ten Kroode, and Z. Rujie, 2012, Full waveform inversion and distance separated simultaneous sweeping: a study with a land seismic data set: *Geophysical Prospecting*, **60**, 733–747.
- Pratt, G., C. Shin, et al., 1998, Gauss–newton and full newton methods in frequency–space seismic waveform inversion: *Geophysical Journal International*, **133**, 341–362.
- Pratt, R. G., 1990, Inverse theory applied to multi-source cross-hole tomography.: *Geophysical Prospecting*, **38**, 311–329.
- , 1999, Seismic waveform inversion in the frequency domain, part 1: Theory and verification in a physical scale model: *Geophysics*, **64**, 888–901.
- Ravaut, C., S. Operto, L. Improta, J. Virieux, A. Herrero, and P. Dell’Aversana,

- 2004, Multiscale imaging of complex structures from multifold wide-aperture seismic data by frequency-domain full-waveform tomography: application to a thrust belt: *Geophysical Journal International*, **159**, 1032–1056.
- Rawlinson, N., S. Pozgay, and S. Fishwick, 2010, Seismic tomography: a window into deep earth: *Physics of the Earth and Planetary Interiors*, **178**, 101–135.
- Saltzer, R., C. Finn, et al., 2006, Exploiting the non-uniqueness of seismic inversion to obtain alternate scenarios of economic interest: 76th SEG Annual Meeting, Society of Exploration Geophysicists, 1670–1673.
- Shin, C., and Y. H. Cha, 2008, Waveform inversion in the Laplace domain: *Geophysical Journal International*, **173**, 922–931.
- , 2009, Waveform inversion in the Laplace-Fourier domain: *Geophysical Journal International*, **177**, 1067–1079.
- Shin, C., S. Pyun, and J. Bednar, 2007, Comparison of waveform inversion, part 1: conventional wavefield vs logarithmic wavefield: *Geophysical Prospecting*, **55**, 449–464.
- Shipp, R. M., and S. C. Singh, 2002, Two-dimensional full wavefield inversion of wide-aperture marine seismic streamer data: *Geophysical Journal International*, **151**, 325–344.
- Sirgue, L., 2006, The importance of low frequency and large offset in waveform inversion: 68th EAGE Conference & Exhibition, European Association of Geoscientists and Engineers.
- Sirgue, L., and R. G. Pratt, 2004, Efficient waveform inversion and imaging: A strategy for selecting temporal frequencies: *Geophysics*, **69**, 231–248.

- Stolk, C. C., and M. V. de Hoop, 2006, Seismic inverse scattering in the downward continuation approach: *Wave Motion*, **43**, 579–598.
- Tarantola, A., 1984, Inversion of seismic reflection data in the acoustic approximation: *Geophysics*, **49**, 1259–1266.
- Taylor, J. R., 1972, *Scattering theory: the quantum theory of nonrelativistic collisions*: Wiley.
- Trampert, J., 1998, Global seismic tomography: the inverse problem and beyond: *Inverse Problems*, **14**, 371.
- Tromp, J., C. Tape, and Q. Liu, 2005, Seismic tomography, adjoint methods, time reversal and banana-doughnut kernels: *Geophysical Journal International*, **160**, 195–216.
- Varela, C. L., P. L. Stoffa, and M. K. Sen, 1998, Background velocity estimation using non-linear optimization for reflection tomography and migration misfit: *Geophysical prospecting*, **46**, 51–78.
- Vasco, D. W., J. E. Peterson Jr, and E. L. Majer, 1996, Nonuniqueness in travelttime tomography: Ensemble inference and cluster analysis: *Geophysics*, **61**, 1209–1227.
- Versteeg, R., 1994, The marmousi experience: Velocity model determination on a synthetic complex data set: *The Leading Edge*, **13**, 927–936.
- Vigh, D., N. Moldoveanu, K. Jiao, W. Huang, and J. Kapoor, 2013, Ultralong-offset data acquisition can complement full-waveform inversion and lead to improved subsalt imaging: *The Leading Edge*, **32**, 1116–1122.
- Virieux, J., and S. Operto, 2009, An overview of full-waveform inversion in explo-

- ration geophysics: *Geophysics*, **74**, WCC1–WCC26.
- Weglein, A. B., F. V. Araújo, P. M. Carvalho, R. H. Stolt, K. H. Matson, R. T. Coates, D. Corrigan, D. J. Foster, S. A. Shaw, and H. Zhang, 2003, Inverse scattering series and seismic exploration: Inverse problems, **19**, R27.
- Weglein, A. B., F. A. Gasparotto, P. M. Carvalho, and R. H. Stolt, 1997, An inverse-scattering series method for attenuating multiples in seismic reflection data: *Geophysics*, **62**, 1975–1989.
- Weglein, A. B., H. Zhang, A. C. Ramírez, F. Liu, and J. E. Lira, 2009, Clarifying the underlying and fundamental meaning of the approximate linear inversion of seismic data: *Geophysics*, **74**, WCD1–WCD13.
- Woodward, M. J., 1992, Wave-equation tomography: *Geophysics*, **57**, 15–26.
- Woodward, M. J., D. Nichols, O. Zdraveva, P. Whitfield, and T. Johns, 2008, A decade of tomography: *Geophysics*, **73**, VE5–VE11.
- Yilmaz, Ö., 2001, *Seismic data analysis*: Society of Exploration Geophysicists.
- Zhang, H., and A. B. Weglein, 2009a, Direct nonlinear inversion of 1d acoustic media using inverse scattering subseries: *Geophysics*, **74**, WCD29–WCD39.
- , 2009b, Direct nonlinear inversion of multiparameter 1d elastic media using the inverse scattering series: *Geophysics*, **74**, WCD15–WCD27.
- Zienkiewicz, O. C., R. L. Taylor, and J. Z. Zhu, 2005, *The finite element method: its basis and fundamentals*, 7th ed.: Butterworth-Heinemann.



# 초 목

## 리프먼-슈윙거 방정식에 기초한 주파수영역 탄성파 파형역산

곽 상 민

에너지시스템공학부

서울대학교 대학원

탄성파 자료 처리 기술 중 하나인 파형 역산은 탄성파 탐사 자료로부터 탐사 대상 지하 매질의 물성을 추정하는 지하 구조 영상화 방법이다. 전(全)파형 역산(FWI)은 파동 전파의 수치적 모델링과 국지 최적화 방법을 사용하는 반복적 자료 맞춤 과정을 통해 역(逆)문제를 풀어내는 파형 역산 방법이다. 주파수 영역 전파형 역산은 파형 역산의 비선형성과 국지 최적화 방법 때문에 역산 해가 국지 최소값으로 수렴할 수 있다는 문제점이 있다.

본 연구는 리프먼-슈윙거 방정식에 기초하는 탄성파 파형 역산 방법인 리프먼-슈윙거 파형 역산(LSWI)을 제안한다. 파형 역산은 역(逆) 산란 문제로서 참조 모델, 참조 파동장, 수신기에서 측정된 탐사 자료로부터 참조 모델과 실제 매질의 차이인 매질 섭동을 추정한다. 리프먼-슈윙거 파형 역산은 산란 이론의 기본 방정식인 리프먼-슈윙거 방정식에 기초하는 역 산란 문제를 직접 풀어낸다. 파형 역산 과정에서 매질 섭동은 가상 산란 송신원의 정의로부터 섭동 연산자로서 계산되어 참조 모델의 갱신에 사용된다. 이때 섭동 연산자에 포함된 느리기(속도의 역수)의 제공은 음향 파동 방정식에서 파동장과의 선형적 관계를 가진다. 리프먼-슈윙거 파형 역산은 느리기 제공의 선형적 성질과 직접 역산 접근을 통해 국지 최소값으로의 수렴 문제를

방지할 수 있다. 또한 역산 결과 모델이 단일 산란 가정 때문에 초기 모델에 의존하는 문제를 해결하고자 순차 주파수 전략을 선택하였다. 본 논문에서는 리프먼-슈윙거 파형 역산을 이용하여 초기 속도 모델에서 시작하여 저(低)주파수 성분이 포함된 탄성파 자료로부터 탐사 대상 지하 매질의 속도 모델을 추정할 수 있음을 예제를 들어 입증하였다.

본 연구에서 제안한 파형 역산을 실제 탐사 관측 자료에 적용하기 위해서는 자료 내 잡음 제거를 위한 전처리 과정이 필요하다. 보다 정확한 파형 역산 결과를 얻기 위해서는 초기 속도 모델의 선택과 저주파수 성분의 사용 또한 중요하다. 실제 탐사 자료에 대한 파형 역산 적용 시 발생하는 대부분의 문제들은 전파형 역산에서 발생하는 문제들과 유사하다. 해상 탐사 자료의 경우 제한된 오프셋 때문에 자료 간차로부터 매질 섭동을 추정하는 과정에서 자료 부족 문제가 발생하는데, 이에 대해서는 분할 정복법을 해결책으로서 고려해 볼 수 있다.

**주요어:** 탄성파 토모그래피, 파형 역산, 산란 이론, 주파수 영역, 리프먼-슈윙거 방정식

**학번:** 2010-21022